Doctoral Thesis in Physics

Thermal spin transport phenomena and magnetic proximity effect in Pt/ferromagnet bilayer systems

Spintronics and spin caloritronics

Panagiota Bougiatioti

Bielefeld University
Department of Physics

Declaration

I wrote this thesis by myself and used none but the indicated resources. Text and figures were partly taken from corresponding publications, which originate directly from this work.

(Panagiota Bougiatioti)

Reviewers:

Prof. Dr. Günter Reiss
Prof. Dr. Thomas Huser
Prof. Dr. Mathias Kläui

Bielefeld University, Department of Physics
Center for Spinelectronic Materials & Devices

Doctoral thesis
April 3, 2019

"The physical world can be interpreted only by the stepwise research from the partial to the total, from the leaf to the tree, from the tree to the forest, from the forest to the nature, from the nature to the physical world, from the physical world to the universe. Observing the total in ignorance of the partial is a fallacy."

Plato (428-347 B.C.)

Contents

Chapter 1

Introduction

Living in the era of information and social networks, the growth in the storage and memory technologies is associated with the advent of high performance computing and mobile devices, allowing for the generation and storage of the enormous amount of information. In 1980s the computers displayed memory of hundreds of kB, whereas nowadays the most common computers have about 8 GB random access memory [1]. The price per GB of hard drive storage was reduced from 200000 $ in 1982 to 0.06 $ in 2012 [2]. The fundamental question is how to continue the progress of the electronic devices in terms of size, speed, and price reduction, with the additional challenge of treating and storing efficiently a non-stop increasing quantity of information.

The continuous miniaturization of the device size for achieving higher circuit densities, is inextricably connected with increased power dissipation due to leakage currents [3], limiting considerably the improvement of electronic devices. In this background, novel technologies to replace the mainstream charge-based electronics are hot topics for research communities and industries. Upcoming *spintronic devices* hold the promise of faster switching speeds, less total energy consumption, and higher density of circuit elements, lowering the heat production per switching element. This could be achieved by employing the spin of the electrons instead of (or in addition to) the charge. The spin corresponds to the additional quantum mechanical property of an electron that can be described as an intrinsic angular momentum.

The outstanding breakthrough in the field of *spintronics* [4] concerns the discovery of the so-called *giant magnetoresistance* (GMR) effect, introducing the *spin-dependent transport* as a new physical approach compared to the magnetoresistance known before. GMR was introduced independently by the Nobel-Prize winners Albert Fert and Peter Grünberg in 1988 [5, 6], who reported spin-dependent transport phenomena in superstructures consisting of magnetic and non-magnetic metal layers. The basic structure of a GMR device, which is considered as spin valve, consists of two ferromagnetic (FM) layers with different magnetic switching fields and separated by a non-magnetic metal (NM) layer. When the magnetization vectors of the two FM layers are parallel, the electrons with spins parallel to the magnetization are hardly scattered leading to a low electric resistance state. In the antiparallel alignment, electrons with both spin-types undergo significant scattering resulting in a high electric resistance state. Along with this undeniable breakthrough in spintronics, Julliére *et al*. [7] realized the existence of the *tunneling magnetoresistance* (TMR) effect in Fe/GeO/Co trilayer at 4.2 K. In 1995, Miyazaki *et al*. [8] and Moodera *et al*. [9] observed the TMR effect at room temperature (RT) in $Fe/Al_2O_3/Fe$ and $FeCo/Al_2O_3/Co$ trilayers, paving the way for the evolution of nonvolatile solid-state memory devices, magnetoresistive random-access memory, and fast programmable logic circuits.

However, despite this progress the power consumption still increases and from an application standpoint, it constitutes the most challenging aspect in the development of modern information technologies. Energy conversion technologies provide the mechanisms to transform an input of energy (e.g. heat) into a more desirable and applicable form (e.g. electricity) that can be potentially used for waste heat recovery and temperature control. The spin-dependent electronic and thermal transport in materials is framed by the field of *spin caloritronics* [10–13], which is included as an additional complementary branch to the established field of *spintronics* and *thermoelectricity*. The transport of charge, magnetization (spin), or heat, occurs when the corresponding particles or quasi-particles (electrons, magnons, or phonons) are driven out of thermodynamic equilibrium. The conduction electrons can be utilized for spin transport through several mechanisms as well as thermal energy transport via the Wiedemann-Franz law. Magnons as bosonic quasi-particles, transport only heat and spin via perturbations of localized spins in the lattice. Phonons as similar bosonic quasi-particles they,

on the one hand, are considered to transport heat through perturbations of the positions of the atoms as well as spin [14]. On the other hand, they are capable of scattering and dragging conduction electrons and magnons and, thus, bring those particles out of thermal equilibrium under the presence of an external stimuli, e.g., temperature gradient.

In the fields of spintronics and spin caloritronics a variety of experimental and theoretical studies have been focused on spin-transport phenomena in NM/FM bilayer systems, where the spin current constitutes the core topic of the research [4, 10–13]. The generation, manipulation, and detection of spin-polarized currents in such systems is a very broad avenue holding promises towards the realization of next generation spintronic devices. An additional challenge can be introduced when utilizing NMs (e.g. Pt) as spin detectors which are near the Stoner FM instability [15], since a spin polarization in the NM can be generated by a static magnetic proximity effect (MPE). MPE could significantly influence the spin transport properties and give rise to additional phenomena that do not exist in the constituent materials in isolation [16–19]. Some groups used Cu or Au interlayers to suppress the MPE in NM/FMM bilayers [17, 20, 21] and others [17, 18] tried to isolate them while employing different measurement's geometries. Consequently, a comprehensive investigation regarding the magnetic properties of the NM/FM interface is required since MPE could modulate and emerge the functionality of future spintronic and spin caloritronic devices.

In this thesis we focus on the investigation and quantitative disentanglement of thermal spin transport phenomena in NM/FM systems, identifying and evaluating the contribution of possible MPEs in the transport measurements. We examine the cornerstone of the spin caloritronics, i.e., the *spin Seebeck effect* (SSE), in different kind of FM materials starting from nearly-insulating nickel ferrite ($NiFe_2O_4$ or NFO), semiconducting-like $NiFe_2O_x$ ($4 > x > 0$), and metallic $Ni_{1-x}Fe_x$ and $Co_{1-x}Fe_x$ bilayers, using Pt as a NM on top of the FM. The observation of the SSE in FM insulators (FMIs) [16, 22–29], allows for the generation of electric voltages without the thermal loss associated with mobile charge carriers, offering potential applicability to new functional devices in terms of energy harvesting. However, the application of FM metals (FMMs) and semiconducting FMs in the SSE measurements may give rise to parasitic charge current effects, like the anomalous Nernst effect (ANE) [30–40]. Additionally, when Pt is utilized as a spin current detector on an

adjacent FM film, a spin polarization in the Pt induced by a MPE might occur and generate a proximity-induced ANE. Therefore, even the application of FMIs in spin caloritronic experiments does not ensure a complete exclusion of additional proximity-induced effects which could prevent from the correct interpretation of the measured signal.

In our work, we tackle this issue by proposing a compact procedure to identify and quantitatively disentangle the FM- and proximity-induced ANE contributions to the SSE voltage. This proposed technique is further based on the identification and evaluation of the proximity induced magnetization in the NM. In particular, x-ray resonant magnetic reflectivity (XRMR) is utilized as a powerful tool when investigating interfacial spin polarizations, since it is based on the interference of light reflected from the interfaces in the system rendering this method independent from the layer thickness.

In the following chapter we will introduce the relevant phenomena from the mosaic of spintronics, thermoelectrics, and spin caloritronics which are used to interpret and discuss the experimental data. A thorough insight of the spin-dependent effects, charged based phenomena, and their thermal counterparts as well as their possible combinations, allows for a comprehensive understanding of the physics which enlarges upon our experiments.

In the experimental chapters we will focus on the proposed compact procedure for the quantitative disentanglement of thermal spin transport phenomena in NM/FM bilayers together with the obtained results, while utilizing different systems such as, FMIs (e.g. yttrium iron garnet or nickel ferrite), semiconducting-like FMs (e.g. $NiFe_2O_x$ with $4 > x > 0$), and FMMs (e.g. $Co_{1-x}Fe_x$ and $Ni_{1-x}Fe_x$). More specifically, in a first step we will provide information about the fabrication of the films and the characterization techniques used to investigate the film properties. In a next step, we will analyze the structural, magnetic, electrical, and optical properties of the $NiFe_2O_x$ films, addressing the conduction mechanisms that govern the systems in high and low temperature regimes, the optical band gap as well as the conduction type of the materials. We will continue with the presentation of the SSE data obtained in a Pt/YIG system, analyzing and emphasizing on the use of the heat flux method compared to the temperature difference determination. In the next three sections, we will present data for the isolation of the voltage generated by the SSE from the ANE voltage contributions, arising from both the FM and the spin polarized Pt layer in three Pt/FM systems, via different

spin injection geometries. We will further probe the dependence of the aforementioned effects on the stoichiometry and on the magnetic moments of both the FMM and the spin polarized Pt layer, when examining Pt/FMM systems.

In the last chapter, we will present our systematic study of the MPE in Pt on top of semiconducting-like FMs (e.g. $NiFe_2O_x$ with $4 \geq x > 0$) and FMMs (e.g. $Co_{1-x}Fe_x$) utilizing XRMR. We will further discuss the dependence of MPE on the electrical (e.g. conductivity) and magnetic (e.g. magnetic moment and anisotropy) properties of the adjacent FM, making one step towards the realization of the MPE mechanism.

All results presented here have already been published in different peer-reviewed journals or submitted for publication. The corresponding articles are referenced in the respective chapters.

Chapter 2

Fundamentals

2.1 Onsager reciprocity relations for transport phenomena

The first attempt to explain the thermoelectric phenomena occurring in a metallic system, was made by W. Thompson in 1854. According to his theory, reciprocal relations connect current densities and forces in analogy to mechanical systems where the applied forces are connected to perturbations to the equilibrium. As an example, an electric current in a circuit that consists of different metallic conductors will cause generation or absorption of heat at the junctions (Peltier effect). Conversely, if the junctions are maintained at different temperatures, an electromotive force will occur in the circuit (Seebeck effect). Some years later in 1931, Lars Onsager [41] extended the validity of the theory onto systems consisting of several mutually dependent irreversible processes and established a corner stone of linear irreversible thermodynamics, through the Onsager reciprocity relations.

According to the theory, around equilibrium the examined system must fulfill the requirements of thermodynamics and the general principle of time symmetry. Therefore, the current density $\boldsymbol{J}_{\mathrm{i}}$ of a certain quantity is a direct outcome of the linear combination of the corresponding driving forces $\boldsymbol{x}_{\mathrm{j}}$ following the relation

$$\mathbf{J}_\mathrm{i} = \widetilde{L}_\mathrm{ij}\mathbf{x}_\mathrm{j}, \tag{2.1}$$

where $\widetilde{L}_{ij}$ is defined as the *Onsager matrix* of transport coefficients, using the Einstein summation convention. The diagonal elements $\widetilde{L}_{ii}$ of the aforementioned matrix quantify the effect of an individual generalized force on the corresponding conjugate current density, e.g., the charge current density generated by the application of an electrical potential gradient or the heat current density generated by a temperature gradient. However, it is of significant importance to determine how the involvement of a generalized force can influence not only conjugate current densities but also the non conjugate ones, e.g., transport of electrons contributes to heat current density (Peltier effect). Such contributions are given by the off-diagonal elements $\widetilde{L}_{ij}$ of the Onsager matrix. All the off-diagonal elements satisfy the relation

$$\widetilde{L}_\mathrm{ij} = \widetilde{L}_\mathrm{ji}, \tag{2.2}$$

known as the *Onsager's reciprocity theorem*, consequence of the fact that the parameters characterizing the system are invariant under time inversion.

This thesis aims to provide a thorough analysis of effects in the fields of spintronics, thermoelectrics, and their combination known as spin caloritronics. Focusing on the effects that will be examined in the rest of the work, the Onsager relations can be written in the following simplified form [10]

$$\begin{bmatrix} \mathbf{J}_\mathrm{c} \\ \mathbf{J}_\mathrm{s} \\ \mathbf{J}_\mathrm{q} \end{bmatrix} = \begin{bmatrix} \widetilde{L}_\mathrm{cc} & \widetilde{L}_\mathrm{cs} & \widetilde{L}_\mathrm{cq} \\ \widetilde{L}_\mathrm{sc} & \widetilde{L}_\mathrm{ss} & \widetilde{L}_\mathrm{sq} \\ \widetilde{L}_\mathrm{qc} & \widetilde{L}_\mathrm{qs} & \widetilde{L}_\mathrm{qq} \end{bmatrix} \cdot \begin{bmatrix} \mathbf{E} \\ \boldsymbol{\nabla}\mu_\mathrm{s} \\ -\boldsymbol{\nabla}T \end{bmatrix}, \tag{2.3}$$

where $\mathbf{J}_\mathrm{c}$ is the charge current density, $\mathbf{J}_\mathrm{s}$ is the spin current density, $\mathbf{J}_\mathrm{q}$ is the heat current density, $\mathbf{E}$ is the electric field, i.e., a gradient in the electric potential, $\boldsymbol{\nabla}\mu_\mathrm{s}$ is a gradient in spin potential generated by the spin accumulation, and $\boldsymbol{\nabla}T$ is the temperature gradient, respectively.

The analysis of the components $\mathbf{J}_\mathrm{c}$ and $\mathbf{J}_\mathrm{s}$ via the Onsager matrix describes the individual effects that are mainly discussed in this thesis. The total charge current density is given by $\mathbf{J}_\mathrm{c} = \widetilde{L}_\mathrm{cc}\mathbf{E} + \widetilde{L}_\mathrm{cs}\boldsymbol{\nabla}\mu_\mathrm{s} - \widetilde{L}_\mathrm{cq}\boldsymbol{\nabla}T$. The first term $\widetilde{L}_\mathrm{cc}$ connects the generation of an electric field via the application of a charge current and, thus, is the conductivity tensor. The diagonal components of $\widetilde{L}_\mathrm{cc}$ involve the well known *Ohm's law* and the *longitudinal magnetoresistance*,

while the off-diagonal components describe *Hall effects* (ordinary Hall, planar Hall or transverse magnetoresistance and anomalous Hall). The second term $\widetilde{L}_{cs}$ stands for the generation of a charge current due to a spin accumulation, e.g. *inverse spin Hall effect*. The third term $\widetilde{L}_{cq}$ describes the generation of a charge current by the application of a temperature gradient and is correlated indicatively to the *Seebeck* and *Nernst effects* (anomalous Nernst, planar Nernst).

Analogous, the total spin current is given by $\mathbf{J}_s = \widetilde{L}_{sc}\mathbf{E} + \widetilde{L}_{ss}\boldsymbol{\nabla}\mu_s - \widetilde{L}_{sq}\boldsymbol{\nabla}T$. The first term $\widetilde{L}_{sc}$ describes the generation of a spin current by an applied electric field, e.g. *spin Hall effect*. The second term $\widetilde{L}_{ss}$ stands for the generation of a spin current due to a spin accumulation, e.g. *magnon Hall effects* [42]. The third term $\widetilde{L}_{sq}$ includes the generation of a spin current due to the application of a temperature gradient and is correlated to the *spin Seebeck* and *spin Nernst* effects. Correspondingly, the components $\widetilde{L}_{qq}$ and $\widetilde{L}_{qs}$ concern the *thermal Hall effects* [42] and the *spin Peltier effect*, respectively.

2.2 Spintronics

For more than 3 decades, *spintronics* has been one of the most attractive and rapidly growing research frontiers in materials science, focusing on the investigation and development of *spin transport electronics*. The introduction of the spin angular momentum (alternatively spin) as the electron's internal degree of freedom besides its fundamental properties such as mass and charge, forms the basis of this new branch of the already existing electronics [4]. In particular, the generation and control of "spin currents", i.e., spin-polarized electric currents and pure spin currents, play a crucial role in several phenomena in the field of spintronics. The most fundamental of these phenomena, characterized by their potential integration into new functional spintronic devices, are analytically discussed in the following.

Spin current An electron, apart from its charge, can be characterized by internal angular momentum. This internal angular momentum which can be understood in an intuitive picture similar to the rotation of a classical particle, is called *spin* and contributes an additional degree of freedom to the electron. Since the electron carries both charge and spin, the existence of a charge

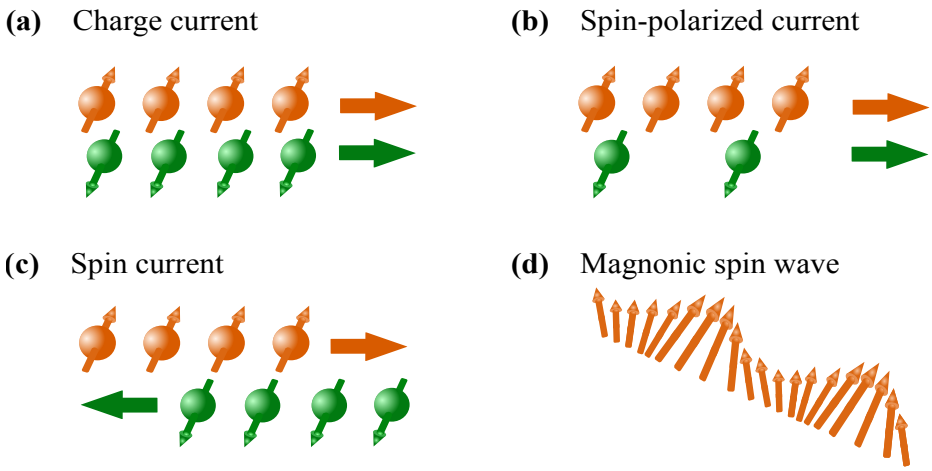

Figure 2.1. (a) Electrons with opposite spin orientations travelling along the same direction, constitute a net charge current. (b) Unequal number of electrons with opposite spin orientations travelling along the same direction, generate a spin-polarized current. (c) Electrons with opposite spin orientations travelling in opposite directions define a spin current. (d) Spin currents can also be generated via the coherent precession of magnetic moments leading to magnonic spin waves.

current with uncompensated spin polarization indicates the existence of spin flow. An imbalance in the flow of spin-up electrons and that of spin-down electrons is called *spin current*. In the case that the charge current direction of spin-up electrons is opposite to that of spin-down electrons and all electrons have the same drift velocity, the net charge current vanishes but a net amount of spin angular momentum does not and, thus, a pure spin current is generated. In this regime, the total charge current $\boldsymbol{I}_c = \boldsymbol{I}_c^{\uparrow} + \boldsymbol{I}_c^{\downarrow}$ is zero, while the total spin current is non zero $\boldsymbol{I}_s = \boldsymbol{I}_c^{\uparrow} - \boldsymbol{I}_c^{\downarrow} \neq 0$, as explained in Fig. 2.1(c). A pure spin current can also be present in non-conducting magnetic insulators as a result of coherent precessional waves of magnetization. These collective magnetic excitations are called *spin waves* and their quanta are named *magnons* which can directly transport heat, spin but not charge. Aside from pure spin or charge currents, the so-called (uncompensated) *spin-polarized currents* transport both charge and spin momentum, due to an imbalance of the populations of spin-up and spin-down charge carriers in the electric current. All these cases are sketched in Fig. 2.1.

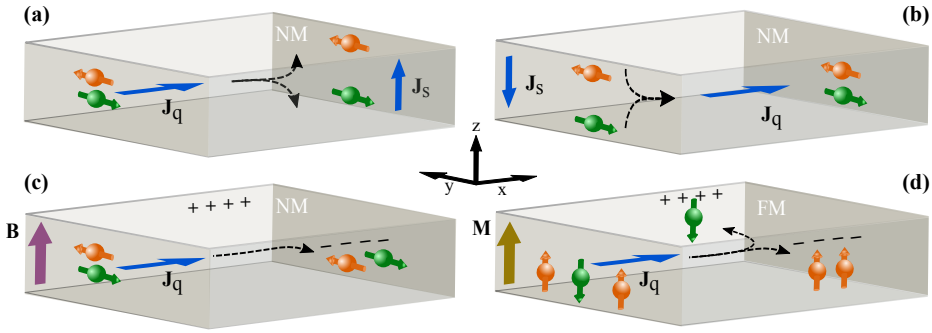

Figure 2.2. Schematic illustration of (a) the conversion of a charge current into a transverse spin current, SHE, (b) the conversion of a spin current into a transverse charge current, ISHE, (c) the generation of a transverse electric field under the application of a charge current in a presence of a perpendicular magnetic field, via OHE, and (d) the generation of a transverse electric field under the application of a charge current due to the magnetization of the ferromagnet, via AHE.

In the emerging field of spintronics a variety of phenomena that enable the generation, manipulation and detection of spin currents in ferro(i)magnetic, antiferromagnetic, as well as paramagnetic materials have been reported and framed by significant scientific interest, creating new challenges and perspectives within the field. One possible method for the generation of spin currents is the well known *spin-pumping* [43], generated by the *ferromagnetic resonance* [44]. Spin-pumping is the reciprocal effect of spin-transfer torque (an analytical description is included in Sec. 2.4), which are related to each other through the Onsager relation [see Eq. (2.2)]. Spin pumping describes the creation of a spin current through the magnetization dynamics of a ferromagnet in contact with a non-magnetic metal. In the following, several scattering phenomena, such as (inverse) spin Hall effect, ordinary (anomalous) Hall effect, spin Hall (anisotropic) magnetoresistance are discussed.

Spin Hall Effect A well established and versatile tool for spin current generation is the *spin Hall effect* (SHE). The SHE belongs to a group of phenomena that result from spin–orbit interaction, which associates orbital motion with spin direction and acts as a spin-dependent magnetic field. It presents great potential for spintronic applications creating spin currents which can be used to excite spin waves in ferro(i)magnetic, antiferromagnetic, as well as param-

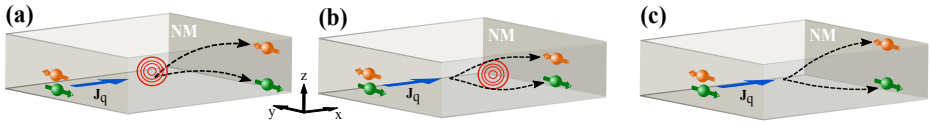

Figure 2.3. Schematics of the SHE and AHE mechanisms. Extrinsic contribution of (a) skew-scattering and (b) side-jump-scattering. (c) Intrinsic contribution.

agnetic materials or to switch the magnetization in FMs. Applying a charge current to the system, the electrons are driven along the electric field. In systems with strong spin–orbit coupling (SOC), the electrons are scattered spin-dependently. The spin-up and spin-down electrons are deflected in opposite ways, transverse to the charge current $\boldsymbol{J}_c$ and perpendicular to the spin polarization $\boldsymbol{s} = \frac{\boldsymbol{M}}{|\boldsymbol{M}|}$, as depicted in Fig. 2.2(a). A mechanical analogous is the Magnus effect where a spinning ball in a fluid deviates from its straight path in a direction that depends on the sense of rotation. The phenomenon was theoretically predicted by Dyakonov and Perel in 1971 [45, 46]. One year later it was quantitatively measured in InSb by Chazalviel and Solomon [47] and in 1975 Chazalviel reported the observation of the effect on Ge [48], with precisions that still rival more contemporary measurements. In 1999, Hirsch brought it to the attention of the spintronics community and established the term SHE [49], since in the direction perpendicular to the charge current there is a net spin current though no net charge current. In 2004, after Hirsch revived this topic Kato *et al.* [50] experimentally identified the existence of the SHE by using the magnetooptic Kerr effect to probe a spin accumulation transverse to a charge current in the non-magnetic semiconductor GaAs. In 2005, Wunderlich *et al.* [51] demonstrated the SHE developing a *p-n* junction light-emitting diode fabricated in (Al,Ga)As/GaAs heterostructures.

We distinguish between two distinct physical mechanisms causing the SHE, the *extrinsic* and the *intrinsic* one, determined by the dependence on external impurities. The extrinsic mechanism is controlled by the SOC with impurities and is classified into two forms: the asymmetric scattering (or *skew-scattering*) and the *side-jump* effect.

Skew-scattering The scattering is *skew* under the existence of different scattering probabilities of conduction electrons at impurity potentials depending on the spin momentum of the electron. More specifically, electrons moving in

the vicinity of an impurity charge center with spin polarization parallel to the y axis are characterized by the wave function Ψ^+ and the electrons with spin polarization antiparallel to the y axis are characterized by the wave function Ψ^-. Assuming the incoming state to propagate along the x axis, the outgoing wave function is scattered mainly parallel or antiparallel to the z axis, depending on the spin orientation of the corresponding wave function [52] [cf. Fig. 2.3(a)]. The spin orbit coupling (interaction between the electron spin and the inhomogeneous impurity potential) induces an anisotropic deviation along the z axis resulting in different scattering amplitudes, as depicted in Fig. 2.3(a). This distinct asymmetry between the two spin channels, is the origin of the spin current and the spatial spin separation [52].

Side-jump-scattering Similar to skew-scattering, the side-jump mechanism is characterized by a scattering asymmetry of the conduction electrons from impurity potentials with respect to their spin orientation. As indicated in Fig. 2.3(b), a discontinuous displacement in the direction transverse to the initial propagation direction of the electrons takes place at the impurity center. Phenomenologically, the displacement can be understood as the corollary of the local distortion of the wave function which describes the electron, creating a local current density. This displacement is the same for the spin-up and spin-down electrons, but with opposite sign. Therefore, the total momentum is conserved, in contrast to the skew-scattering mechanism.

Intrinsic Additionally to the extrinsic mechanisms, an intrinsic contribution influences the SHE as well. The intrinsic mechanism is associated with the spin-dependent band structure of the material. In a phenomenological approach, it originates from the non-equilibrium dynamics of Bloch electrons. As they are accelerated in the presence of an electric field, they precess around a k-dependent effective magnetic field $\mathbf{B}(\mathbf{k})$. As a consequence, the electron's alignment is directly influenced by the changes in the band structure of the crystal. In particular, considering a two-dimensional electron system with substantial Rashba spin-orbit coupling, in the presence of an electric field the Fermi surface is displaced with time. This displacement induces changes in $\mathbf{B}(\mathbf{k})$, leading to the creation of effective torques in order for the system to reacquire its energetically preferable state of the spin alignment with $\mathbf{B}(\mathbf{k})$

[53]. The group velocity of the electrons is associated with the spin direction and acquires a contribution perpendicular to the electric field [54]. In turn, the electrons with opposite spin orientations will drag to opposite directions and sides of the Fermi surface, according to their spin. Resultantly, a spin current is created [cf. Fig. 2.3(c)].

A parametrization of the efficiency of the charge-spin current conversion is given by the ratio between the transverse spin Hall conductivity σ_{SH} and the longitudinal charge conductivity σ_{c} (with response to the charge current), which defines the spin Hall angle, $\theta_{\mathrm{SH}} = \frac{\sigma_{\mathrm{SH}}}{\sigma_{\mathrm{c}}}$ [55]. The spin Hall angle is a material specific property depending on the SOC and dictates the amount of spin current generated from a charge current. Therefore, materials with a large spin Hall angle (of the order of $10^{-2}-10^{-1}$) either with positive (Pt [56], Pd [57]) or negative (Ta [58], W [59]) sign, exhibiting a pronounced SHE, are suitable for efficient charge-spin current conversion. A relation between the induced spin current density $\boldsymbol{J}_{\mathrm{s}}$ and the applied charge current density $\boldsymbol{J}_{\mathrm{c}}$ is given by the formula [55]

$$\boldsymbol{J}_{\mathrm{s}} = \theta_{\mathrm{SH}}\left(\frac{\hbar}{2e}\right)\boldsymbol{J}_{\mathrm{c}} \times \boldsymbol{s}, \tag{2.4}$$

where $\hbar$ is the reduced Planck constant and e is the electron charge. The spin polarization vector $\boldsymbol{s}$ points in the direction of the spin momentum [60].

Inverse Spin Hall Effect A powerful way for experimental detection of pure spin currents is the utilization of the *inverse spin Hall effect* (ISHE). ISHE, as the reverse process of SHE, induces a transverse charge current from the injected spin current. Analogous, the generated charge current density $\boldsymbol{J}_{\mathrm{c}}$ is given by the formula [55]

$$\boldsymbol{J}_{\mathrm{c}} = \theta_{\mathrm{SH}}\left(-\frac{2e}{\hbar}\right)\boldsymbol{J}_{\mathrm{s}} \times \boldsymbol{s}. \tag{2.5}$$

Both SHE and ISHE are sketched in Fig. 2.2 indicating the orthogonality of the vectors $\boldsymbol{J}_{\mathrm{c}}$, $\boldsymbol{J}_{\mathrm{s}}$ and $\boldsymbol{s}$. Moreover, the imbalance of charge carriers in the NM generates an electric field which is expressed by [61]

$$\boldsymbol{E}_{\mathrm{ISHE}} \propto \boldsymbol{J}_{\mathrm{s}} \times \boldsymbol{s}, \tag{2.6}$$

The ISHE efficiency is described by the pre-factors in Eq. (2.5) including the resistivity of the NM [62].

It is worth noting that one of the key parameters for spin and charge transport is the so-called spin diffusion length λ_N [63], i.e., the distance over which the traveling electron spin conserves its initial orientation. Experimentally this means, a spin detector material, i.e., a NM with large spin Hall angle adjacent to a FM which converts spin current into a charge current should have a limited thickness, dictated by the spin diffusion length λ_N. The spin current progressively decays while it propagates in the material and its reduced value is given by [64]

$$j_s(z) = j_s^0 \frac{sinh((z - t_N)/\lambda_N)}{sinh(t_N/\lambda_N)}, \tag{2.7}$$

where z is the distance from the interface, t_N is the thickness of the NM layer, and j_s^0 is the net spin current which is generated at the NM/FM interface.

One significant step further in spintronic applications is to use the spin current generated from a charge current via the SHE, to manipulate magnetic moments. In 2012, Liu *et al*. reported the discovery of a giant SHE in Ta and demonstrated that this allows an electrical current in a thin Ta layer to efficiently induce *spin-torque switching* of the magnetization in an adjacent thin FM of an MTJ placed on top of the Ta [58]. By changing the polarity of the charge current applied in the Ta layer, the switching can be reversed. Here, the switching is achieved by a pure spin current, whereas in conventional STT experiments (explained in Sec. 2.4) a spin-polarized charge current is used.

Hall Effect The SHE discussed above is independent of the magnetization or the external magnetic field and is directly determined by the strength of the spin orbit interaction. In the next paragraphs, we will compare the SHE with other Hall effects which depend on the magnetization or the external magnetic field. In 1879, Edwin H. Hall [65] discovered that when an external magnetic field $\boldsymbol{B}$ is applied perpendicular to a charge current in a metallic (non-magnetic) material, the moving electrons are deflected due to the Lorentz force $\boldsymbol{F}_L = q(\boldsymbol{u} \times \boldsymbol{B})$. For electrons ($q = -e$) the resulting total force $\boldsymbol{F}_{tot}$ is given by

$$\boldsymbol{F}_{tot} = -e(\boldsymbol{E}_{ext} + \boldsymbol{u} \times \boldsymbol{B}), \tag{2.8}$$

where $q = -e$ is the electric charge of the electron, $\boldsymbol{u}$ its velocity and $\boldsymbol{E}_{ext}$ is the externally applied electric field. Considering the geometry in Fig. 2.2(c), the application of a charge current along the x axis in the presence of an external magnetic field along the z axis results in the deflection of the electrons along the y axis, perpendicular to both the initial direction of motion and the external magnetic field. Consequently, this charge accumulation builds up a transverse electric field along the y axis, the so-called Hall field. This spin-independent phenomenon is known as the *ordinary Hall effect* (OHE) [65, 66]. In a general approach, the OHE field $\boldsymbol{E}_H$ is given by

$$\boldsymbol{E}_H = R_H(\boldsymbol{J}_c \times \boldsymbol{B}), \tag{2.9}$$

where R_H is the OHE resistance and $\boldsymbol{J}_c$ is the charge current density.

In a steady state, the Hall field counteracts the Lorenz force so as, $e\boldsymbol{E}_H + \boldsymbol{F}_L = 0$. Considering Eq. (2.9), the electrons' density n can be obtained by the formula

$$R_H = -\frac{r}{ne} \approx -\frac{1}{ne}, \tag{2.10}$$

where r is the ratio between the Hall mobility μ_H and the drift mobility μ_D, the so-called scattering factor for electrons (holes) that takes into account the energy spread of the carriers and is defined as

$$r = -\frac{\mu_H}{\mu_D} = \frac{\langle\tau^2\rangle}{\langle\tau\rangle^2}, \tag{2.11}$$

where τ is the mean-free time between carrier collisions and reflects the individual scattering processes. More specifically, τ is energy dependent such as $\tau(E) \propto E^{-S}$, where S is dictated by the individual scattering mechanism. Three major scattering mechanisms that considerably influence the transport phenomena in crystals are defect, carrier-carrier, and lattice scattering. Usually r is set equal to 1, however, this unjustified assumption may induce uncertainties in the calculation of the carrier density of the material and should be critically treated. This issue is also discussed in the experimental part of this thesis.

In the case that holes are the majority charge carries in the crystal, the above analysis can be implemented in a similar way and the Hall resistance is equal to $R_H = \frac{1}{pe}$, where p is the holes' density. It's worth mentioning that

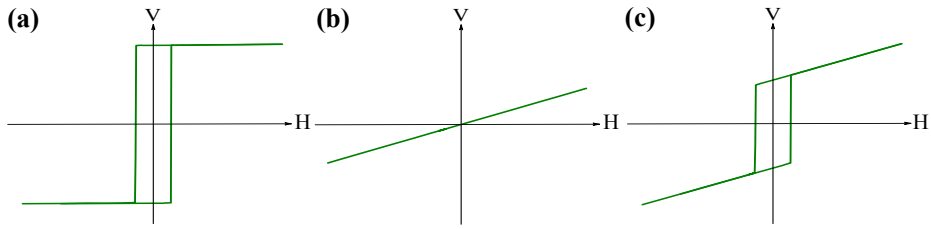

Figure 2.4. (a) The AHE voltage signal of a FM conductor, presenting a non-linear behaviour with respect to the magnetic field. The voltage abruptly increases for low magnetic fields and it nearly saturates for high magnetic fields due to the saturated magnetization. (b) The OHE voltage signal of full conducting materials presenting a proportionality to the applied external magnetic field. (c) The superposition of OHE and AHE signals in FM conductors presenting a hysteresis curve, which increases proportionally to the applied external magnetic field and, thus, without obtaining a saturation value.

when the magnetic field direction changes from out-of-plane to in-plane in the aforementioned configuration, the measured electric field transverse to the applied charge current is then attributed to the *planar Hall effect* (PHE).

Anomalous Hall Effect In 1880, Edwin H. Hall found that this transverse electric field produced by the OHE is ten times larger in ferromagnetic materials than in non-magnetic conductors [67]. To analyze this case we consider a FMM and we replace the external magnetic field with the magnetization [see Fig. 2.2 (d)]. In a FMM, the numbers of spin-up and spin-down charge carriers at the Fermi level are different resulting in spin-dependent scattering contributions of the charge carriers. Consequently, the imbalance in the spin dependently scattered charge carriers results in a net charge separation and an emerging voltage transverse to the applied current. This is the so-called *anomalous Hall effect* (AHE) and can be considered as the spin-dependent equivalent of the OHE. In this regime, the Lorentz force acting onto the electrons is negligible and the scattering process only depends on the spin orientation. Therefore, the mechanisms behind AHE are strongly depending on the SOC and contain intrinsic (Berry curvature [68]) and extrinsic (skew scattering and side jump effect) contributions, as discussed in the SHE analysis. A detailed overview can be found in Ref. [69].

Considering a FMM in a measurement geometry as illustrated in Fig. 2.2 (d), the electric field $\boldsymbol{E}$ detected along the y axis is a superposition of both OHE and AHE. The AHE contribution is proportional to the magnetization $\boldsymbol{M}$ of the material, presenting a hysteresis curve which is antisymmetric with respect to the external magnetic field, as visible in Fig. 2.4(a). The OHE contribution can be disentangled from the total signal [cf. Fig. 2.4(c)], when identifying the slope [cf. Fig. 2.4(b)] which changes linearly with the field in the region where the magnetization dependent AHE saturates.

Spin Hall Magnetoresistance Another recently discovered spin current-based effect is the so-called *spin Hall magnetoresistance* (SMR) when examining NM/ferromagnetic insulator (FMI) bilayer systems, benefiting from the lack of mobile charge carriers in the FMI. FMIs have attracted considerable scientific interest presenting a long-range magnetic order, that enables the propagation of magnetic excitations (spin currents), while remaining electrical insulators. Therefore, they can provide a distinct separation of spin and charge currents, since the charge current is restricted to the conductive NM layer, while spin currents can propagate in both the NM and the FMI layers.

In a NM/FMI bilayer when a charge current flows through the NM with a large SOC, the SHE occurs converting the charge current into a transverse spin current. In turn, the spin current builds up a spin accumulation at the interfaces of the NM. Depending on the magnetization orientation of FM layer below, the spins at the bottom interface are either mainly "absorbed" considering the spin torque, or mainly "reflected". The "reflected" spins are converted back into a charge current in the NM, via the ISHE. Therefore, the longitudinal resistance of the NM (as response to the charge current) is affected by the magnetization orientation of the FMI. The SMR effect has been reported in many publications and discussed in various material combinations in the last years [60, 70–73].

Anisotropic Magnetoresistance The anisotropic magnetoresistance (AMR) concerns the dependence of the electrical resistivity on the relative angle between the directions of the magnetization direction and the applied charge current. AMR was discovered in 1856 by William Thomson in FMMs (Ni and Fe bulk samples) [74], where they reported a resistivity change under

the application of an external magnetic field. A simplified picture of the AMR model includes the shape/symmetry of the atomic orbitals in the crystal. More specifically, the charge distribution of the atoms is not spherical but it is distorted, due to SOC. Different orientations between the atomic orbitals and the applied charge current lead to different scattering cross sections for the charge carriers in the crystal. Since the orbitals in the crystal align with the magnetization, a change in the magnetization orientation results in different scattering cross sections and, thus, a change of the resistivity.

2.3 Thermoelectrics

Thermoelectrics represents an emerging field attracting strong scientific interest due to the continuous need for the investigation of more efficient materials for electronic refrigeration and power generation devices [75]. Thermoelectric effects involve the interplay between the electrical and thermal properties of a system by converting thermal into electrical energy and vice versa. The development of quantum theory and its application to the electronic and thermal properties of the semiconductors, provided a deeper understanding of the thermoelectric materials [76].

Seebeck Effect The thermoelectric effect which has gained widespread popularity, was discovered in 1821 by T.J. Seebeck. The *Seebeck effect* describes the occurrence of an electrical potential difference between two points of an electrically conducting material which are exposed to different temperatures. The magnitude of this thermoelectric field is proportional to the temperature difference and is given by [77]

$$\boldsymbol{E} = -S\boldsymbol{\nabla}T, \tag{2.12}$$

where S is the Seebeck coefficient which parameterizes the efficiency of the conversion of a temperature difference into an electric field $\boldsymbol{E}$. In particular, Seebeck effect can be simply demonstrated by making a connection between wires of thermoelectrically dissimilar metals. When the junction between the wires is heated, a voltage is detected in the open ends of the two metals. Consequently, when the open ends are exposed to a known reference temperature, then the recorded voltage can be calibrated and provides information about

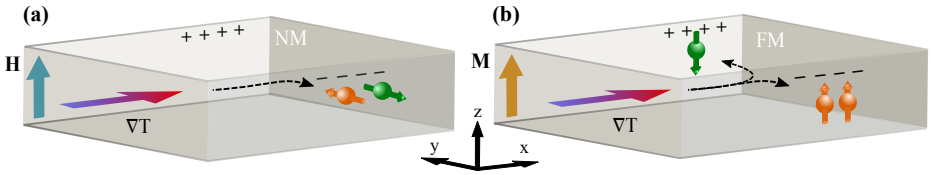

Figure 2.5. (a) The generation of a transverse electric field under the application of a thermal gradient in the presence of a perpendicular magnetic field via ONE. (b) The generation of a transverse electric field under the application of a thermal gradient due to the intrinsic magnetization of the ferromagnetic conductor via ANE.

the exact temperature at the junction. This device which is used regularly as thermometer is called *thermocouple*. Thermocouples also operate in another way when an electric current is driven through it, the couple acts as a heat pump and cools down the junction via the *Peltier effect*. These so called Peltier elements have been used as heat flux sensors to determine the temperature difference in some experiments included in this thesis.

Ordinary Nernst Effect The field of thermoelectrics when combined with the presence of an external magnetic field, is extended to the field of *magneto-thermoelectrics*. The thermal equivalent of the Hall effect described earlier, is a spin-independent phenomenon which is present also in non-magnetic materials the so-called *Ettinghausen-Nernst* or *ordinary Nernst effect* (ONE) [78]. By replacing the electrical current in the Hall geometry with a thermal gradient, a transverse electric field will be detected as a response to the applied thermal gradient. The geometry of the ONE is depicted in Fig. 2.5(a) with a thermal gradient applied along the x axis in the presence of a magnetic field along the z axis. The Nernst field is recorded along the y axis transverse to the applied thermal gradient. The ordinary Nernst field $\boldsymbol{E}_{\mathrm{ONE}}$, is given by the cross product of the thermal gradient $\boldsymbol{\nabla} T$ and external magnetic field $\boldsymbol{H}$ according to the formula

$$\boldsymbol{E}_{\mathrm{ONE}} = \mu_0 D_{\mathrm{ONE}} \boldsymbol{\nabla} T \times \boldsymbol{H}, \tag{2.13}$$

where μ_0 is the permeability of free space and D_{ONE} is the Nernst coefficient. The quantitative analysis of D_{ONE} provides information not only about the efficiency of the ONE in transport measurements but also about the carrier

system (one-carrier system or two-carriers system) while examining materials with semiconducting behaviour. As an example, the D_{ONE} for a mixed-type semiconductor is given by [79]

$$D_{\mathrm{ONE}} = \frac{k_{\mathrm{B}}}{|e|}\left[\left(\frac{\sigma_{\mathrm{n}}}{\sigma}\mu_{\mathrm{H_n}} + \frac{\sigma_{\mathrm{p}}}{\sigma}\mu_{\mathrm{H_p}}\right)r_{\mathrm{s}} + \frac{\sigma_{\mathrm{n}}\sigma_{\mathrm{p}}}{\sigma^2}(\mu_{\mathrm{H_n}} + \mu_{\mathrm{H_p}})\left(2r_{\mathrm{s}} + 5 + \frac{E_{\mathrm{gap}}}{k_{\mathrm{B}}T}\right)\right], \quad (2.14)$$

where σ_{n} is the conductivity of electrons, σ_{p} is the conductivity of holes, σ is the total conductivity, $\mu_{\mathrm{H_n}}$ is the mobility of electrons, $\mu_{\mathrm{H_p}}$ is the mobility of holes, E_{gap} is the band gap energy, k_{B} is the Boltzmann constant, and r_{s} is a factor which parameterizes the scattering process in the system. At very low temperatures, ionized impurity scattering dominates with $r_{\mathrm{s}} = +3/2$. On the contrary, at high temperature ranges lattice scattering is dominant, with $r_{\mathrm{s}} < 0$. For an extrinsic semiconductor for which either σ_{n} or σ_{p} vanishes (one carrier system), the ambipolar term containing the factor $\sigma_{\mathrm{n}}\sigma_{\mathrm{p}}$ also vanishes. Thereby, in a one-carrier system in which only electrons or holes contribute to the measured conductivity, D_{ONE} obtains values of the order of some (nV/TK), or instead, higher values [of the order of some (mV/TK)] for a two-carrier system [79] (At this point, let us clarify that K and T stand for Kelvin and Tesla, respectively).

Anomalous Nernst Effect The thermally driven counterpart of the AHE described in the previous paragraphs, is the so-called *anomalous Nernst effect* (ANE). While studying ferro(i)magnetic conductors, the application of a thermal gradient $\boldsymbol{\nabla} T$ induces a transverse electric field $\boldsymbol{E}_{\mathrm{ANE}}$ which scales with the magnetization $\boldsymbol{M}$, as visible in Fig. 2.5(b). $\boldsymbol{E}_{\mathrm{ANE}}$ is given by the formula

$$\boldsymbol{E}_{\mathrm{ANE}} = D_{\mathrm{ANE}}\boldsymbol{\nabla} T \times \boldsymbol{M}, \quad (2.15)$$

where D_{ANE} is the ANE coefficient. Analogous to the Hall measurements, when investigating FM conductors the manipulation of $\boldsymbol{M}$ by the application of an external field $\boldsymbol{H}$ implies the superposition of ONE and ANE fields as a response to the applied thermal gradient. The same separation technique as in case of the OHE and AHE is employed for the disentanglement of the aforementioned contributions with attributing the antisymmetric part of the curve to the ANE and the field-dependent linear contribution to the ONE.

Anisotropic Magnetothermopower In magnetic conductors under the application of an in-plane temperature gradient and in the presence of a magnetic field, the spin-orbit interaction induces an anisotropic thermoelectric voltage depending on the angle between the temperature gradient and the magnetization. The generation of a thermoelectric voltage parallel to the applied temperature gradient with an in-plane magnetic field, is called *anisotropic magnetothermopower* (AMTP) and is considered as the thermal counterpart of the AMR. Apart from the longitudinal AMTP, a thermoelectric voltage can be generated transverse to the temperature gradient which is attributed to the transverse AMTP, also called the *planar Nernst effect*, the thermal equivalent of PHE.

2.4 Spin caloritronics

The recently established field of "spin caloritronics" combines research on spin-related phenomena with thermoelectric effects [4, 10, 11]. The concept of spin caloritronics arose almost 30 years ago, when M. Johnson and R. H. Silsbee [80] predicted that the transport of heat in a ferromagnetic system was associated with the transport of spin, substantiated by theoretical insights into the non-equilibrium thermodynamics of spin, charge, and heat in metallic heterostructures with collinear magnetization configurations. Therefore, this work unveiled new prospects for the generation and manipulation of both heat and spin currents.

Spin Seebeck effect One of the groundbreaking developments in the last years in the field of spin caloritronics has been the discovery of the spin version of the Seebeck effect, the *spin Seebeck effect* (SSE). Its major importance in spintronics and spin caloritronics relies on the efficient generation of a *spin current* as a result of an applied temperature gradient, in a spin analogy of the Seebeck effect. A schematic illustration of the local SSE is given in Fig. 2.6(a) considering a NM/FM system. In particular, a temperature gradient ($\boldsymbol{\nabla} T$) is applied to the spin-polarized material in which spin currents can be generated, carried either by magnons, by spin-polarized electrons, or by a combination of them, e.g. in FMMs.

The temperature gradient induces a thermodynamic force that drives the spin carriers (electrons or magnons) out of thermal equilibrium resulting in a heat flux [12]. Specifically, in FMs two mechanisms dictate the thermal non-equilibrium state of magnons, i.e., the magnon thermal conductivity and the intense phonon-magnon interactions (phonon-magnon drag effect). Considering the magnon thermal conductivity K_{M}, in the presence of a temperature gradient magnons carry heat current density $\mathbf{J}_{\mathrm{q}} = K_{\mathrm{M}} \boldsymbol{\nabla} T$. Since magnons carry angular momentum as well, this gives rise to a thermally induced spin current density $\mathbf{J}_{\mathrm{S}} \approx \frac{\hbar}{k_{\mathrm{B}} T} \mathbf{J}_{\mathrm{q}} = \frac{\hbar}{k_{\mathrm{B}} T} K_{\mathrm{M}} \boldsymbol{\nabla} T$ [12].

The phonon-magnon drag effect emerges when the frequency of the phonon-magnon collisions is larger than the frequency of the phonon-phonon and phonon-defect collisions in the system. Considering the assembly of phonons acting as an ideal gas, at a certain temperature they exert a pressure. Under the application of a temperature gradient this pressure is converted into force acting on the magnons and inducing a magnon heat current density. In turn, a thermally induced spin current density appears [12].

In the case of FM-semiconductors or FMMs (existence of free conduction-electrons), under the thermal stimuli the resulting conduction-electron accumulation at the edges of the sample will produce a spin accumulation that decays over the length scale of the spin-diffusion length. This is the concept of the spin-dependent Seebeck effect which is described later on in the thesis. An additional mechanism that could bring the electron concentration out of thermal equilibrium is the intense phonon-electron interactions (phonon-electron drag) [12].

In a next step, the generated spin current propagating towards the NM/FM interface is pumped into the NM. The pumped spin current (spin current density $\boldsymbol{J}_{\mathrm{s}}$) is converted into a transverse electric field, via the *inverse spin Hall effect* [61, 81–83]. Experimentally, there are two different configurations to measure the spin Seebeck effect, the *transverse* configuration and the *longitudinal* one [cf. Fig. 2.6(a)], depending on the transverse or longitudinal application of the thermal gradient with respect to the probing direction of the induced spin current. Both configurations are analyzed later on. From an application standpoint, the prominent outcome is that SSE, like thermoelectricity, relates a voltage to a temperature difference (or heat flux), acting as a solid-state heat-to-electricity converter.

At this point it's worth mentioning that the origin of the SSE is vividly discussed within the scientific community. A group of authors [10, 84–86] argue that the spin current results from the temperature difference of the magnons in the FM and the electrons in the NM at their interface, producing a thermal interfacial spin pumping. This is the interfacial contribution of the SSE which produces an electric field that is in agreement with the measured values in the transverse SSE configuration (although the experimental observation of the transverse SSE is dubious). It is also believed [10, 86] that the same mechanism is operative in the longitudinal configuration. However, recent studies [87–91] claim that the experimental results of the longitudinal SSE in NM/FMI bilayers can be also interpreted by a different mechanism in which the magnon spin current is generated by the temperature gradient in the bulk of the FMI film and not at the interface. This is the bulk contribution of the longitudinal SSE which holds in both local and nonlocal SSE experiments, since a temperature driven magnon current is excited wherever a temperature gradient is present, either close to the heating source or also much further away [91].

In contrast to the local SSE configuration where a NM layer or strip is deposited on top of the FM layer, the nonlocal SSE geometry requires two NM stripes placed on top of the FM layer, separated by a certain distance and parallel to each other, serving as the spin current injector and detector, respectively. The application of a temperature gradient in the injector (e.g. via Joule heating from an applied charge current) leads to the thermal generation of a magnon spin current which diffuses towards the detector. The magnonic spin current is then quantified via the nonlocal charge voltage measurement at the detector, as an outcome of the ISHE. Nonlocal SSE experiments have been conducted on Pt/Yttrium iron garnet (YIG) [91–95], Ta/YIG [95], and Pt/NFO [96, 97] systems, yielding information about the magnon spin diffusion length, the magnon spin conductivity, and the magnon-polaron formation.

In 2008, Uchida *et al*. [98] initially reported the observation of SSE in a ferromagnetic metal $Ni_{81}Fe_{19}$ (20 nm), while using 10 nm of a Pt strip on top as a spin detector. Two years later in 2010, Xiao *et al*. [84] described the mechanism of SSE in terms of *interfacial thermal spin pumping* (see Fig. 2.8). The length scale of the generated spin current is governed by the relaxation length between magnons and phonons, which is much longer than the spin relaxation length. This approach differs from the standard spin accumulation

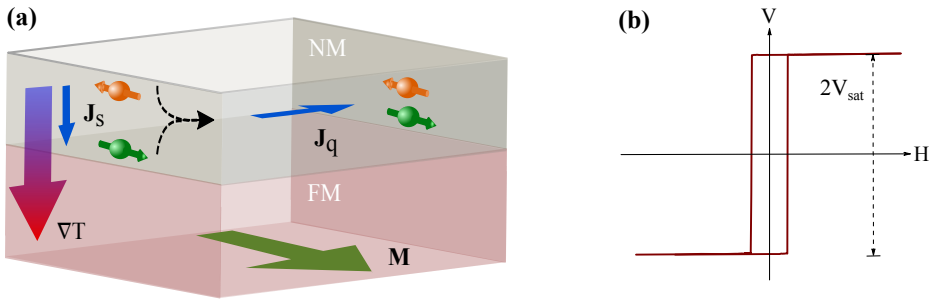

Figure 2.6. (a) Schematic illustration of the LSSE configuration. The ISHE in the NM converts the pure spin current into transverse charge current. (b) The antisymmetric voltage V as a function of the external magnetic field H for the LSSE configuration.

picture due to the independence of the spin transport mechanism from the conduction electrons. Consequently, this suggests that SSE should exist in ferro(i)magnetic insulators (FMI) or semiconductors as well. The confirmation of the above theory came in 2010 by Uchida *et al.* reporting the transverse SSE in the FMI YIG [99] and in the semiconductor GaMnAs, by Jaworski *et al.* [100]. However, it's worth mentioning that these experiments could not be repeated by other groups using the same length scales and thermal gradients.

Interfacial thermal spin pumping In order to further analyze the fundamental principles of SSE proposed by Xiao *et al.*, we will start with the basic concepts of the *Landau–Lifshitz–Gilbert* (LLG) equation that describes the phenomenology of magnetization dynamics, *spin transfer torque* (STT), and *spin-pumping effects* for exchanging angular momentum between conduction electron spins and magnetization. We start by considering a FM with its macroscopic magnetization $\boldsymbol{M}$ which saturates to a maximum $|\boldsymbol{M}| = M_s$. The magnetic state is described by a unit vector order parameter $\boldsymbol{m} = \frac{\boldsymbol{M}}{M_s}$. In thermal equilibrium, $\boldsymbol{m}$ is parallel to the effective magnetic field $\boldsymbol{H}_{\text{eff}}$ in the FM [55]. $\boldsymbol{H}_{\text{eff}}$ describes the externally applied magnetic field in addition to the internal magnetic fields expressing demagnetization, magnetic anisotropy, and exchange energies. After the application of an external stimulus, $\boldsymbol{m}$ is driven into a precessional motion around $\boldsymbol{H}_{\text{eff}}$. In a generalized picture, the precessing magnetization encloses the so-called precession cone angle, as visible in Fig. 2.7(a). In turn, taking into account the energy dissipation (con-

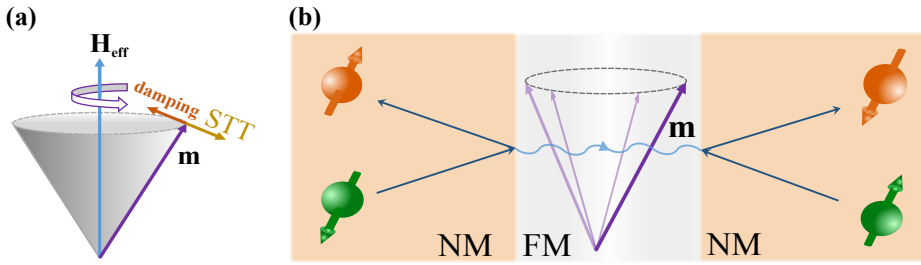

Figure 2.7. Schematic illustration of (a) the precession cone angle, (b) the spin transfer torque (STT) and its reciprocal effect, the spin-pumping.

sidering damping contributions), the magnetization dynamics are modeled using the LLG equation [55]

$$\frac{\partial \boldsymbol{m}(\boldsymbol{r},t)}{\partial t} = -\gamma \boldsymbol{m}(\boldsymbol{r},t) \times [\boldsymbol{H}_{\text{eff}}(\boldsymbol{r}) + \boldsymbol{h}(\boldsymbol{r},t)] + \alpha \boldsymbol{m}(\boldsymbol{r},t) \times \frac{\partial \boldsymbol{m}(\boldsymbol{r})}{\partial t}, \quad (2.16)$$

where γ is the gyromagnetic ratio, α is the Gilbert damping constant, and $\boldsymbol{h}(\boldsymbol{r},t)$ is a random magnetic field associated with all sources of magnetic damping, i.e., the thermal random field from the lattice considering the bulk damping, the random field $\boldsymbol{h}'$ from the NM contact associated with the enhanced damping α', and other possible random fields (additional contacts).

In order to further realize the origin of $\boldsymbol{h}(\boldsymbol{r},t)$, we should consider the fluctuation-dissipation theorem (FDT) for a magnetic system established by Callen and Welton [101]. More specifically, the precessing magnetization experiences dissipative magnetic Gilbert damping, due to the interactions with the lattice and/or electrons. Accordingly, the thermal fluctuations of lattice and/or electrons exert a random torque on the magnetization as well, causing the magnetization to fluctuate as well. This random torque is parameterized by the random magnetic field $\boldsymbol{h}(\boldsymbol{r},t)$ in the LLG equation [see Eq. (2.16)].

Spin transfer torque [102] and spin-pumping effects [43], concern two reciprocal effects which reflect identical microscopic correlations according to the Onsager reciprocity relations. In quantum mechanics, the aforementioned effects can be discussed as illustrated in Fig. 2.7(b). The left interface in Fig. 2.7(b) describes the STT process. In this regime, the electron in the

NM which reaches the FM interface is reflected and at good interfaces this reflection is always associated with a spin-flip. Consequently, on the left side of the NM/FM interface there is a net angular momentum current, whereas on the right side of the interface there is no angular momentum. In order for the angular momentum to be conserved, there is the emergence of the ferromagnetic order parameter, the so-called spin transfer torque $\boldsymbol{N}_{\text{stt}}$. If we consider a spin accumulation $\boldsymbol{\mu}_{\text{s}}$ in the NM, $\boldsymbol{N}_{\text{stt}}$ is given by [35]

$$\boldsymbol{N}_{\text{stt}} = \frac{1}{4\pi}[\text{Re}(G^{\uparrow\downarrow})\boldsymbol{m} \times (\boldsymbol{m} \times \boldsymbol{\mu}_{\text{s}}) - \text{Im}(G^{\uparrow\downarrow})\boldsymbol{m} \times \boldsymbol{\mu}_{\text{s}}], \tag{2.17}$$

where $G^{\uparrow\downarrow} = \text{Re}(G^{\uparrow\downarrow}) + i\text{Im}(G^{\uparrow\downarrow}) = G^{\downarrow\uparrow}$ denotes the dimensionless NM/FM interfacial spin mixing conductance in the spin-conductance tensor and quantifies the properties of the interface.

The right interface in Fig. 2.7(b) describes the reciprocal process to the STT, the spin-pumping effect. In this case, the spin angular momentum of the precessing magnetization in the FM layer is transferred to the electrons in the NM layer through dynamical exchange interactions at the NM/FM interface, meaning that the magnetization dynamics transfer a spin current from the FM to the NM. The spin-pumping current emitted by the magnetization $\boldsymbol{M}(t)$ is given by [43]

$$\boldsymbol{I}_{\text{sp}}(t) = \frac{\hbar}{4\pi}\text{Re}(G^{\uparrow\downarrow})\left[\boldsymbol{m}(t) \times \frac{d\boldsymbol{m}(t)}{dt}\right] + \text{Im}(G^{\uparrow\downarrow})\frac{d\boldsymbol{m}(t)}{dt}. \tag{2.18}$$

The imaginary part of $G^{\uparrow\downarrow}$ is usually much smaller than the real part and can be neglected in this formalism. $\boldsymbol{I}_{\text{sp}}(t)$ is polarized in the direction of $\boldsymbol{m}(t) \times \frac{d\boldsymbol{m}(t)}{dt}$. It is crucial to note that some angular momentum that is transmitted in the NM, returns back to the FM due to the non-equilibrium spin accumulation in the NM $\left(\boldsymbol{I}_{\text{s}}^{\text{back}}(t)\right)$ [43, 103]. High-Z metals with SOC are characterized by large spin-flip rate. Therefore, a spin-polarized electron is more probable to lose its spin information in the NM and, thus, the back-flow spin current into the FM will be reduced. Consequently, in a steady state ($\boldsymbol{I}_{\text{sp}}(t) \neq \boldsymbol{I}_{\text{s}}^{\text{back}}$) the total thermally pumped spin current $\boldsymbol{I}_{\text{sp}}^{\text{tot}}(t)$ is given by

$$\boldsymbol{I}_{\text{sp}}^{\text{tot}}(t) = \boldsymbol{I}_{\text{sp}}(t) + \boldsymbol{I}_{\text{s}}^{\text{back}}(t) \quad . \tag{2.19}$$

As a next step, to illustrate the basic idea of Xiao *et al.*, let us consider the NM/FM bilayer system as depicted in Fig. 2.8. The magnetization in the FM is

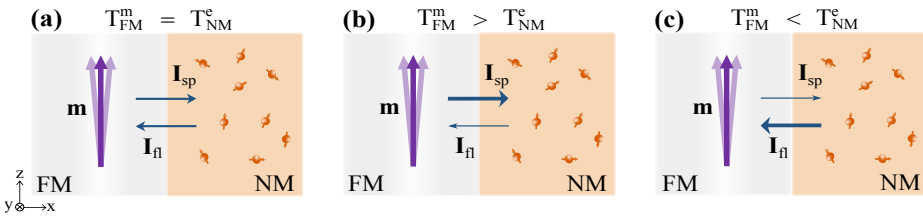

Figure 2.8. Schematic illustration of thermal spin pumping. The magnetization **m** gets thermally activated at temperature T^{m}_{FM} and pumps a spin current $\boldsymbol{I}_{sp}$ from the FM to the NM. In addition, the thermally activated electron spins in the NM at temperature T^{e}_{NM}, exert a fluctuation torque $\boldsymbol{I}_{fl}$ on **m**. The total spin current crossing the NM/FM interface is $\boldsymbol{I}^{z}_{s} = \boldsymbol{I}_{sp} + \boldsymbol{I}_{fl}$. (a) At thermal equilibrium $\boldsymbol{I}^{z}_{s} = 0$. (b) At $T^{m}_{FM} > T^{e}_{NM}$, $\boldsymbol{I}_{sp} > \boldsymbol{I}_{fl}$. (c) At $T^{m}_{FM} < T^{e}_{NM}$, $\boldsymbol{I}_{sp} < \boldsymbol{I}_{fl}$.

a single domain and can be regarded as a macrospin $\boldsymbol{M} = M_s V \boldsymbol{m}$, where V is the volume of the FM and $\boldsymbol{m}$ is the unit vector parallel to the magnetization. At equilibrium, $\boldsymbol{M} \| \hat{z}$. At a non-zero temperature, the magnetization is thermally activated and, thus, $\frac{d\boldsymbol{m}}{dt} \neq 0$. As discussed in the previous paragraph, the electrons in the NM and the magnetization in FM can exchange angular momentum through the STT and the spin pumping. Here, the different quasiparticles subsystems such as, electrons, magnons, and phonons, are characterized by different temperatures which need to be defined. Therefore, we consider T^{p}_{FM}, T^{e}_{FM}, and T^{m}_{FM} for the temperature of phonons, electrons, and magnons in the FM, respectively. Similarly, we consider T^{p}_{NM} and T^{e}_{NM} for the temperature of phonons and electrons in the NM. Moreover, we assume a strong electron-phonon interaction, whereas the magnon is weakly coupled with the other subsystems. Hence, $T^{e}_{FM} = T^{p}_{FM} \equiv T_{FM}$ and $T^{e}_{NM} = T^{p}_{NM} \equiv T_{NM}$.

On the one hand, under the application of a thermal gradient, magnetization dynamics get thermally activated pumping a spin current into the NM which is described by the Eq. (2.18) and can be equally written as [55]

$$\boldsymbol{I}_{sp}(t) = \frac{M_s V}{\gamma} \alpha' \boldsymbol{m}(t) \times \frac{d\boldsymbol{m}(t)}{dt}, \tag{2.20}$$

where $\alpha' = \frac{\gamma\hbar}{4\pi M_s V} \mathrm{Re}(G^{\uparrow\downarrow})$ describes the magnetic damping contribution caused by spin pumping and V is the total FM volume.

On the other hand, at finite temperatures electron spins in the NM fluctuate as well, exerting a random torque on the FM magnetization. The exerted

torque is described by the random magnetic field $\boldsymbol{h}(t)$ explained in the Eq. (2.16) and can be formulated as [55]

$$\boldsymbol{I}_{\mathrm{fl}}(t) = -\frac{M_{\mathrm{s}}}{\gamma}\gamma \boldsymbol{m}(t) \times \boldsymbol{h}(t), \tag{2.21}$$

where $\boldsymbol{I}_{\mathrm{fl}}(t)$ is called Johnson-Niquist spin current noise. Consequently, the total spin current flowing across the NM/FM interface is given by

$$\boldsymbol{I}_{\mathrm{s}}(t) = \boldsymbol{I}_{\mathrm{sp}}^{\mathrm{tot}}(t) + \boldsymbol{I}_{\mathrm{fl}}(t) = \frac{M_{\mathrm{s}}}{\gamma}\left[\alpha' \boldsymbol{m}(t) \times \frac{d\boldsymbol{m}(t)}{dt} - \gamma \boldsymbol{m}(t) \times \boldsymbol{h}(t)\right]. \tag{2.22}$$

Both $\boldsymbol{I}_{\mathrm{sp}}(t)$ and $\boldsymbol{I}_{\mathrm{fl}}(t)$ are illustrated in Fig. 2.8. From the Eqs. (2.20) and (2.21), we realize that the $\boldsymbol{I}_{\mathrm{sp}}(t)$ depends on how strongly $\boldsymbol{m}$ fluctuates, or equivalent on the magnon temperature $T_{\mathrm{FM}}^{\mathrm{m}}$, whereas the $\boldsymbol{I}_{\mathrm{fl}}(t)$ depends on the electron temperature in the NM, $T_{\mathrm{NM}}^{\mathrm{e}}$. In a non-equilibrium state, since $\boldsymbol{M} \| \hat{z}$ the $\hat{x}$ and $\hat{y}$ components of the $\boldsymbol{I}_{\mathrm{s}}(t)$ vanish due to the symmetry and, thus, $I_{\mathrm{s}}^{z}(t)$ is the only non-zero component of $\boldsymbol{I}_{\mathrm{s}}(t)$. From Eq. (2.22), using the transverse magnetic susceptibility (within the macrospin model) and assuming the limit $t \to 0$, we derive the formula

$$I_{\mathrm{s}}^{z}(t) \propto T_{\mathrm{FM}}^{\mathrm{m}} - T_{\mathrm{NM}}^{\mathrm{e}}. \tag{2.23}$$

Equation (2.23) expresses the proportionality of the thermally driven spin current across the NM/FM interface, with the temperature difference between the magnons and electrons. We further conclude that when $T_{\mathrm{FM}}^{\mathrm{m}} > T_{\mathrm{NM}}^{\mathrm{e}}$ ($T_{\mathrm{FM}}^{\mathrm{m}} < T_{\mathrm{NM}}^{\mathrm{e}}$), the pumped spin current flows from the FM to the NM leading to a loss (gain) of angular momentum [see Figs. 2.8(b) and 2.8(c)]. In an equilibrium state, $T_{\mathrm{FM}}^{\mathrm{m}} = T_{\mathrm{FM}} = T_{\mathrm{NM}} = T_{\mathrm{NM}}^{\mathrm{e}}$ dictating that there is no net spin current flow across the NM/FM interface since the pumped spin current $\boldsymbol{I}_{\mathrm{sp}}(t)$ is cancelled out by the spin current noise (see Fig. 2.8). A quantitative study of the above analysis and the intermediate steps between Eqs. (2.22) and (2.23) are presented in Ref. [84]. Next, the generated total spin current flowing from the FM to the NM is converted into a charge current in the NM via ISHE according to Eq. (2.5). This approach concerns the interfacial contribution of the SSE as introduced above.

An intuitive formula of the SSE voltage V_{SSE} was proposed by Schreier *et al.* [104] based on the analysis of Xiao *et al.* [84]

$$V_{\mathrm{SSE}} = \frac{\mathrm{Re}(G^{\uparrow\downarrow})\gamma\hbar k_{\mathrm{B}}}{2\pi M_{\mathrm{s}} V_{\alpha}}(T_{\mathrm{FM}}^{\mathrm{m}} - T_{\mathrm{NM}}^{\mathrm{e}}) \cdot \frac{2e}{\hbar}\theta_{\mathrm{SH}}\rho L_{\mathrm{V}} \cdot \eta \cdot \frac{\lambda}{t}\tanh\left(\frac{t}{\lambda}\right), \tag{2.24}$$

where η stands for the correction factor of the back-flow spin $\boldsymbol{I}_{\mathrm{s}}^{\mathrm{back}}(t)$ and is defined as

$$\eta = \left[1 + 2\mathrm{Re}(G^{\uparrow\downarrow})\rho\lambda\frac{e^2}{\hbar}\coth\frac{t}{\lambda}\right]^{-1}. \tag{2.25}$$

Here, ρ is the electrical resistivity, L_{V} is the distance between the voltage contacts transverse to the magnetization orientation of the ferromagnet, λ is the spin diffusion length in the NM, t is the thickness of the NM, and V_{α} is the temperature-dependent magnetic coherence volume. The cube root of V_{α} which is correlated with the coherence length, reflects the finite stiffness of a magnetic system that parameterizes the range at which an applied perturbation is felt. In other words, a small coherence length allows a random field to have a larger effect on a smaller magnetic volume.

Bulk SSE contribution As previously mentioned, the underlying mechanism of the SSE is an issue strongly discussed within the research community. Besides the interfacial SSE contribution, recent publications [87–90] introduce a model for the longitudinal spin Seebeck effect in NM/FMI bilayers (both local and nonlocal geometries are examined) based on the bulk magnon spin current generated by a temperature gradient across the FMI layer. As reviewed by Rezende *et al*. [89], the generated bulk spin current is the sum of two parts. The first part concerns the direct propagation of magnons under the application of a temperature gradient from the hotter region of the system towards the colder one, affecting the local magnetization. Specifically, at the hotter end of the gradient the number of the local magnons is reduced and, thus, the local magnetization increases. Correspondingly, at the cold end of the system the arriving magnons from the hotter regions decrease the local magnetization. The second part describes an indirect generation of the spin current due to the spatial variation of the magnon accumulation.

Within the frame of a mathematical approach [89], the number of the thermally generated magnons in the whole volume V of the FMI layer is n_{k}, with wave vector $\mathbf{k}$ and energy $\varepsilon_{\mathrm{k}} = \hbar\omega_{\mathrm{k}}$. Their number in thermal equilibrium,

given by the Bose-Einstein distribution, is $n_{\mathrm{k}}^0 = 1/[\exp(\varepsilon_{\mathrm{k}}/k_{\mathrm{B}}T) - 1]$ and $\delta n_{\mathrm{k}}(\mathbf{r}) = n_{\mathrm{k}}(\mathbf{r}) - n_{\mathrm{k}}^0$ is their number in excess of equilibrium. Then, the bulk magnon spin current density with polarization along the z axis is given by [105]

$$\mathbf{J}^z_{\mathrm{s,bulk}} = \frac{\hbar}{(2\pi)^3}\int d^3k\mathbf{v}_{\mathrm{k}}[n_{\mathrm{k}}(\mathbf{r}) - n_{\mathrm{k}}^0], \tag{2.26}$$

where $\mathbf{v}_{\mathrm{k}}$ is the k-magnon velocity. The distribution of the magnon number under the presence of a temperature gradient can be identified via Boltzmann transport equation [106]. In the absence of external cases and considering the relaxation approximation we extract

$$n_{\mathrm{k}}(\mathbf{r}) - n_{\mathrm{k}}^0 = -\tau_{\mathrm{k}}\mathbf{v}_{\mathrm{k}}\nabla n_{\mathrm{k}}(\mathbf{r}), \tag{2.27}$$

where τ_{k} is the k-magnon relaxation time. Using the Eqs. (2.27) and (2.26) one can prove that the spin current is the sum of two parts, $\mathbf{J}^z_{\mathrm{s,bulk}} = \mathbf{J}^z_{\mathrm{s},\nabla T} + \mathbf{J}^z_{\mathrm{s},\delta n}$, with

$$\mathbf{J}^z_{\mathrm{s},\nabla T} = -\frac{\hbar}{(2\pi)^3}\int d^3k\tau_{\mathrm{k}}\frac{\partial n_{\mathrm{k}}^0}{\partial T}\mathbf{v}_{\mathrm{k}}(\mathbf{v}_{\mathrm{k}}\cdot\nabla T) \tag{2.28}$$

as the contribution of the flow of magnons due to the temperature gradient and

$$\mathbf{J}^z_{\mathrm{s},\delta n} = -\frac{\hbar}{(2\pi)^3}\int d^3k\tau_{\mathrm{k}}\mathbf{v}_{\mathrm{k}}[\mathbf{v}_{\mathrm{k}}\cdot\nabla\delta n_{\mathrm{k}}(\mathbf{r})] \tag{2.29}$$

as the contribution due to the spatial variation of the magnon accumulation.

Similarly to the previously analyzed SSE mechanism, the thermally pumped spin current at the NM/FMI interface is given by Eq. (2.18). In turn, the pumped spin current in the NM is converted into a voltage via the ISHE. In order to derive the longitudinal V_{SSE} in the frame of the bulk SSE contribution description, one should modify Eq. (2.24) by inserting the parameters which stem from the spacial variation of the magnon accumulation. An extended analysis of this approach can be found in Ref. [89].

Transverse spin Seebeck effect The SSE in the *transverse* configuration (TSSE), was first reported by Uchida *et al.* in 2008 [98] on $Ni_{81}Fe_{19}$ films, as

earlier introduced. The TSSE owes its name to the direction of the applied temperature gradient which is perpendicular (*transverse*) to the spin current flow. In the experiment's configuration of Uchida *et al*., a thermal gradient longitudinal to the film plane ($Pt/Ni_{81}Fe_{19}$ bilayer) and perpendicular to the spin injection into the Pt film is applied and the V_{SSE} across the Pt in the transverse direction with respect to the applied thermal gradient is measured. After the announced observation of TSSE in FMM, a number of groups have reported TSSE voltages in different materials, such as FM-semiconductors [100] and FMIs [99]. However, the origin of TSSE was in dispute within the scientific community which inevitably carried out further experimental research in the field of spin caloritronics. Several groups have conducted investigations on measuring or reproducing the TSSE in different kind of materials and most of the reports claimed no observation of TSSE or referred to parasitic contributions from side effects such as magnetothermopower or Nernst effects, which could lead to a misinterpretation of a TSSE signal [27, 31, 107–113].

Longitudinal spin Seebeck effect The transverse configuration of the SSE involves complicated temperature distribution manipulation and depends crucially on the choice of substrate [55]. In order to eliminate these kind of uncertainties and to overcome the obstacle of the non-reproducibility of the TSSE, a *longitudinal* configuration of the SSE (LSSE) defines a strong contribution towards this approach. In the LSSE configuration, a thermal gradient (usually applied out-of-plane) is the driving force for the generation of a parallel (*longitudinal*) spin current flowing into the NM with a magnetization dependent spin orientation. The V_{SSE} across the NM film is measured in the direction perpendicular to the thermal gradient and transverse to the applied external magnetic field [see Fig. 2.6(a)]. The V_{SSE} is derived from the voltage in saturation V_{sat} of the collected hysteresis curve, as depicted in Fig. 2.6(b). However, in this geometry, the SSE generated voltage is difficult to distinguish from an ANE. In 2010, Uchida *et al*. [114] reported LSSE measurements on Pt/YIG bilayers. Due to the lack of free charge carriers the LSSE in magnetic insulators is free from parasitic contributions, such as the anomalous Nernst effect, enabling the correct interpretation of the LSSE signal. This claim will be discussed later on in this thesis. In contrast to the dubious observation

of the TSSE, LSSE has widely been reproduced in different materials. For example, a group of publications have reported LSSE in FMIs, such as YIG and NFO [26, 29, 37], in conducting magnetite [30, 33], and in the metallic FM $Ni_{81}Fe_{19}$ [40].

Spin-dependent Seebeck effect Up to this point we discussed the SSE in terms of the generation of a spin voltage as a response to an applied temperature gradient. Recently, Bauer *et al.* [10] emphasized on the spin current generation via conduction-electron spin accumulation in FMM or FM-semiconductors, using the term *spin-dependent Seebeck effect* (SDSE) to separate it from the magnon-based SSE. In particular, considering NM/FM bilayer systems according to the classical thermoelectric effect the application of a thermal gradient $\boldsymbol{\nabla} T$ between the FM and NM causes a charge current which results in the generation of a conduction-electron spin current $\boldsymbol{I}_{\mathrm{c}}^{\uparrow} - \boldsymbol{I}_{\mathrm{c}}^{\downarrow}$ at the NM/FM interface [115]. The generated spin current is accompanied by a spin accumulation $\mu_{\mathrm{s}}^{\uparrow} - \mu_{\mathrm{s}}^{\downarrow}$. Then, the spin-dependent charge current density $\boldsymbol{J}_{\mathrm{c}}^{\uparrow\downarrow}$ is described as

$$\boldsymbol{J}_{\mathrm{c}}^{\uparrow\downarrow} = -\sigma_{\uparrow\downarrow}\left[\frac{1}{e}\boldsymbol{\nabla}\mu_{\mathrm{s}}^{\uparrow\downarrow} + S_{\mathrm{SDSE}}\boldsymbol{\nabla} T\right], \tag{2.30}$$

where $\mu_{\mathrm{s}}^{\uparrow\downarrow}$ is the spin-dependent electrochemical potential and S_{SDSE} stands for the spin-dependent Seebeck coefficient. However, in the SSE measurements included in this thesis we will not distinguish between SSE and SDSE in the conducting materials and, thus, we will use the term SSE throughout the thesis.

Spin Nernst effect It has been discussed that pure spin currents can be generated from spin orbit interactions in heavy-ion metals by driving a flow of conduction electrons, e.g., in the SHE. The thermal equivalent of the SHE regards the generation of a spin current perpendicular to a thermal gradient and is called *spin Nernst effect* (SNE). Theoretical discussions of the SNE can be found in the publications of Cheng *et al.* [116] and Liu *et al.* [117]. First experimental observations have been recently made by Sheng *et al.* [118] and Meyer *et al.* [119].

Spin Nernst magneto-thermopower Considering an induced spin current from a SHE to flow in the transverse direction of the applied thermal gradient in the NM, the ISHE leads to the conversion of this spin current into a charge current parallel to the thermal gradient direction. The combination of the SNE and the ISHE induces a thermopower contribution along the temperature gradient direction and this effect is called *spin Nernst magneto-thermopower* (SMTP). In NM/FMI bilayer systems the concept of the SMTP, in close analogy to the SMR, enables the manipulation of the spin angular momentum exchange between the spin current in the NM and the magnetization of the FMI via spin transfer torque, by controlling the orientation of magnetization in the FM. A recent analysis of the experimental detection of the SMTP is reported by Meyer *et al*. and can be found in Ref. [119].

2.5 Magnetic proximity effect

The *magnetic proximity effect* (MPE) is a feature of heterostructures consisting of layers with different functionalities and long-range magnetic orderings. Proximity between two of those layers can lead to an altering of their interfacial magnetic properties, due to the interfacial exchange coupling. Consequently, this would significantly influence the spin transport properties and give rise to additional phenomena that do not exist in the constituent materials in isolation. Therefore, MPE as a key element of spintronics, can modulate the functionality of future spintronic and spin caloritronic devices.

Static magnetic proximity effect The static MPE has been widely discussed since the 1950s and is generally attributed to the interfacial magnetic exchange coupling between two neighbouring materials. Thin film heterostructures and bilayers are favored configurations for investigating and employing MPE, because they provide control of the interface quality and can conveniently be integrated into several spintronic and spin caloritronic devices.

In 1973, M.J. Zuckermann [120] reported a theoretical analysis of proximity induced magnetization in a NM/FM system and later on several experimental studies supported his work. The ferromagnetic materials involved in such bilayer systems were usually picked from the 3d transition metals, such as Fe, Co, Ni, and their alloys. The paramagnetic material usually consisted

of a metal from the 4d transition group such as Ru, Rh, Pd [121, 122] and from 5d metals, such as Pt, Au, Ir, and W [123–125]. In addition, light transition metals such as V [126, 127] and Cr [128] have been reported to exhibit significant MPE when adjacent to a FM as well. The properties of the NM itself determine the possible generation of a spin polarization when it is in contact with a FM. The Stoner criterion of ferromagnetic instability [15] signifies the possibility of a material to get spin-polarized. In particular, materials which are in close vicinity to the Stoner criterion are likely to exhibit spontaneous magnetization. An empirical rule to identify this property of a material is the expression $I_F \cdot N(E_F) > 1$, where I_F stands for the exchange integral and $N(E_F)$ is the density of states at the Fermi level.

Pt has been employed as the paramagnetic component in the NM/FM bilayer systems that are discussed in this thesis. Pt is a highly attractive candidate material to be utilized in spintronic and spin caloritronic applications when considering its large spin orbit coupling. However, it's close proximity to the Stoner criterion ($I_F \cdot N(E_F) \approx 0.6$ in fcc and hcp phase [129]) renders Pt an easily spin-polarized material, which as a consequence opens up new perspectives, yet also bears challenges when investigating spin transport phenomena in NM/FM bilayer systems. Numerous publications revealed that the MPE in Pt can influence spin transport measurements in NM/FM bilayer systems, e.g., via contamination of the LSSE measurements with proximity-induced ANE [16–18] or in terms of parasitic anisotropic magnetoresistance contribution to the SMR signal [19]. Therefore, when exploiting Pt, its novel properties have to be considered carefully to avoid misinterpretation of the detected effects by evaluating the side contributions (proximity-induced phenomena).

A critical issue in this context is the possibility of a static MPE in NM/FMI systems. While theoretically the large band gap in FMIs prohibits a coupling of interface states around the Fermi level, static MPE can still occur in the FMI as long as additional states around the Fermi level are present, for example from defects and lattice imperfections or from interfacial roughness. So far, the question of the existence or absence of static MPE in NM/FMI bilayers is controversially discussed within the research community. By using x-ray based techniques, such as x-ray magnetic circular dichroism or x-ray resonant magnetic reflectivity, several groups identified or excluded the MPE in such systems. Lu *et al.* [130] reported an average magnetic moment of $0.054\,\mu_B$

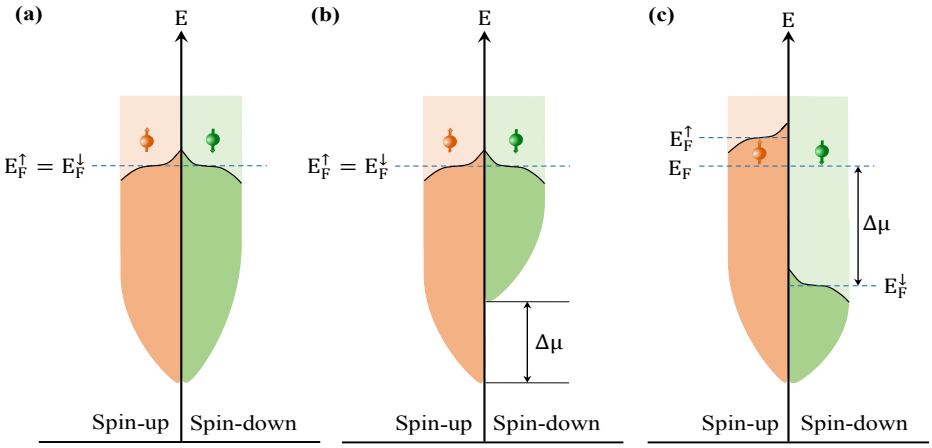

Figure 2.9. Qualitative draw of the energy band model in a NM (a) without spin polarization, (b) considering the concept of a static MPE, indicating the exchange splitting of the spin-up and spin-down channels, $\Delta\mu$ and, (c) under the concept of a non-equilibrium MPE.

per Pt atom at 300 K and 0.076 μ_B per Pt atom at 20 K, for 1.5 nm Pt on YIG. On the other hand, Geprägs *et al.* [131] did not find any evidence for an induced spin polarization in Pt on YIG as well as Kuschel *et al.* [37, 132] in Pt/$NiFe_2O_4$ bilayers, Valvidares *et al.* [133] in Pt/$CoFe_2O_4$ bilayers and Collet *et al.* [134] in Pt/$NiFe_2O_4$, Pt/$CoFe_2O_4$, Pt/$MnFe_2O_4$, and Pt/Fe_3O_4 systems. In a recent publication Kikkawa *et al.* [135] reported an induced paramagnetic moment in Pt on YIG equal to $(0.0212 \pm 0.0015)\,\mu_B$, extracted by x-ray magnetic circular dichroism measurements. They attributed the induced moment to the magnetic coupling between Pt and the interfacial magnetic moments at the Pt/YIG interface, whose magnetization process exhibits the paramagnetic behaviour. All these contradicting observations indicate that the magnetic properties of Pt strongly depend on the qualities of the Pt film and the Pt/FM interface.

In order to further elucidate the static MPE mechanism we should take a look at the bandstructure of the NM. In principle, the spin polarization in a material is a manifestation of an imbalance of the carrier distributions of spin-up and spin-down electrons. An imbalance in the carrier distributions can be generated either by unequal densities of states (DOSs) for the two spin channels or by shifted occupation functions of the spin resolved DOSs.

In the case of a static MPE, the spin polarization arises from a shift in the density of states by $\Delta\mu$ for one spin channel compared to the other. In the absence of an external magnetic perturbation, the ground state of the NM has an equal number of spin-up and spin-down electrons. Therefore, the density of states for spin-up electrons is equal to the density of states for spin-down electrons. In strongly correlated spin systems under the presence of a total magnetic field $\boldsymbol{B} = \mu_0(\boldsymbol{H} + \boldsymbol{M})$, the Hamiltonian term (Zeeman term) H_{Z} which provides the information for the spin-field interactions is given by

$$H_{\mathrm{Z}} = g_0 \mu_{\mathrm{B}} \mu_0 \boldsymbol{B}\boldsymbol{s}, \tag{2.31}$$

where g_0 is the Landé factor (≈ 2), μ_{B} is the Bohr magnetron, $\boldsymbol{H}$ is the external magnetic field, and $\boldsymbol{M}$ is the magnetization of the spin-polarized NM. In the absence of an external magnetic field $\boldsymbol{H}$ and assuming that $\boldsymbol{M} \| \boldsymbol{s}$, the Zeeman term introduces a relative shift of the DOS of the NM equal to

$$E_{\mathrm{shift}} = \Delta\mu = \mu_{\mathrm{s}}^{\uparrow} - \mu_{\mathrm{s}}^{\downarrow} = 2\mu_{\mathrm{B}} B = 2\mu_{\mathrm{B}}\mu_0 M, \tag{2.32}$$

as visible from the qualitative sketch in Fig. 2.9(b).

Non-equilibrium magnetic proximity effect In contrast to the well established static MPE the recently discovered SMR [60, 70, 72] and LSSE [114] can be understood as a non-equilibrium MPE. Different to the static MPE, non-equilibrium MPE manifest itself in the induced-spin polarization of a NM in a NM/FM bilayer system due to the application of an external stimuli, i.e., an applied electric current or a thermal gradient and not spontaneously. To further elucidate non-equilibrium MPE case, we should recall the concept of SMR and LSSE effects in NM/FMI bilayers, as described earlier in the theoretical part.

In the first case, the applied charge current through the NM is converted into a transverse spin current via SHE. The generated spin current builds up a spin accumulation in the interface and, therefore, a magnetization dependent absorption and reflection of this spin current from the FMI can occur. The "reflected" spin current is then converted into a charge current via ISHE in the NM leading to a detectable change of its longitudinal resistance, as described in Sec. 2.2. Thus, the transformation of the electronic properties of the

NM resulted as a consequence of the magnetic proximity to the FM and the external applied electric current.

In LSSE measurements, an out-of-plane thermal gradient is the driving force of an out-of-plane spin current from the FMI to the NM which piles up to a spin accumulation in the NM. Therefore, the applied thermal gradient leads to the altering of the magnetic properties of the NM, which can also be regarded as a non-equilibrium MPE.

In contrast to the static MPE, in the case of the non-equilibrium MPE there is no influence in the DOS, but the imbalance of the carrier distributions is an outcome of a change in the occupation function of spin-up and spin-down electrons, as sketched in Fig. 2.9(c). Therefore, this phenomenon leads to a spin polarization in the NM.

MPE in other bilayer systems Apart from NM/FM bilayer systems, MPE was also reported in other bilayer systems and heterostructures [136]. In 1999, Manago *et al*. [137] investigated NM/antiferromagnet (AFM) heterostructures. More specifically, they studied Pd(NM)/NiO(AFM) films and reported a magnetic moment of $0.59\,\mu_B$ per Pd atom. However, in 2001 Hoffmann *et al*. [138] showed that the Pd magnetic moment in Pd/NiO heterostructures could not exceed the value of $0.01\,\mu_B$ per Pd atom. In 2000, van der Zaag *et al*. [139] reported proximity induced magnetization in ferrimagnet/AFM systems. In particular, they investigated Fe_3O_4/CoO thin films and reported an enhancement of the Néel temperature of the AFM CoO layer above its bulk value (291 K), attributing this behaviour to a magnetic proximity of CoO to the ferrimagnetic Fe_3O_4 with it's higher Curie temperature of 858 K. Moreover, MPE was reported in AFM/AFM type NiO/CoO superlattices due to the presence of an interface exchange coupling between NiO and CoO by Borchers *et al*. [140].

Chapter 3

Experimental details

This chapter gives a brief introduction to the preparation of the films as well as the characterization techniques used in this project. All films were fabricated by dc magnetron sputtering, the structural analysis was performed utilizing x-ray diffraction/reflectivity and for the chemical composition analysis x-ray fluorescence was employed. The analysis of the magnetic properties was obtained by using the alternating gradient magnetometer and the magnetooptic Kerr effect. In addition, x-ray resonant magnetic reflectivity measurements were carried out at the XMaS beamline BM28 at ESRF (Grenoble, France) and at the resonant scattering and diffraction beamline P09 of the third generation synchrotron PETRA III at DESY (Hamburg, Germany), in order to study the MPE in the investigated NM/FM bilayer systems.

3.1 Fabrication of NM/FM bilayers

Apart from YIG, different insulating or semiconducting FMs from the group of spinel ferrites fulfill the requirements to be implemented in spin caloritronic devices. In particular, the high Curie temperatures ($T_C \approx 850\,K$) [141, 142] of spinel ferrites, such as NFO, render them attractive candidates for future applications. NFO in contact to a NM with a large SOC has already been employed in spin transport experiments for the detection of SMR and LSSE [27, 28, 37,

60, 96, 132, 143]. In this study, we partly focused on the fabrication and characterization of the spinel ferrite $NiFe_2O_x$ [144]. By reducing the oxygen content below its stoichiometric value (x=4), we varied the conductivity, the optical band gap, and the electrical transport mechanisms. Consequently, the variation in resistivity of such materials could lead to the manipulation and quantitative analysis of possible parasitic contributions of several phenomena, while studying the transport mechanisms in the fields of spintronics and spin caloritronics.

Ultra high vacuum reactive dc magnetron sputter deposition was utilized to fabricate the NM/FM bilayers. This process employs an electrically excited Ar plasma in a vacuum system. The choice of Ar as the process gas relies on its inert property which prohibits its reaction with the other constituents. The Ar^+ ions in the Ar plasma are accelerated toward the cathode, which upon bombardment ejects atoms from the cathode's surface. The ejected atoms collect on all surfaces including the substrate surface. The base pressure in a sputter deposition system is in the ultra high vacuum range to prevent from contamination of the fabricated films. The process pressure which allows for a stable plasma is usually of the order of $2 \cdot 10^{-3}$ mbar. Alternatively, a reactive sputtering process is used with an additional reactive gas, such as O_2 or N_2, in order to induce a reaction between the process gas and the sputter materials.

The $Pt/NiFe_2O_x$ ($4 \geq x \geq 0$) films were fabricated by co-sputtering from elemental Ni and Fe targets, starting from pure high-resistive $NiFe_2O_4$ ($\sim$ 160 nm) and by reducing the oxygen content during deposition we reached the metallic $Ni_{33}Fe_{67}$ (10.4 nm) with intermediate $NiFe_2O_{x_1}$ (60 nm) and $NiFe_2O_{x_2}$ (35 nm), with $4 > x_1 > x_2 > 0$. The films were deposited on top of (001)-oriented $MgAl_2O_4$ (MAO) substrates. The $Ni_{33}Fe_{67}$ film was deposited in Ar atmosphere with pressure in the range of $2 \cdot 10^{-3}$ mbar at RT. The $NiFe_2O_{x_1}$ and $NiFe_2O_{x_2}$ films were prepared in Ar and O_2 atmosphere at 610°C substrate temperature. For the $NiFe_2O_{x_1}$ bilayer the Ar partial pressure during the deposition was $1.7 \cdot 10^{-3}$ mbar, while the total one was $2 \cdot 10^{-3}$ mbar. For the $NiFe_2O_{x_2}$ bilayer the Ar partial pressure was $1.8 \cdot 10^{-3}$ mbar, while the total one was $2.3 \cdot 10^{-3}$ mbar. The pure NFO was grown in pure O_2 atmosphere with a pressure of $2 \cdot 10^{-3}$ mbar at 610°C substrate temperature. The base pressure in all cases was less than 10^{-8} mbar.

Twin FM layers were prepared with and without Pt in-situ deposited on top, by covering one FM layer with a mask to obtain the same deposition conditions

for the FM in both samples. The Ar pressure during the deposition for the Pt layers was equal to $2 \cdot 10^{-3}$ mbar. The appropriate sputter parameters were adjusted after evaluating the x-ray fluorescence measurements to achieve the desired stoichiometry. The final Fe:Ni ratios were extracted to be equal to 2.00, 1.95, and 1.87 for NFO, $NiFe_2O_{x_1}$, and $NiFe_2O_{x_2}$ samples, respectively, very close to the correct stoichiometric compositions. We collected the x-ray fluorescence data until the error of the corresponding composition becomes equal to 1% in all cases. The crystallographic properties of the films were evaluated using x-ray diffraction in a Bragg Brentano configuration. The oxygen content could not be derived quantitatively due to the insensitivity of the fluorescence detector regarding oxygen.

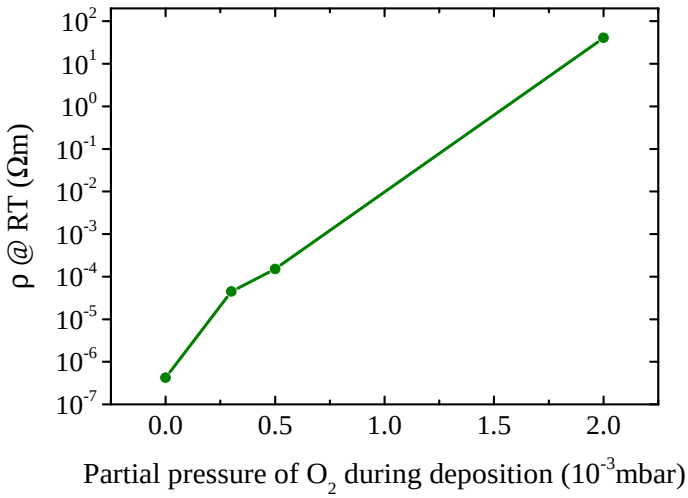

Figure 3.1. Resistivity measured at RT for the corresponding partial O_2 pressure of all $NiFe_2O_x$ samples.

Figure 3.1 represents the change of RT resistivity according to the partial O_2 pressure during deposition. The partial O_2 pressure was calculated from the partial Ar and total pressures, recorded during the deposition of each sample. A clear increase of the resistivity is observed when the amount of oxygen increases.

For the NM/FMM bilayers, i.e., $Pt/Co_{1-x}Fe_x$ with $x = 0.00, 0.15, 0.30, 0.50, 0.67, 1.00$ and $Pt/Ni_{1-x}Fe_x$ with $x = 0.00, 0.19, 0.30, 0.50, 0.67, 1.00$ sample series, we again utilized dc magnetron co-sputter deposition and the twin

samples (with and without Pt deposited on top) were grown on top of (001)-oriented MgO substrates at RT. As previously mentioned, the x-ray fluorescence data served to quantify the Ni:Fe and Co:Fe ratios and the crystallographic properties of the films were evaluated using x-ray diffraction. The Ar pressure during the deposition for all FMM and Pt layers was equal to $2 \cdot 10^{-3}$ mbar and the base pressure was $3 \cdot 10^{-9}$ mbar. The thickness of the FMM and Pt layers was (9.1 ± 0.9) nm and (3.05 ± 0.15) nm, respectively.

3.2 X-ray based techniques

X-rays were first discovered by the German Physicist Wilhelm K. Röntgen for which he was awarded the Nobel Prize in 1901 [145]. Since then, they have revolutionized the world of solid state physics with their implementation in a wide variety of characterization techniques. Their non-destructive nature renders them an unbeatable tool for the investigation of the crystal and electronic structure (XRR, XRD, XANES, EXAFS, angle-resolved XPS etc.) as well as the composition (XRF, XPS etc.) of the material of interest.

3.2.1 X-ray diffraction

X-ray diffraction (XRD) is used to investigate qualitatively and quantitatively the structural properties of solids. In our experiments, XRD measurements were carried out in a Philips X'pert pro MPD diffractometer (Cu K_α $\lambda = 1.5419$ Å) which was equipped with a Bragg-Brentano geometry. In particular, the x-rays of wavelength λ are diffracted by the planes of a crystal and for a defined family of planes with Miller indices (hkl) and interplanar distance d_{hkl}, the diffraction will be constructive if the angle θ of the incident beam with respect to the surface of the film satisfies Bragg's law [146]. This is given by the formula

$$n\lambda = 2d_{\mathrm{hkl}}\sin\theta, \tag{3.1}$$

with n as an integer. The distance d_{hkl} between two sequential parallel planes with (hkl) indices, will be equal to the distance between the origin and its closest crystal plane. When the axes compose an orthogonal basis (orthorhombic symmetry) the interplanar distance is obtained by

$$d_{\mathrm{hkl}} = \left(\frac{h^2 + k^2 + l^2}{a^2 + b^2 + c^2} \right)^{1/2}, \tag{3.2}$$

with a, b, c as the lattice parameters.

In order to achieve a deeper insight of the physical mechanisms and finally visualize the crystal structure, the crucial parameter of the structural factor F(hkl) is necessary to be analyzed. The F(hkl) of each plane can be considered as the sum of the atomic factors f_{i} of each atom, multiplied by a phase factor $e^{-i\boldsymbol{rq}}$, such that $F(hkl) = \sum_{i=1}^{n} f_{\mathrm{i}} e^{-i\boldsymbol{rq}}$, with $\boldsymbol{r}$ as the position vector of each atom and $\boldsymbol{q}$ as the scattering vector. Simultaneously, the intensity of the XRD spectrum I_{hkl} is proportional to the $|F(\mathrm{hkl})|^2$, according to the Laue conditions. The conversion of F(hkl) into atomic coordinations is achieved using the Fourier transformation which connects the electronic density with the F(hkl) via the relation $\rho(\boldsymbol{r}) = \sum_{hkl} F(hkl) e^{-2\pi(hx+ky+lz)}$. Consequently, this unveils the distribution of the atoms in the unit leading to a visualization of the structure of the crystal.

3.2.2 X-ray reflectivity

X-ray reflectivity (XRR) is employed for the characterization of surfaces and interface of multilayer heterostructures. A typical XRR scan can provide information on the thickness, roughness, density, and optical properties for each layer in a multilayer system. In particular, the XRR interference pattern concerns an XRD spectrum in Bragg-Brentano geometry ($\theta/2\theta$, cf. Fig. 3.2) at very small angles ($2\theta < 5°$). The incoming x-rays with wave vector $\boldsymbol{k}_{\mathrm{i}}$ and incidence angle θ are reflected at the sample surface and interfaces and the interference of the outcoming results in an oscillation pattern. This characteristic pattern consists of the so-called Kiessig fringes whose periodicity and shape yield information about the structural parameters of the probed sample. In particular, the layer thickness can be obtained by the formula [147]

$$d = \frac{\lambda(m-l)}{2(\sin(\theta_m) - \sin(\theta_l))}, \tag{3.3}$$

for oscillation maxima/minima of order m and l and the corresponding angular positions θ_m and θ_l, respectively. When probing rough surfaces/interfaces the reflected intensity is reduced due to diffusive scattering of the x-ray beam.

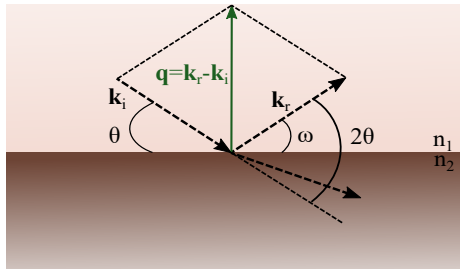

Figure 3.2. An incident wave with wave vector $\boldsymbol{k}_\mathrm{i}$ and incident angle θ is partially transmitted and reflected at an interface between two optically dissimilar media with refractive indices n_1 and n_2. The reflected wave is characterized by the wave vector $\boldsymbol{k}_\mathrm{r}$ and reflection angle equal to $\omega = \theta$. The scattering vector $\boldsymbol{q} = \boldsymbol{k}_\mathrm{r} - \boldsymbol{k}_\mathrm{i}$ can be considered as the momentum transfer.

The scattering vector $\boldsymbol{q}$ concerns the difference between the reflected $\boldsymbol{k}_\mathrm{r}$ and incident $\boldsymbol{k}_\mathrm{i}$ wave vectors, as depicted in Fig. 3.2 and, thus, can be considered as the momentum transfer. It is always perpendicular to the surface and varies during XRR measurements by changing the incident angle θ while keeping $\theta = \omega$. In addition, its amplitude is given by $q = \frac{4\pi}{\lambda} \sin\theta$ [148].

The complex refractive index for the incoming monochromatic x-rays is given by

$$n = 1 - \delta + i\beta, \tag{3.4}$$

with the dispersion and absorption terms [149]

$$\delta = \frac{\lambda^2}{2\pi} r_\mathrm{e} \rho_\mathrm{e} \tag{3.5}$$

and

$$\beta = \frac{\lambda}{4\pi} \mu, \tag{3.6}$$

respectively. Here, r_e concerns the classical electron radius, ρ_e is the electron density, and μ regards the absorption coefficient. The dispersion part is a positive number of the order of 10^{-6} [149] and, therefore, for x-rays the real

part of the complex refractive index n is always slightly smaller than unity. The absorption part β is usually one or two orders of magnitude smaller. As a result, considering x-ray reflection at the interface between vacuum/air and matter, below a critical angle θ_c the x-rays do not penetrate inside the material and undergo a total reflection. Above θ_c, the x-rays are partially transmitted and the reflected intensity decreases exponentially. The critical angle is an element-specific parameter ($\theta_c \approx \sqrt{2\delta}$) yielding information about the film's density (by neglecting the absorption part, $\beta = 0$) [146].

In this thesis, as for the XRD case the XRR scans were collected in a Philips X'Pert Pro diffractometer with a Cu K_α source. To obtain the required structural properties, the Parratt algorithm [150] was used to fit numerically the XRR data. For the analysis, information about the material's composition is required and the layer thickness, roughness, and mass density are fit parameters.

3.2.3 X-ray fluorescence

X-ray fluorescence (XRF) is a powerful, non-destructive tool, ideally suited for the quantitative and qualitative elemental analysis of materials. In this thesis, the chemical composition of the films was adjusted using XRF with an Ag tube as x-ray source. It is crucial to note that since the penetration length for XRF is of about 1 μm, the substrate is critical when investigating thin films of the order of some nm. Thus, the thin films should be of the order of 100 nm thick to reduce the errors originating from the impurities in the substrate. Prior to the sample fabrication, test films have been deposited on amorphous fused silica substrates (in order to further reduce the unwanted peaks due to diffraction on crystalline substrates) and analyzed by XRF regarding their chemical composites. After adjusting the correct sputter rates based on the XRF results, the final samples have been deposited on the individual substrates (MgO, MAO, etc.).

An intuitive analysis of the XRF technique is as follows. The atoms in the film under the illumination by x-rays eject electrons from the lower (e.g. K and L) energy levels. The ionized electrons are replaced by electrons from an outer orbital with higher energy. Consequently, the binding energy of the inner-orbital electron is decreased compared to an outer one and energy is released. This energy release is in the form of emission of characteristic x-rays, unveiling the type of atom present in the film. In addition, this released

energy quantum may not be emitted from the atom but it can excite an Auger electron. The recombination probability of an outer-orbital electron with an inner-orbital hole is proportional to the square of the nuclear charge Z^2. Due to the reduced absorption cross section of the light elements ($Z < 30$), a reasonable application of the fluorescence process is limited to the heavier ones [151].

The spectra were collected utilizing an AMPTEK XR-100CR Si-PIN detector and a digital pulse processor under He atmosphere. The samples were analyzed in a He atmosphere in order to avoid any absorption of the characteristic emission of light elements by air that could hamper the observations. The characteristic peaks were evaluated after the removal of the background, escape and sum peaks, and smoothing the spectrum, allowing for the underlying composition of the irradiated material to be determined. Usually, integrating for more than one hour results in accuracy of $\leq 1\,\%$ atomic content.

3.2.4 X-ray magnetic circular dichroism

In optics, the term "dichroism" refers to changes in the absorption of polarized light on passing through a material in two different directions. So far, x-ray magnetic circular dichroism (XMCD) has been implemented for the analysis of magnetic properties of several materials, extracting the absolute magnetic moment per atom of each element. In a typical XMCD experiment, circularly polarized x-rays are employed and the energy dependant absorption spectra across the $L_{2,3}$ absorption edges of the FM are collected, by changing the helicity of x-rays with respect to the direction of an externally applied magnetic field or vice versa. The application of photon energies around resonant absorption edges ($L_{2,3}$) of the investigated material, implies the high element specificity of the technique. The XMCD signal is given by the formula [148]

$$I_{\mathrm{XMCD}} = I_+ - I_- \propto \boldsymbol{P}\boldsymbol{M}, \tag{3.7}$$

where $I_\pm$ stands for the measured intensity when the helicity of the x-rays is parallel or antiparallel with the magnetic field, $\boldsymbol{P}$ is the photon polarization vector, and $\boldsymbol{M}$ is the magnetization vector.

More specifically, an incident x-ray beam with photon energy close to the binding energy of the probed material, can cause the excitation of the strongly localized core electrons into energetically higher levels in the conduction band.

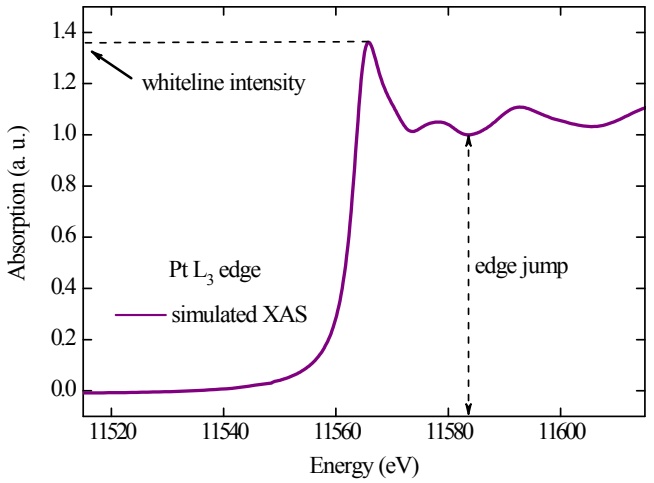

Figure 3.3. Normalized L_3 absorption edge of Pt calculated theoretically [152]. The ratio of absorption maximum and edge jump indicates the whiteline intensity.

Such excitations at these specific energies are reflected by sharp peaks in the x-ray absorption spectrum (XAS) of the material, the well known absorption edges (see Fig. 3.3). The absorption edges are denoted as K (1s), L (2s and 2p), and M (3s, 3p, and 3d), depending on the principal quantum number of the core level where the electrons have been excited. For example, L_2 and L_3 absorption edges describe the transitions from $2p_{1/2}$ and $2p_{3/2}$, respectively. In principle, a XAS spectrum apart from the absorption edge should include both pre-edge and post-edge absorption features, yielding information about the electronic properties, the local geometry of the absorbing atom, etc. The theoretically calculated XAS for the L_3 edge of Pt is drawn in Fig. 3.3, as simulated by Dr. Markus Meinert [132].

Several publications have reported the use of XMCD as a mean to investigate the MPE in Pt on FMMs [153–160], allowing to extract the absolute magnetic moment per atom of each element. Apart from FMMs, XMCD has been used to investigate the spin polarization in Pt on FMIs [130, 131, 133, 134], an issue which is controversially discussed, as explained in Sec. 2.5.

Electromagnetic radiation which is emitted from accelerated electrons or other charged particles when moving at relativistic speed on curved trajectories, is called *synchrotron radiation*. Nowadays, many synchrotron radiation

facilities are built causing an explosive growth in the use of synchrotron radiation for element specific characterization of the magnetic properties of materials.

3.2.5 X-ray resonant magnetic reflectivity

The examination of spin-polarized interfaces with regard to static MPE (see Sec. 2.5), necessitates the investigation of interfaces which are located far from the surface in the sample's volume. Unfortunately, XMCD strongly depends on the film thickness since a large fraction of the sample's volume contributes to the measured signal, introducing difficulties in the static MPE analysis of films thicker than a few nm. A much younger technique to detect the magnetic properties of layer systems with element- and depth-sensitivity, is the x-ray resonant magnetic reflectivity (XRMR). XRMR is based on the spin-dependent interference of the light reflected from the interfaces in the system which renders this method independent from the layer thickness (as long as the absorption in the layers is small), compared to XMCD [132, 148]. In a typical XRMR experiment, the helicity of the circularly polarized x-rays or the orientation of the externally applied magnetic field is switched for each incidence angle from left-handed to right-handed or from positive to negative, respectively.

A fundamental theoretical background for the XRMR includes the determination of the optical properties of a material exposed to x-rays of the element's absorption energy as given in the refractive index n. When the magnetization is aligned in opposite directions or the helicity of the x-rays is reversed, the optical parameters δ and β vary by a fraction $\pm\Delta\delta$ and $\pm\Delta\beta$, respectively, due to the magnetic circular dichroism in the material. These so-called magnetooptic parameters are most pronounced at energies right around the absorption edge of the investigated material and vanish far from the resonance. Therefore, the XRMR data are collected by performing XRR scans at a fixed energy close to the absorption edge of the probed material. The change in the optical parameters with the magnetization orientation regarding the x-ray helicity is interpreted as a change of the detected reflectivities. Hence, a suitable measure in order to investigate and quantify the interface magnetization is the asymmetry ratio given by the formula

$$\Delta I = \frac{I_+ - I_-}{I_+ + I_-}, \tag{3.8}$$

with $I_\pm$ to be the XRR intensity for opposite magnetization directions or different x-ray helicities. The degree of circular polarization should always be estimated. As an example, the spin polarization in Pt has been examined in Pt/NFO and Pt/$Ni_{1-x}Fe_x$ bilayers [37, 132, 144, 161], providing information about the spatial distribution of the spin polarization of Pt, across the interface to a FM.

In this thesis, the fitting tool ReMagX [148] is used to evaluate the magnetic XRMR asymmetry ratio ΔI plotted over the scattering vector amplitude q. A recipe procedure for the determination of the induced magnetic moment by evaluation of XRR and XRMR data is included in Ref. [161]. A brief summary of this routine is as follows. In the first step of the experimental data processing, the structural parameters (thickness, roughness) are obtained from the fittings of the off-resonant non-magnetic XRR curves, using the tabulated values for the optical parameters δ and β according to the Henke tables [162]. In turn, the curves are fitted using the Parratt algorithm and the structural parameters extracted from the fittings are used to fit the resonant XRR curves and determine the optical parameters in resonance. Afterwards, the XRMR asymmetry ratios are simulated using the previously derived parameters along with the variation of magnetooptic depth profiles for the magnetooptic parameters $\Delta\delta$ and $\Delta\beta$. Finally, by comparing the resulting $\Delta\delta$ and $\Delta\beta$ values to optical data from *ab initio* calculations [132], the magnetic moment per spin-polarized NM atom is identified.

3.3 Magnetization measurements

The alternating gradient magnetometer (AGM) has proved to be a vigorous and versatile tool for the study of the magnetic properties of materials, such as remanent magnetization, saturation magnetization, coercivity, etc. In this thesis, the magnetization measurements were performed using the Micromag 2900 Alternating Gradient Magnetometer from Princeton Measurements Corporation, a highly-sensitive measurement system. This system utilizes optimized gradient coils in conjunction with small high performance electromagnets and an advanced pulse-width modulated bipolar magnet power

supply, to achieve high sensitivity. Magnetic fields up to 14 kOe can be applied with the electromagnet and the field is measured with a Hall probe.

In particular, the sample is mounted in the center between the electromagnets. The application of a field occurs, e.g. B_z, together with a well-defined alternating field gradient, e.g. b_z, on the sample. This is accompanied with a simultaneous alternating force on the sample which is described by the relation [163]

$$F_z = m_z B_z \frac{\partial b_z}{\partial z}, \tag{3.9}$$

where m_z is the z-component of the magnetization. The applied force causes displacements of the sample from the center, which can be detected by an attached mechanically compliant system (piezoelectric element). The piezoelectric element produces a voltage proportional to the displacement of the sample. In turn, the amplitude of this voltage is analogous to the magnetic moment of the sample.

3.4 Magnetooptic Kerr effect

The magnetooptic Kerr effect (MOKE) is a well established technique and has attracted significant scientific interest while used extensively to investigate the magnetic properties of thin films, e.g., coercivity, magnetization reversal properties, magnetic anisotropies, etc. The Kerr effect is also the basis of the commercially available magnetooptic drives. The MOKE was discovered by John Kerr in 1877 [164] during his investigations of the polarization of light reflected from a polished electromagnet pole. It describes the change of the polarization states of light when reflected by a magnetic material. In principle, any linearly polarized wave can be described as a superposition of a left- and a right-circularly polarized component having the same phases and amplitudes. The reflection of this linearly polarized wave from a magnetized sample can cause a phase shift resulting in the Kerr rotation of the polarization principal axis of the incident wave, while a change in the amplitudes of the two components causes the Kerr ellipticity.

There are three different configurations for MOKE depending on the relative orientation of the magnetization direction with respect to the surface plane and the plane of incidence. The first one is the *polar* Kerr effect configuration

where the magnetization lies perpendicularly to the sample surface and parallel to the plane of incidence. The second one corresponds to the *longitudinal* Kerr effect where the magnetization lies in-plane to the sample surface and parallel to the plane of incidence. Last, in the *transverse* configuration the magnetization lies in-plane to the sample surface and perpendicular to the plane of incidence. In this thesis, we utilized the longitudinal configuration to investigate the magnetic anisotropy of FMM bilayers.

3.5 Optical absorption

The optical properties were investigated via ultraviolet-visible (*UV-Vis*) spectroscopy in the range of (1.0-4.1) eV (1200-300) nm, in a Perkin Elmer Lambda 950 Spectrometer. Both reflection and transmission spectra were recorded in order to extract the absorption coefficient and derive the optical band gap energies of the films. The energy-dependent absorption coefficient α(E) was extracted from the measured transmission T and reflection R spectra using [165]

$$\alpha = \frac{1}{d}\ln\frac{1-R}{T}, \tag{3.10}$$

where d is the thickness of the corresponding layer.

A common way to determine the minimum gap from the optical absorption spectra is by evaluating Tauc plots as explained in Ref. [152]. The indirect gap can be extracted from straight line segments in $(\alpha E)^{0.5}$ plotted over energy E. However, the determination of the band gap using Tauc plots could lead to rough estimated values because of the uncertainties that may come up during this kind of data processing [152].

3.6 Temperature gradient setup

The LSSE measurements were carried out in a vacuum furnace, as depicted in Fig. 3.4, at RT. To collect the LSSE voltage applying an out-of-plane temperature gradient in the presence of an in-plane magnetic field, the samples were clamped between two copper blocks from their top and bottom sides, in in-plane magnetized (IPM) configuration. The copper block on the top

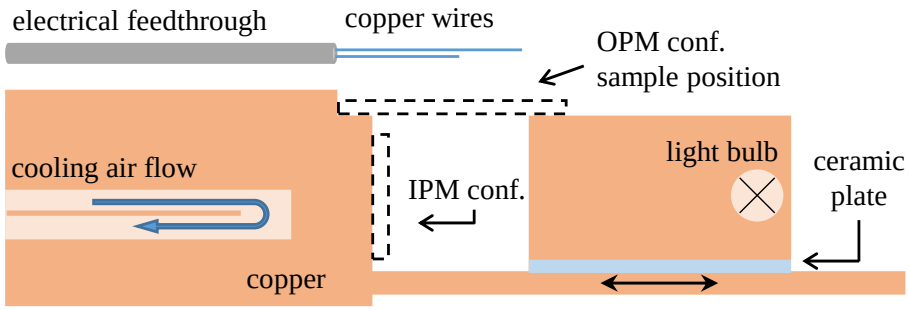

Figure 3.4. Schematic illustration of the vacuum furnace indicating the sample positions in the IPM and OPM configurations.

side of the sample acted as a heat source using a light bulb and the one on the bottom side of the sample acted as a heat sink. In between the right copper block and the sample there was an additional sapphire (Al_2O_3) layer with a thickness of 0.5 mm, in order to prevent from electrical contacting between those two parts. A small amount of thermal grease (titanium dioxide paste with thermal conductivity equal to $K = 0.82\,\mathrm{Wm^{-1}K^{-1}}$) was introduced in between the parts of the setup which were in direct contact e.g., copper blocks, sample, sapphire layer. The introduction of thermal grease retained the thermal stability which could be disturbed by the presence of roughness between the materials.

In case of studying the heat flux (see analysis in Sec. 5.1), a Peltier element was placed in between the right copper block and the upper side of the film, acting as a heat flux sensor. The Peltier elements were calibrated by using an electric heater resistor to simulate a Joule heat source as described by Sola *et al.* [29, 166]. Then, an out-of-plane thermal gradient was homogeneously applied to the film via utilizing and controlling a heat resistor, see Fig. 3.4. The temperature difference between the two copper blocks was measured by two K-type thermocouples. The two thermocouples were placed in a region which was in thermal equilibrium (hot and cold baths). For the voltage measurements, two aluminum or gold wires 25 μm thick were bonded on top of the samples and glued properly with silver paste to copper wires that are connected to the electrical feedthroughs of the vacuum chamber. The voltage contacts were in the same plane but in transverse direction to the applied magnetic field. Also, the collected output signal of the sensor after

the measurement was converted into heat flux by taking into account the cross section area of the heat between the sample and the Peltier element, as will be explained in Sec. 5.1.

The ANE measurements were performed in the aforementioned setup, but in a different geometry. In this case, we exchanged the directions of the external magnetic field (out-of-plane) and the thermal gradient (in-plane), by placing the samples in a different configuration in the setup, out-of-plane magnetized (OPM) configuration (see Fig. 3.4). The samples were placed on top of the two copper blocks. As previously, in order to detect the heat flux, a Peltier element was placed in the cold side between the sample and the left copper block. The sample was clamped with a copper plate on the top hot side (right copper block), in order to drive the thermal gradient homogeneously along the sample. In the cold side, the sample was free from clamping to avoid heat losses through the copper plate to the rest of the setup, which could influence the voltage output of the Peltier element and, thus, underestimate the heat flux. As in the IPM configuration, thermal grease was introduced in between the parts of the setup which were in direct contact as well as two aluminum or gold wires were bonded on top of the sample and glued with silver paste to the copper wires of the setup. The voltage contacts were on the same plane but in transverse direction to the applied temperature gradient.

At this point, it's crucial to mention that in the OPM configuration the heat flux was determined by taking into account the thermal conductivity of the FM and NM layers used in the bilayer. The procedure to estimate the thermal conductivities was as follows. Since in the OPM configuration the Peltier element was placed below the substrate, considering the thermal conductivity of the different used substrates ($K_{\mathrm{MAO}} = 24\,\mathrm{Wm^{-1}K^{-1}}$ [167] and $K_{\mathrm{MgO}} = 30\,\mathrm{Wm^{-1}K^{-1}}$ [168]) in Eq. (5.2) we extracted the temperature difference (ΔT) along the substrate. Further, we considered the same ΔT among all the layers. The main contribution to the total heat flow resistance of the sample came from the substrate since this was the thickest part of the bilayer. However, in our measurements we were only interested in the contribution of the FM layer in which the effects are generated. The thermal conductivities of the $NiFe_2O_x$ ($x > 0$) layers are assumed to be $(8.5 \pm 0.9)\,\mathrm{Wm^{-1}K^{-1}}$ [169], since all of these samples are in the non-conducting regime at RT. The error is introduced since the absolute value of the thermal conductivity corresponds to a bulk material and not to thin films.

In the NM/FMM bilayer systems the thermal conductivity K_{FMM} contains two contributions

$$K_{\mathrm{FMM}} = K_{\mathrm{e}} + K_{\mathrm{ph\text{-}m}}, \tag{3.11}$$

with K_{e}: thermal conductivity of free electrons and $K_{\mathrm{ph\text{-}m}}$: thermal conductivity of phonons and magnons. The value of K_{e} is calculated from the Wiedemann-Franz law

$$K_{\mathrm{e}} = L\,\sigma\,T, \tag{3.12}$$

with σ: the measured electrical conductivity at each temperature T and L=2.44$\cdot 10^{-8}\,\mathrm{W\Omega K^{-2}}$: the Lorentz number. The value of $K_{\mathrm{ph\text{-}m}}$ ranges between $(7.9 \pm 0.8)\,\mathrm{Wm^{-1}K^{-1}}$ and $(8.4 \pm 0.8)\,\mathrm{Wm^{-1}K^{-1}}$ for all $Co_{1-x}Fe_x$ and $Ni_{1-x}Fe_x$ layers according to literature [170–173]. In the cases of induced spin polarization in Pt, we additionally considered the contribution to the heat flux from the spin-polarized Pt layer, with effective thickness extracted from the XRMR investigations (see Chap. 6), according to the Wiedemann-Franz law.

3.7 Further characterization techniques

3.7.1 Hall effect measurements

For the investigation of the semiconducting-like behaviour of our samples, the evaluation of the Hall resistance as well as the determination of the carrier densities and mobilities, we performed Hall effect measurements in a closed-cycle helium cryostat. The samples were patterned into a Hall-bar geometry with a length of 1000 μm and a width of 75 μm via optical lithography (identical to the one used in Ref. [60]) and a subsequent argon ion beam milling. Each sample was glued to a chip-carrier sample holder and the contacts of the Hall bar structure were connected to the bonding frame of the sample holder with aluminum wires 25 μm thick, via wedge bonding. The geometry of the measurements is displayed in Fig. 4.5(a) in Sec. 4.4. A charge current was flowing along the y axis in the presence of an out-of-plane magnetic field up to 4 T and the voltages along the x and y axis were recorded. The measurements were collected in vacuum atmosphere at RT.

3.7.2 Temperature dependent electrical resistivity

In order to investigate the conduction mechanisms governing our systems in a certain temperature range and to determine some physical quantities such as the thermal activation energy, we studied the temperature dependence of the electrical resistivity. The measurements were performed in temperature ranges of (40 − 330) K, using a closed-cycled helium cryostat. For that reason the samples were patterned into a Hall bar, as described in the previous paragraph. The resistance was determined by applying a constant current and collecting the longitudinal voltage in a two-point probe technique, using a Keithley 2000.

Chapter 4

Physical properties of $NiFe_2O_x$ thin films

This chapter includes measurements of the $NiFe_2O_x$ film properties which allowed us to identify the structural, magnetic, electrical, and optical behaviour of the films. By reducing the oxygen content below its stoichiometric value ($x = 4$) we were able to vary the conductivity, the band gap, and the electrical transport mechanisms. In particular, XRD analysis unveiled the structural properties of the films and the saturation magnetization was studied to further evaluate the quality of them. From the temperature dependent electrical resistivity measurements, we examined the disorder of our films and obtained the conduction mechanisms that govern the systems in high and low temperature regimes. We further investigated the Hall coefficient and the mobilities of the samples by performing Hall effect measurements which revealed the semiconductor type of our thin films. Ultraviolet-visible spectroscopy was utilized to estimate the optical band gap. The results were published in Ref. [174] and the corresponding sections are based on this publication.

4.1 XRD measurements

Figure 4.1(a) illustrates the results of $\theta - 2\theta$ measurements for the $NiFe_2O_x$ ($4 \geq x > 0$) samples. In the XRD patterns, (004) Bragg peaks are visible for

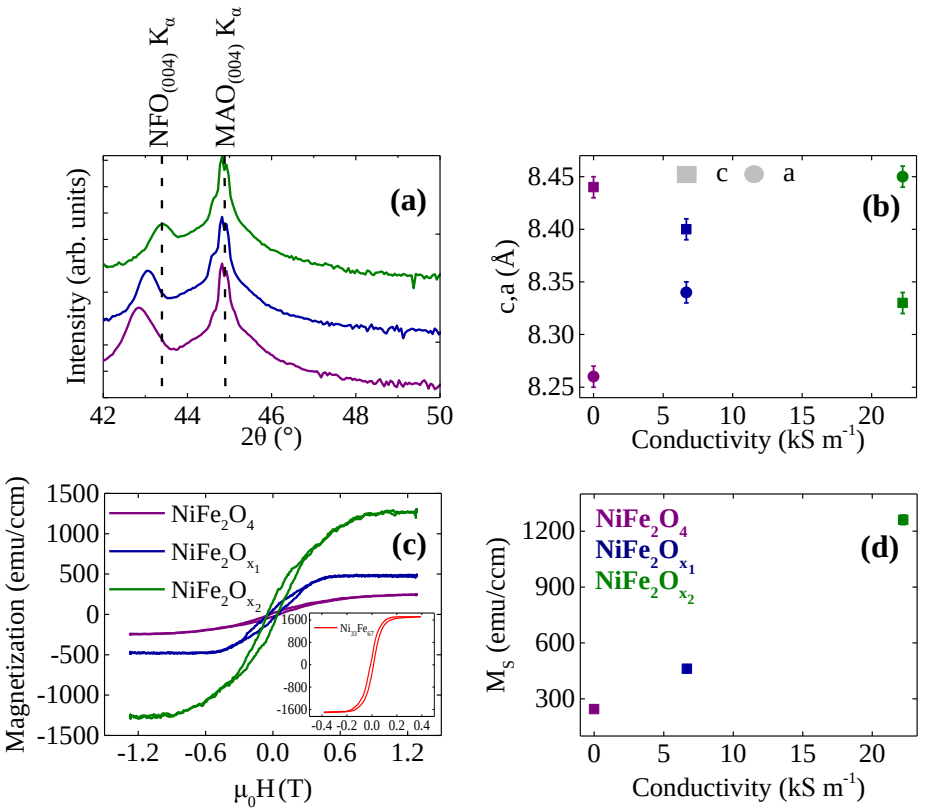

Figure 4.1. (a) XRD patterns for $NiFe_2O_4$, $NiFe_2O_{x_1}$, and $NiFe_2O_{x_2}$ samples. (b) Out-of-plane *c* and in-plane *a* lattice parameters plotted against the conductivity at RT for all films. (c) Magnetization curves collected via AGM. A linear diamagnetic background was subtracted. The inset of the figure indicates the hysteresis loop for the metallic $Ni_{33}Fe_{67}$ sample. (d) Saturation magnetization M_S acquired at 1.3 T plotted against the conductivity.

all samples showing a crystalline structure with epitaxial growth in [001] direction. From the peak positions in the XRD patterns the out-of-plane lattice parameters *c* can be derived. Additionally, the in-plane lattice parameters *a* can be identified from the position of the (606)-Peak ($2\theta \approx 103°$), which is observable with off-specular $\omega - 2\theta$ measurements and an ω-offset of $\Delta\omega \approx 45°$ (this is analog to an eccentric tilt of the sample around the [010] MAO

direction by $\Delta\omega$). The obtained out-of-plane and in-plane lattice parameters are presented in Fig. 4.1(b) as a function of the conductivity for all samples.

For NFO, a tetragonal distortion is visible which is in agreement with epitaxial strain due to the lattice mismatch between NFO and the MAO substrate, since $a_{\mathrm{MAO}} = 8.08\,\text{Å}$. Specifically, the film is expanded in the direction perpendicular to the surface ($c_{\mathrm{NFO}} > c_{\mathrm{bulk}}$) and compressed in the film plane ($a_{\mathrm{NFO}} < a_{\mathrm{bulk}}$). The bulk lattice parameter for NFO equal to $a_{\mathrm{bulk}} = 8.34\,\text{Å}$ is taken from Ref. [175]. In order to quantify the strain effect in the film, the Poisson ratio is commonly used. From the formula [176]

$$\nu = -\frac{\epsilon_{\mathrm{oop}}}{\epsilon_{\mathrm{ip}}} = \frac{(c - \mathrm{a_{bulk}})}{(\mathrm{a} - \mathrm{a_{bulk}})}, \tag{4.1}$$

where ϵ_{oop} is the out-of-plane strain and ϵ_{ip} is the in-plane strain, we extracted a positive strain equal to $\nu = 1.25$. This value comes in line with Fritsch and Ederer [177] who reported a value of $\nu \approx 1.2$, for NFO with in-plane compressive strain. The unit cell volume is reduced by about 1% with respect to bulk material. For the other two $NiFe_2O_x$ films, the in-plane lattice parameters increase and the out-of-plane ones decrease, compared to NFO. However, no further conclusion can be drawn for these samples since the corresponding bulk values of the lattice parameters are not known and may differ from the ones of the NFO.

Moreover, by performing ω-scans around the (004) Bragg peak of our $NiFe_2O_x$ samples (not shown) we obtained a full width of half maximum equal to 1.2°, 0.6°, and 0.7° for NFO, $NiFe_2O_{x_1}$, and $NiFe_2O_{x_2}$, respectively. These values are slightly higher but still comparable to previous publications on NFO films prepared by pulsed laser deposition [178].

4.2 Magnetic measurements

Figure 4.1(c) illustrates the magnetization plotted against the magnetic field as extracted from the AGM measurements. The plots are presented after the subtraction of diamagnetic contributions. In the magnetic field of 1.3 T, the $NiFe_2O_{x_1}$, $NiFe_2O_{x_2}$, and $Ni_{33}Fe_{67}$ samples are clearly saturated. In contrast, for the NFO sample, we reached 88% of saturation in the applied magnetic

field. The saturation value was estimated from the AHE measurements with the application of a field strength equal to 4 T (see Sec. 4.4).

Figure 4.1(d) shows the saturation magnetization M_S as a function of the conductivity for all samples. For the NFO, the M_S value equal to 244 emu/ccm (in 88 % saturation state) is consistent to earlier publications [165]. Moreover, it is clearly observed that the magnetization increases with the increase in conductivity. One possible explanation for the increased magnetization is a higher ratio between magnetic ions and the non-magnetic oxygen in the lattice. This increased Fe and Ni density enables a larger moment per f.u. Additionally, deviations from the default $NiFe_2O_4$ stoichiometry potentially reduce the antiferromagnetic coupling between tetrahedral and octahedral lattice sites, leading to a larger net moment.

4.3 Electrical resistivity measurements

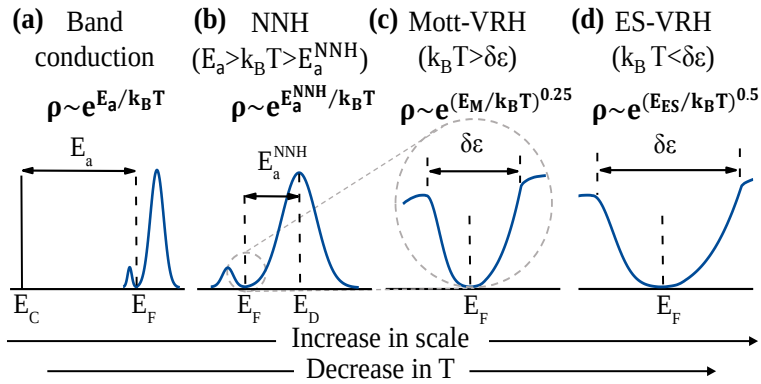

Figure 4.2. Conductivity mechanisms as a function of the temperature decrease representing qualitatively the DOS in a lightly doped semiconductor. (a) Band conduction. (b) Nearest-Neighbour hopping (NNH). (c) Mott-Variable Range Hopping (Mott-VRH). (d) Efros-Shklovskii-Variable Range Hopping (ES-VRH).

In a generalized picture the electrical conduction in semiconductors consists of two types, the band and hopping conduction. Figure 4.2 represents the sequence of conductivity mechanisms replacing one by another as a function of the temperature decrease in a lightly doped (n-type) semiconductor [179]. This sequence includes the assumption that the Fermi level E_F is located

Table 4.1. Summary of different conduction mechanisms which take place in semiconductors with the corresponding characteristic energy E_t and the value of the exponent P from Eq. (4.2).

Conduction mechanism	Characteristic energy E_t	Exponent P
Band conduction	E_a	1
NNH	$E_a^{NNH} < E_a$	1
Mott-VRH	$E_M = k_B T_M$	0.25
ES-VRH	$E_{ES} = k_B T_{ES}$	0.50

in the impurity band of the localized states of a doped semiconductor. A lower temperature value is balanced with a smaller section of the energy scale to distinguish between the different transitions of the carriers for the corresponding applied energy $k_B T$. In band conduction, charge carriers from localized states are thermally activated and transported to delocalized states, as visible in Fig. 4.2(a). The highest energy at which states are still localized defines a mobility edge. The universal equation which describes the temperature dependent electrical conductivity in semiconductors is given by

$$\sigma(E) = \sigma_0 \exp\left[-\left(\frac{E_t}{k_B T}\right)^P \right], \tag{4.2}$$

where σ_0 is a pre-exponential factor, E_t is the transition energy, k_B is the Boltzmann constant, and $P\,(>0)$ is the characteristic exponent. The value of the exponent P distinguishes between different conduction mechanisms by expressing the profile of the DOS. In band conduction, P=1 and E_t corresponds to the thermal activation energy for the delocalization of carriers E_a, as summarized in Table 4.1. E_t is given by either $E_C - E_F$ or $E_F - E_V$, depending on whether electrons or holes are the charge carriers of the material. E_C, E_V, and E_F are the mobility edges of the conduction band, the valence band, and the Fermi energy, respectively.

In hopping conduction, charge is transported through localized states in the vicinity of E_F [cf. Figs. 4.2(b)-4.2(d)]. The conductivity is defined by electrons hopping directly between localized states in the impurity band, without any excitation to the conduction band since they have insufficient energy for this transition. Therefore, the free electron band conduction is less important in

this case [180]. In this regime, there are two types of conduction mechanisms, the Nearest-Neighbour Hopping (NNH) and the Variable Range Hopping (VRH). In NNH, the hopping conductivity is expressed by transitions between the nearest neighbours [Fig. 4.2(b)]. The DOS in the donor impurity band at low donor concentration is maximum when the energy is of the order of the ionization energy of an isolated donor, E_D. When the initial and final states of such a transition are among the nearest neighbours, it is most probable that the corresponding energy levels are in the vicinity of the maximum DOS. The necessary condition for the NNH conduction to occur, is the existence of a large number of pairs of close neighbour states, with one of them being free. The corresponding probability of this free state (for an n-type semiconductor) depends on its energy with respect to the Fermi level and is proportional to

$$\exp\left(\frac{-|E_F - E_D|}{k_B T}\right). \tag{4.3}$$

Then, from the general semiconductor equation [Eq. (4.2)], E_t is now symbolized as E_a^{NNH} and corresponds to the thermal activation energy having a smaller value compared to the energy required for thermally activated band conduction (E_a), as summarized in Table 4.1.

In systems with only small disorder, the further decrease of temperature such that $k_B T << |E_F - E_D|$, causes the number of empty states among the nearest neighbours to be significantly small and, therefore, the electron hopping will take place between free states localized in the vicinity of the Fermi level symbolized by $\delta\varepsilon$. The average hopping length depends on temperature and the conduction mechanism changes from NNH to VRH. When the VRH dominates the conduction, the condition $0 < P < 1$ for the exponent P in Eq. (4.2) is fulfilled. The VRH model was firstly proposed by Mott [181] when he considered a constant density of states $N(E)$ near E_F, claiming that the Coulomb interaction of electrons is weak and can be neglected. Thus, he showed that the value of the exponent P in Eq. (4.2) is equal to 0.25 and the transition energy E_t is given by $E_M = k_B T_M$ [cf. Fig. 4.2(c)]. E_M defines the energy that corresponds to the characteristic Mott temperature T_M, as described in Table 4.1. T_M can be correlated to the localization length L_c via the formula

$$T_M = \frac{18}{L_c^3 N(E_F) k_B}. \tag{4.4}$$

However, Efros and Shklovskii [180] later on suggested that at low enough temperatures for highly disordered systems, $N(E)$ cannot be considered constant anymore, but behaves as $N(E) \propto (E - E_F)^2$. This behaviour derives from the energetic insufficiency of the system to overcome the electron-hole Coulomb interaction arising from the movement of the electron from one state to the other. This vanishing DOS is called Coulomb gap. In the Efros-Shklovskii-VRH (ES-VRH) conduction regime [Fig. 4.2(d)], the exponent P is equal to 0.5. Moreover, E_t is now given by $E_{ES} = k_B T_{ES}$, where E_{ES} is the energy that corresponds to the characteristic Efros-Shklovskii temperature T_{ES}, as included in Table 4.1. T_{ES} is given by

$$T_{ES} = \frac{2.8\, e^2}{\epsilon\, L_c\, k_B}, \tag{4.5}$$

where ϵ is the dielectric constant and e is the electron charge. At intermediate disordered systems, there may be a crossover from ES- to Mott-VRH with increasing temperature.

In our systems from highly resistive to semiconducting-like $NiFe_2O_x$, we expect to observe different conduction mechanisms that contribute in the examined temperature range. Figures 4.3(a) and 4.3(b) illustrate the electrical resistivity ρ as a function of temperature, ranging between $(100-330)$ K for NFO, $(60-330)$ K for $NiFe_2O_{x_1}$, and $(40-330)$ K for $NiFe_2O_{x_2}$. The expected semiconducting behaviour with increasing resistivity for decreasing temperature is clearly observed in all cases. In order to investigate the conduction mechanisms governing our systems, we first considered the simplest form of thermal activation process. The temperature dependent resistivity can be described by the Arrhenius law which corresponds to $P = 1$ in Eq. (4.2), as included in Table 4.1. The required energy for the thermally activated charge transport can be derived by a linear regression of the temperature dependent resistivity. Figures 4.3(c) and 4.3(d) show the Arrhenius plot of $\ln(\rho)$ vs. $1000/T$ for all samples. The experimental data was fitted with the electrical resistivity relation extracted from Eq. (4.2) for P=1, in order to determine the thermal activation energy. In the high temperature regime the straight line segments fit the data closely. The black arrows indicate the lowest tem-

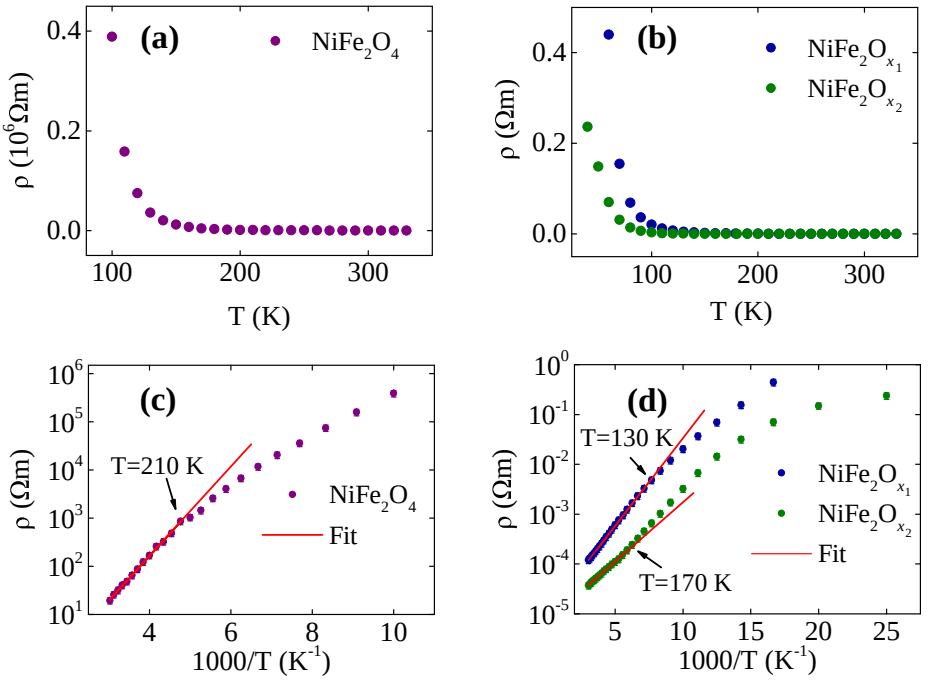

Figure 4.3. (a),(b) Temperature dependence of the resistivity and (c),(d) Arrhenius plots for $NiFe_2O_4$, $NiFe_2O_{x_1}$, and $NiFe_2O_{x_2}$ samples, respectively. In the high temperature regime, the straight line segments fit the data closely indicating the validity of Arrhenius law. The black arrows note the lowest temperature point included in the linear fit.

perature point included in the linear fit. Consequently, the thermal activation energy value for NFO was found to be equal to $E_a^{NFO} = 0.19\,eV$. This result is in accordance with our previous investigations on sputter-deposited and chemical vapor deposited NFO [143, 165], as well as the values found by Lord and Parker in sintered NFO specimens, Austin and Elwell in NFO single crystals, and Ponpandian et al. in NFO nanoparticles [182–184]. For the $NiFe_2O_{x_1}$ and $NiFe_2O_{x_2}$ films, we found $E_a^{NiFe_2O_{x_1}} = 0.07\,eV$ and $E_a^{NiFe_2O_{x_2}} = 0.05\,eV$, respectively. The thermal activation energy is lower in the more conducting samples reflecting the additional electronic states localized in the band gap which contribute to the measured resistivity.

On the contrary, in the low temperature regime the plots show significant deviations from the straight lines, as visible in Figs. 4.3(c) and 4.3(d). This

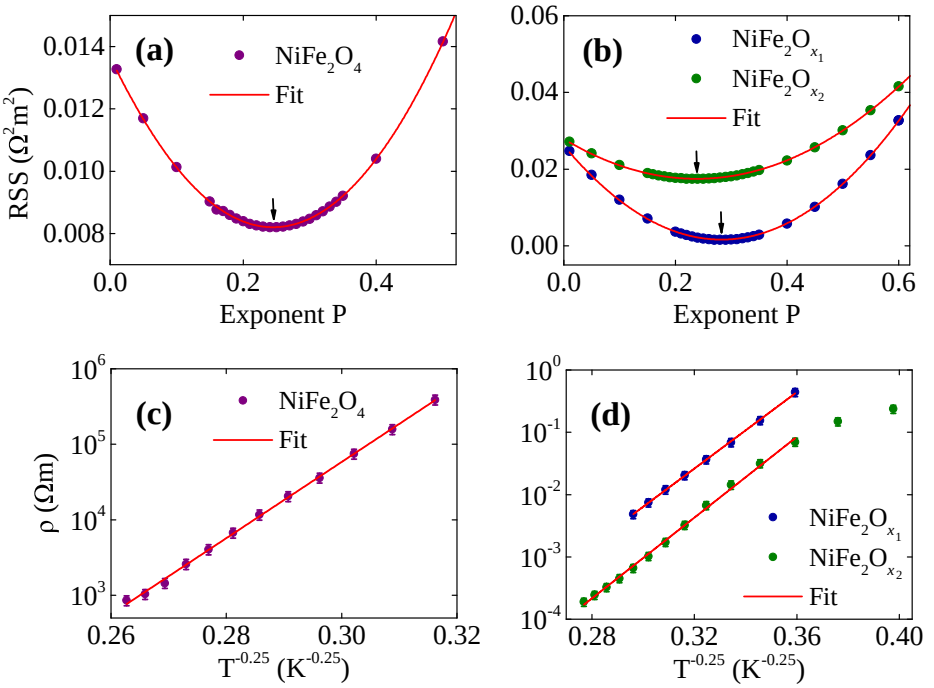

Figure 4.4. (a),(b) Plot of the residual sum of squares (RSS) against the exponent P from Eq. (4.2) fitted with parabolas for $NiFe_2O_4$, $NiFe_2O_{x_1}$, and $NiFe_2O_{x_2}$ samples. The black arrows denote the minimum of the parabola fit indicating which conduction mechanism governs the measurements in the low temperature regimes. (c),(d) Temperature dependence of the resistivity in the Mott-VRH regime.

behaviour suggests that the conduction mechanism in which the carriers are thermally activated and jump over a certain semiconductor energy barrier cannot be the dominant one and a crossover between two mechanisms is reasonable. In order to determine with sufficient accuracy which conduction mechanism governs the resistivity, we plotted the data in low temperature regimes $\ln(\rho)$ vs. T^{-P}, where we varied the exponent P from 0.1 to 1 (with outer steps of 0.05 and inner steps of 0.01 near the minimum). We fitted the data by straight line segments and we plotted the residual sum of squares (RSS) versus the exponent P. From the parabola fits we extracted the appropriate exponent P which minimizes the RSS leading to the best fitting.

Figures 4.4(a) and 4.4(b) illustrate the RSS as a function of the exponent P in the low temperature regimes, $(100-210)$ K for NFO, $(60-130)$ K for

$NiFe_2O_{x_1}$, and (60−170) K for $NiFe_2O_{x_2}$. All curves were fitted with parabolas to estimate the minimum of the corresponding curve with high precision. The black arrows indicate the minimum of the parabola fit. We found that the minimum of the RSS is P=0.25 for NFO, P=0.28 for $NiFe_2O_{x_1}$, and P=0.24 for $NiFe_2O_{x_2}$. Thus, we deduce that the values of P are 0.25 or very close to it indicating the existence of Mott-VRH conduction in the low temperature regimes. This suggests an almost constant DOS near E_F. Figures 4.4(c) and 4.4(d) show $\ln(\rho)$ plotted against $T^{-0.25}$, according to the Mott model, with the corresponding linear fits indicating that Mott-VRH model describes accurately the data in the low temperature regimes. The characteristic Mott temperature T_M is extracted from Eq. (4.2), with P=0.25. For the $NiFe_2O_{x_2}$ sample, the two last points at 50 K and 40 K were left out from the fitting, since those points present a second change in the slope of the curve in the low temperature dependent resistivity. This behaviour could also indicate a possible transition between Mott-VRH and ES-VRH at even lower temperatures. However, this assumption requires further investigation in lower temperature ranges. The values of ρ at RT, E_a, and T_M are summarized in Table 4.2 for all samples. The Mott temperature T_M increases with increasing resistivity, as reported in Table 4.2, indicating that the quantity $N(E_F)L_c^3$ [see Eq. (4.4)] is smaller. This behaviour is expected since in the most resistive samples, $N(E_F)$ has a smaller value as well.

Table 4.2. Resistivity ρ collected at RT, thermal activation energy E_a, and characteristic Mott temperature T_M extracted from the linear fits in Figs. 4.3 and 4.4.

Film	ρ (Ωm)	E_a (eV)	T_M (K)
$NiFe_2O_4$	40.5	0.19	5264
$NiFe_2O_{x_1}$	1.5×10^{-4}	0.07	2482
$NiFe_2O_{x_2}$	4.5×10^{-5}	0.05	2400

4.4 Hall measurements

In order to extract the semiconductor type of our films, we performed Hall effect measurements according to the geometry displayed in Fig. 4.5(a). A

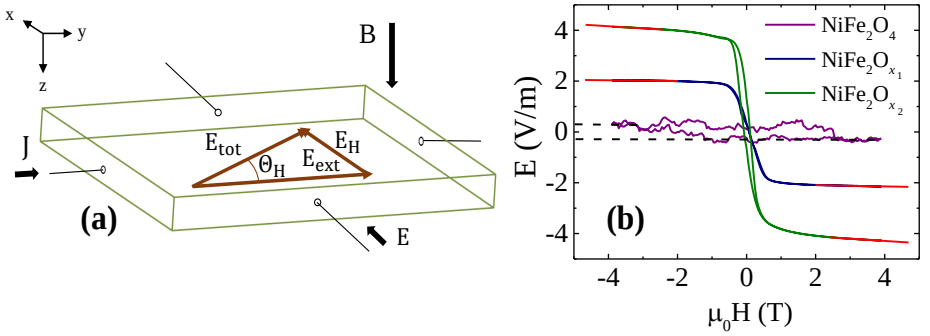

Figure 4.5. (a) Schematic illustration of Hall effect geometry. (b) Hall effect measurements for $NiFe_2O_4$, $NiFe_2O_{x_1}$, and $NiFe_2O_{x_2}$ samples. From the slope of the fitting curves, the Hall coefficient is extracted.

charge current was flowing along the y axis in the presence of an out-of-plane magnetic field, and the voltages along the x and y axes were recorded. Figure 4.5(b) displays the detected electric field E along the x-axis plotted against the applied external magnetic field for the NFO, $NiFe_2O_{x_1}$, and $NiFe_2O_{x_2}$ samples. Both curves for $NiFe_2O_{x_1}$ and $NiFe_2O_{x_2}$ show a slope changing linearly with the field in the region where the magnetization dependent AHE saturates. This can be attributed to the OHE. Since the presented curves are free from symmetric contributions, no symmetrization of the curves is needed. The corresponding values were extracted by fitting the positive and negative saturation regimes and, afterwards, averaging the individual slopes. From the slopes of the linear fits the OHE coefficient R_{H} can be extracted by using

$$\mathbf{E}_{\mathrm{H}} = R_{\mathrm{H}}(\mathbf{J} \times \mathbf{B}), \tag{4.6}$$

where $\mathbf{E}_{\mathrm{H}}$ is the OHE field, $\mathbf{J}$ is the charge current density, and $\mathbf{B}$ is the external magnetic field. Considering the geometry displayed in Fig. 4.5(a), the Hall coefficient is given by

$$R_{\mathrm{H}} = \frac{E_{\mathrm{H,x}}}{J_{\mathrm{y}} B_{\mathrm{z}}} \tag{4.7}$$

and taking into account the slope of the linear fits A_{OHE} extracted from the curves, R_{H} is modified to

$$R_H = \frac{A_{OHE}}{J_y}. \tag{4.8}$$

For a charge current density of $J_y = 1.04 \times 10^7\,A/m^2$ ($17.86 \times 10^7\,A/m^2$) and a slope of $A_{OHE} = -0.0256\,V/Tm$ ($A_{OHE} = -0.0870\,V/Tm$) for the $NiFe_2O_{x_1}$ ($NiFe_2O_{x_2}$) sample, we can extract the corresponding Hall coefficient. We find, $R_H^{NiFe_2O_{x_1}} = -24 \times 10^{-10}\,m^3/C$ and $R_H^{NiFe_2O_{x_2}} = -4.9 \times 10^{-10}\,m^3/C$ for the $NiFe_2O_{x_1}$ and $NiFe_2O_{x_2}$ samples, respectively. The sign of the extracted Hall coefficients indicates n-type semiconducting behaviour of our samples. These results are in accordance with the n-type behaviour reported for nanocrystalline nickel ferrite [185]. However, the large resistivity of the NFO makes the measurements challenging and prevents us from reliably determining the Hall coefficient and the semiconducting behaviour for this sample [see Fig. 4.5(b)].

Furthermore, the density of the carries n is given by the formula

$$R_H = -\frac{r}{ne}, \tag{4.9}$$

where r is the ratio between the Hall mobility μ_H and the drift mobility μ_D which is usually set equal to 1 (for further analysis see Sec. 2.2). Considering the aforementioned R_H, we find $n = 2.6 \times 10^{27}\,m^{-3}$ ($n = 12.7 \times 10^{27}\,m^{-3}$) for the $NiFe_2O_{x_1}$ ($NiFe_2O_{x_2}$) sample. The latter expresses higher carrier density value which is consistent with its higher conductivity value compared to the $NiFe_2O_{x_1}$ sample. The carrier density values that we obtain are relatively large but still within the limit of possibility for semiconducting materials such as In_2O_3:Sn exhibiting values of $n \approx 10^{27}\,m^{-3}$ [186] and even higher values of $n \approx 10^{28}\,m^{-3}$ in nanocrystalline nickel ferrite [185].

The relatively low R_H values leading to comparably high charge carrier densities could also indicate a mixed-type of semiconducting behaviour. In order to further elucidate this issue we investigated the ordinary Nernst coefficients D_{ONE} of the samples. In general, D_{ONE} for a mixed-type semiconductor is given by Eq. (2.14). As briefly analyzed in Sec. 2.3, if there is one-carrier system we expect to find quite small numbers (of the order of some nV/TK) for D_{ONE}, or instead, large numbers (of the order of some mV/TK) for a mixed-type semiconductor [79]. From our investigations on the transport properties of these samples (see Sec. 5.4), we extracted Q_N while performing ANE measurements.

The Nernst coefficient values were found to be equal to D_{ONE}=5.5 nV/TK and D_{ONE}=9.4 nV/TK for $NiFe_2O_{x_1}$ and $NiFe_2O_{x_2}$ samples, respectively, suggesting one carrier system. This result comes in line with the n-type semiconducting behaviour extracted from the Hall measurements.

As a next step, we obtain the drift mobility of electrons μ_{D} by the formula

$$\mu_{\mathrm{D}} = -R_{\mathrm{H}}\sigma_{\mathrm{n}}. \tag{4.10}$$

Considering, $\sigma_{\mathrm{n}} = 6.67\,\mathrm{kS/m}$ ($\sigma_{\mathrm{n}} = 22.22\,\mathrm{kS/m}$), we find $\mu_{\mathrm{D}} = 0.16\,\mathrm{cm^2/Vs}$ ($\mu_{\mathrm{D}} = 0.11\,\mathrm{cm^2/Vs}$) for the $NiFe_2O_{x_1}$ ($NiFe_2O_{x_2}$) sample. By comparing the two extracted mobility values, the latter is slightly lower indicating the presence of higher concentration of defects acting as scattering centers in the more conducting sample.

Furthermore, from the Hall effect geometry illustrated in Fig. 4.5(a), we can estimate the Hall mobility μ_{H}. The two components E_{H} and E_{ext} (the external electric field along the y axis) define a total electric field, E_{tot}. Then, E_{tot} is tilted according to the Hall angle, Θ_{H}. Consequently, the Hall mobility of the electrons μ_{H} is obtained by the formula

$$\tan\Theta_{\mathrm{H}} = \frac{E_{\mathrm{H,x}}}{E_{\mathrm{ext,y}}} = \mu_{\mathrm{H}} B_{\mathrm{z}}. \tag{4.11}$$

Taking into consideration that $B_{\mathrm{z}} = 4\,\mathrm{T}$, $E_{\mathrm{H,x}} = 0.10\,\mathrm{V/m}$ ($E_{\mathrm{H,x}} = 0.34\,\mathrm{V/m}$), and $E_{\mathrm{ext,y}} = 97.31\,\mathrm{V/m}$ ($E_{\mathrm{ext,y}} = 43.13\,\mathrm{V/m}$) for the $NiFe_2O_{x_1}$ ($NiFe_2O_{x_2}$) sample, we extracted the corresponding Hall mobility. We find, $\mu_{\mathrm{H}}^{NiFe_2O_{x_1}} = 2.6\,\mathrm{cm^2/Vs}$ and $\mu_{\mathrm{H}}^{NiFe_2O_{x_2}} = 19.7\,\mathrm{cm^2/Vs}$ for the $NiFe_2O_{x_1}$ and $NiFe_2O_{x_2}$ samples, respectively. At this point, it is crucial to underline the different μ_{D} and μ_{H} values. These discrepancies may have their origin in the unjustified assumption that the parameter r would be equal to 1 [see Eq. (4.9)]. The ratio of Hall to drift mobility ($\mu_{\mathrm{H}}/\mu_{\mathrm{D}}$) is in both cases larger than one. Similar discrepancies have also been reported in C.E. Turner *et al.* for iron rich nickel ferrites [187], where the ratio r varies systematically from 1.3 at high ferrous content to ∼11.0 at low ferrous content. We thus conclude in agreement with Ref. [187] that in a system with two antiparallel magnetic sublattices and hopping conduction (such as the investigated systems), the Hall- and the drift mobility cannot be expected to be equal.

4.5 Optical measurements

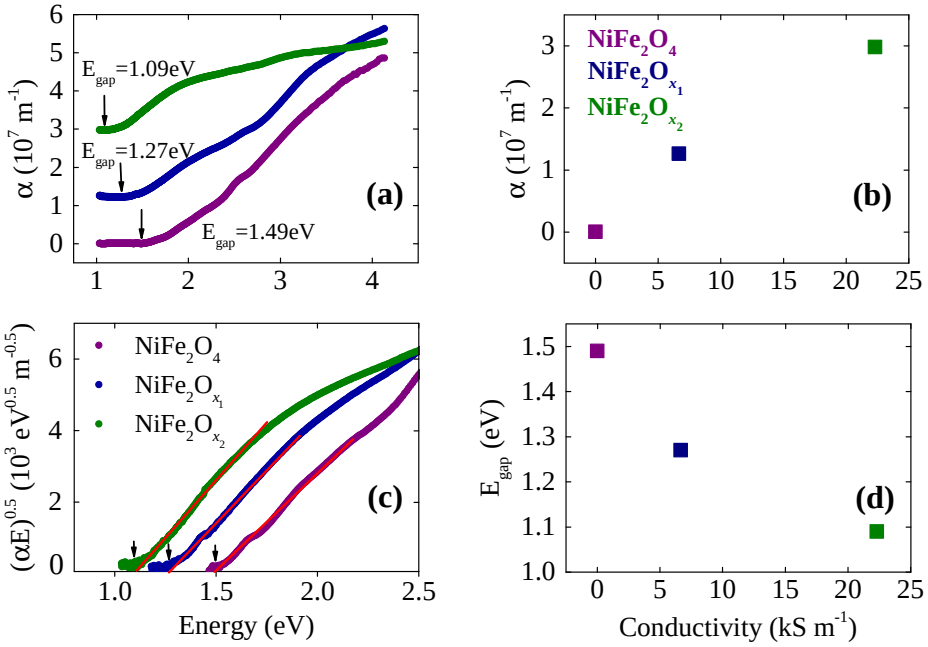

Figure 4.6. (a) The RT optical absorption spectrum for NFO, $NiFe_2O_{x_1}$, and $NiFe_2O_{x_2}$. (b) The absorption saturation value at 1 eV versus the RT conductivity. (c) Tauc plot $(\alpha E)^{0.5}$ versus energy for the determination of the minimum gap for all samples. The black arrows indicate the minimum direct gaps. (d) The band gap energy versus the RT conductivity.

To investigate the optical properties of the films, the energy-dependent absorption coefficient α(E) was extracted from the measured transmission T and reflection R spectra using

$$\alpha = \frac{1}{d} \ln \frac{1-R}{T}, \tag{4.12}$$

where d was equal to 160, 60, and 35 nm corresponding to the thickness for the NFO, $NiFe_2O_{x_1}$, and $NiFe_2O_{x_2}$ samples, respectively. Figure 4.6(a) illustrates the absorption coefficient as a function of the energy for all samples. It is worth noting that down to a lower energy limit, a saturation plateau is visible in all cases. The plateau region indicates that the energy of the photons is lower than the band gap of the sample and, therefore, insufficient to excite electrons

from the valence band to the conduction band. Nevertheless, it is clearly observed that there is a different finite absorption value for each sample. Interestingly, as visible in Fig. 4.6(b) where the absorption saturation value is plotted against the conductivity of the samples, for the NFO the absorption saturation value is zero in this plateau unveiling that the additional electronic states in the band gap are too few to noticeably contribute to the measured absorbance. On the other hand, for the $NiFe_2O_{x_1}$ and $NiFe_2O_{x_2}$ samples the absorption saturation value is equal to $1.26 \times 10^7\,m^{-1}$ and $2.99 \times 10^7\,m^{-1}$, respectively, confirming that the number of electronic states in the band gap contributing to the measured absorption is larger in the more conducting samples. The absorption spectrum of the NFO is very similar to previous investigations, [152, 165] as well as to the epitaxial NFO from Holinsworth *et al*. [188].

A common way to determine the minimum gap from the optical absorption spectra is by evaluating Tauc plots as explained in Ref. [152]. The indirect gap can be extracted from straight line segments in $(\alpha E)^{0.5}$ plotted over energy. In Fig. 4.6(c) the minimum gaps are extracted for each sample. It is worth mentioning that in order to extract the band gap energies, the curves are shifted such that the plateau regions are at zero absorption. For the NFO, the optical band gap is estimated to be $E_{gap}^{NFO} \approx 1.49\,eV$, close to previous publications [165, 189]. The optical band gap for the $NiFe_2O_{x_1}$ and $NiFe_2O_{x_2}$ samples is $E_{gap}^{NiFe_2O_{x_1}} \approx 1.27\,eV$ and $E_{gap}^{NiFe_2O_{x_2}} \approx 1.09\,eV$, respectively, unveiling the more conducting character of the latter. The band gap energy of all samples is presented in Fig. 4.6(d) as a function of the RT electrical conductivity. However, the determination of the band gap using Tauc plots could lead to rough estimated values because of the uncertainties that may come up during this kind of data processing [152].

It is clear that the band gap energy increases with the decrease of conductivity. In addition, the extracted optical band gap is considerably larger than the corresponding thermal activation energy estimated from the temperature dependent resistivity measurements, in all cases. The reason for that is focused on the nature of the experimental techniques which were used to determine the corresponding optical and electrical band gaps. The temperature dependent resistivity is sensitive to all charge transport mechanisms which characterize the film, for example chemical impurities, defects etc.,

that influence the measured resistivity, compared to the optical absorption. More specifically, the optical band gaps determined from optical absorption measurements are of the order of some eV, indicating the energy that is needed for a carrier located in the valence band to get excited to the conduction band. On the other hand, the electrical band gaps stemmed from the resistivity measurements are of the order of some meV, reflecting the thermal activation energy which is necessary for a carrier located in an impurity level to get excited to the conduction band.

Chapter 5

LSSE in NM/FM bilayers

This chapter addresses results on the LSSE on different NM/FM bilayer systems, ranging from FMIs (YIG) to FMMs ($Co_{1-x}Fe_x$ and $Ni_{1-x}Fe_x$) with intermediate FM semiconductor-like ($NiFe_2O_x$). In the first part we will point out the necessity to utilize the physical quantity of heat flux instead of the commonly used temperature gradient, taking into account the interfacial thermal resistances in LSSE experiments. Next, we will present the LSSE measurements on a Pt/YIG bilayer. These results were gained in close collaboration with Dr. Alessandro Sola from Istituto Nazionale di Ricerca Metrologica (INRIM), Italy and have been published in Ref. [29].

Besides the pure LSSE voltage while examining Pt/FMI bilayers with no proximity-induced polarization, the observations can be quite different when studying NM/FM-semiconductors and NM/FMM bilayers. In such cases, additional parasitic effects (e.g. FM-induced and proximity-induced ANE) may appear and enhance the measured LSSE voltage, preventing from its correct interpretation. Motivated by the necessity to quantitatively disentangle the LSSE voltage from the side effects in NM/FM thin films, we present and analyze a compact procedure for the quantitative disentanglement of the LSSE from both ANE contributions, which established the starting point to experimentally identify the proximity-induced ANE in metals. In the last part, the focus lies on the demonstration of the disentangled effects on

Pt/$NiFe_2O_x$, Pt/$Co_{1-x}Fe_x$, and Pt/$Ni_{1-x}Fe_x$ bilayers and their correlations to the magnetic, electrical, and optical properties of the films. All of the obtained results have been published in Ref. [190] or are under preparation for publication [191]. All sections depend on the corresponding articles.

5.1 Heat flux vs. temperature gradient methods

One of the striking contributions in the field of spin caloritronics is the SSE which stands for the electromotive force generated perpendicular to the heat current in a NM, being in touch with a FM under the application of a temperature bias, as thoroughly described in the theoretical part of this thesis. A variety of experimental setups and methods have been reported in literature for the generation and determination of a temperature gradient $\boldsymbol{\nabla} T$, as the driving force for LSSE measurements. These are Joule heating in an external heater [98, 143] or via induced charge current in the sample [192], using needles [27, 31], using rotatable temperature gradients [193, 194], Peltier heating [114], on-chip heating [195, 196], and laser heating [197]. However, it is undeniable that the LSSE coefficient must be independent from the experimental setup or measurement method and acquire reproducible values depending only on the material and the device geometry.

The SSE coefficient is defined as $S_{\mathrm{SSE}} = -E/\nabla T$. $E = V/L_{\mathrm{V}}$ is the electric field strength generated by the ISHE in the heavy metal [see Eq. (2.6)] and estimated by the measured SSE voltage V and the distance between the electrical contacts, L_{V}. The thermal gradient $\nabla T = \Delta T/L_{\mathrm{T}}$ is estimated by the temperature difference between the two surfaces of the sample ΔT and the total length of the sample in the direction of the temperature gradient, L_{T}.

The most used method for the determination of the SSE coefficient includes the measurement of the temperature difference between two thermal baths being in contact with the sample, as depicted in Fig. 5.1(a). This method requires the knowledge of the thicknesses and the thermal conductivities of all layers of the sample. A common approach is to consider a linear gradient assuming similar temperature drop for all layers, as denoted by the blue line in Fig. 5.1(a). However, this assumption neglects the thermal resistance between the sample and the thermal baths as well as the interfacial thermal

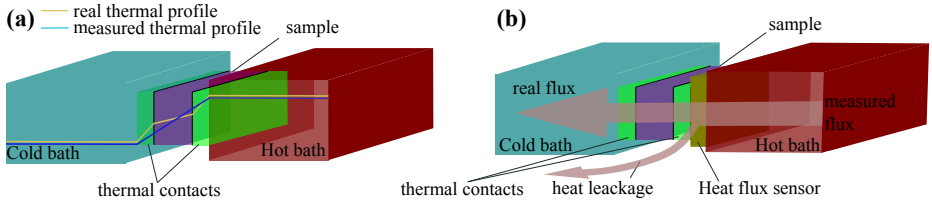

Figure 5.1. (a) Schematic illustration of the direct temperature measurement. The blue line corresponds to the assumed linear temperature profile between the two heat baths. The yellow line shows the real temperature profile considering the thermal resistances at the interfaces. (b) Schematic illustration of the heat flux measurement. The real quantity of the heat flux flowing into the sample (big arrow) depends on the amount of the heat leakage (small arrow).

resistances, leading to the misinterpretation of the temperature difference. The temperature profile considering the thermal resistances between the contacts in the setup is qualitatively presented in Fig. 5.1(a) by the yellow line.

As a consequence, in order to overcome this challenging frontier a universal method should be proposed allowing for the elimination of the systematic errors due to the thermal interface resistances and thermal contacts. This method considers the heat flux which passes through the cross section of the sample, as suggested by Sola *et al.* [29, 166]. This approach results in the effective comparison not only between LSSE measurements of different setups but also between different measurement configurations within the same setup, as it is explained later on in this thesis. The heat flux method employs Peltier elements as heat flux sensors, as shown in Fig. 5.1(b) and explained in Sec. 3.6. The heat Q which passes through every layer of the sample is calculated from

$$Q = \frac{\Delta T}{L_{\mathrm{T}}} K \cdot S, \tag{5.1}$$

where S is the side area perpendicular to the direction of the heat propagation and K is the thermal conductivity of the corresponding layer. Then the heat flux ϕ_{q} is determined by

$$\phi_{\mathrm{q}} = \frac{K\,\Delta T}{L_{\mathrm{T}}}. \tag{5.2}$$

In turn, the S_{SSE} is calculated by $S_{\mathrm{SSE}} = \left(\frac{V}{L_{\mathrm{V}}}\right)/\phi_{\mathrm{q}}$. The heat flux method can be considered equivalent to the ΔT method if the thermal conductivity $K = \left(\frac{Q}{S}\right)/\left(\frac{\Delta T}{L_{\mathrm{T}}}\right)$ of the magnetic material is known and, thus, the S_{SSE} is calculated by $S_{\mathrm{SSE}} = \left(\frac{V}{L_{\mathrm{V}}}\right)\Big/\left(\frac{\Delta T}{L_{\mathrm{T}}}\right) = -E/\nabla T$. The measured heat flux can be misinterpreted, as described in the sketch of Fig. 5.1(b) (small arrow), if there are uncontrolled heat leakages. To eliminate this undesirable condition, the system was kept under vacuum.

5.2 LSSE in Pt/YIG bilayer

The S_{SSE} was measured with the two aforementioned methods in two different setups at INRIM and Bielefeld University. First, we performed a comparison between the two ΔT-based measurement setups and then both setups were modified for the measurement using the heat flux method [29]. We investigated the reproducibility of our results and emphasized on the advantageous use of the heat flux method. We used a Pt(3 nm)/YIG(60 nm) sample grown on Yttrium Aluminum Garnet substrate. Since YIG is an insulator and according to a previous report [131] which neglect the proximity induced magnetization from YIG to the adjacent NM, we can assume no FM- and proximity-induced ANE contributions to the LSSE signal. At the edges of the sample's top surface we sputtered two 100 nm thick gold electrode strips, allowing for the same Ohmic contact between the Pt film and the electrical connections used in the two setups. We further spin-coated the Pt surface of the sample with PMMA as a protection layer, eliminating the deterioration of the Pt film due to the continuous measurements. This preparation step enhanced the contact thermal resistance and added a constant value of temperature drop to the measurement in the ΔT method configuration without, however, affecting the measurement of the heat flux, since the heat flux method is independent from the thermal contact resistances.

The LSSE measurements performed in the two laboratories with both the ΔT and the heat flux methods are reported in Fig. 5.2. We applied an out-of-plane thermal gradient in the presence of an in-plane magnetic field with strength equal to $H = 20\,\mathrm{mT}$. The voltage was collected transverse to the direction of the external applied magnetic field and the electric field was calculated from the measured voltage and the distance between the two

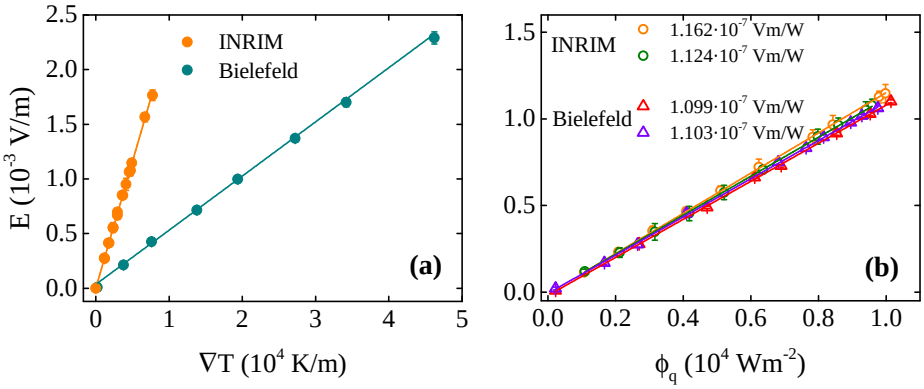

Figure 5.2. LSSE driven electric field from both laboratories at Bielefeld University and INRIM as a function of (a) the obtained thermal gradient and (b) the measured heat flux.

contacts L_V. The error bars in the y axis include the uncertainty on both the measurement of L_V and V. The amplitudes of the error bars on the x axis are too small to be resolved in the Figure. For the accurate comparison of the results from the heat flux method with those from the ΔT method reported in Fig. 5.2(b), it is necessary to assume the thermal conductivity of the YIG equal to $K_{YIG} = 6\,\mathrm{Wm^{-1}K^{-1}}$ [198], as explained in prior. As depicted in Fig. 5.2(a), there is a prominent difference by a factor of 4.6 between the values of the S_{SSE} obtained in the two laboratories with the ΔT method. Consequently, the results verify that the temperature profile drawn in Fig. 5.1(a) (blue line) is not the existent one, dictating that the thermal contacts resistance leads to a substantial temperature drop. As a result, ΔT is highly misinterpreted. A reliable estimation of the real temperature difference across the sample necessitates the thermal contacts resistance to be negligible with respect to the one of the sample [29].

Considering the heat flux method, the spin Seebeck coefficients are found to be equal to $S_{SSE} = (6.620 \pm 0.044) \cdot 10^{-7}\,\mathrm{V/K}$ and $S_{SSE} = (6.851 \pm 0.038) \cdot 10^{-7}\,\mathrm{V/K}$ for the Bielefeld and INRIM groups, respectively. The extracted S_{SSE} values imply that the uncertainty between two sets of measurements from the same setup is of the same order as the uncertainty between two measurement sets from the two different setups. The results unveil that the systematic errors related to heat leakage from the thermal circuit can be considered as

very small and highlight the possibility to eliminate the systematic error due to thermal resistances. Therefore, a reproducible and with low uncertainty measurement of the spin Seebeck coefficient requires an approach based on the heat flux method.

5.3 Quantitative disentanglement of SSE, proximity-induced, and FM-induced ANE in NM/FM bilayers

When studying NM/FMI systems, a spin current which is generated parallel to a temperature gradient, it is generally attributed to the LSSE. However, in case of studying FMMs or semiconducting-FMs, not only a proximity-induced ANE [16] can overwhelm the LSSE signal, but also an additional ANE contribution could be present as well [30, 143], arising from the FM. Mainly NM/FMI bilayers have been investigated, while LSSE studies on NM/FMM are quite rare. Holanda *et al*. [40] reported on this topic the observation of the LSSE signal separated from the ANE contribution in permalloy (Py) by using Py/NiO/Pt trilayer samples. Additionally, Ramos *et al*. [30, 32, 34, 39] and Wu *et al*. [33] individually investigated the LSSE in magnetite, which is conducting at RT and, thus, has an ANE contribution induced from the FM. They identified the LSSE in Pt/Fe_3O_4 [30] and CoFeB/Fe_3O_4 bilayers [33] by using temperatures below the conductor-insulator transition of magnetite (Verwey transition at 120 K) in order to exclude any FM-induced ANE contribution. Ramos *et al*. further investigated the ANE in bulk magnetite without any Pt [32] and concluded that the ANE contributions for Pt/Fe_3O_4 bilayers and multilayers should be quite small [34, 39]. In addition, Lee *et al*. [36] and Uchida *et al*. [35, 38] discussed that in Pt/FMM multilayers both LSSE and ANE contribute, but did not disentangle the effects quantitatively. Hence, a clear quantitative disentanglement of the LSSE in the FMM, the ANE in the FMM, and the proximity-induced ANE in the NM is still pending.

Some groups used Cu or Au interlayers to suppress the MPE in NM/FMM bilayers [17, 20, 21], however, a promising technique to distinguish between LSSE and proximity-induced ANE was first proposed by Kikkawa *et al*. [17, 18]. In their study, the voltage measured transverse to the thermal gradient in IPM and OPM configurations, leads to the sufficient separation of the

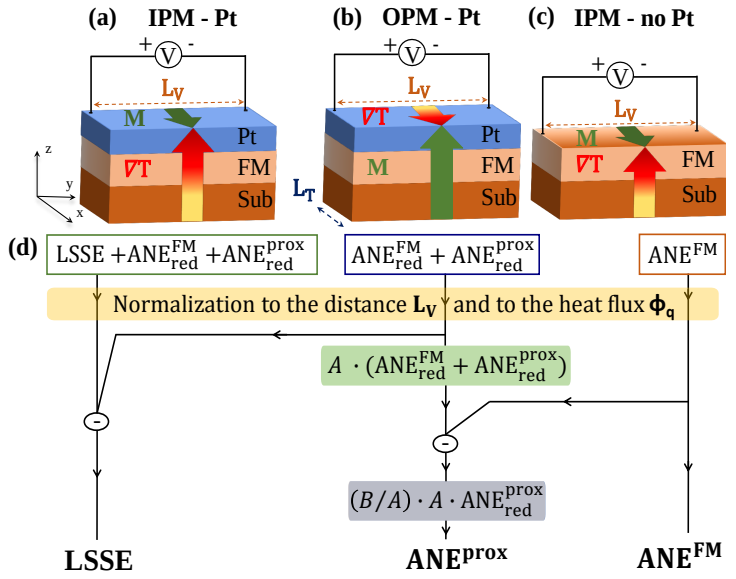

Figure 5.3. Schematic illustration of (a),(c) in-plane magnetized and (b) out-of-plane magnetized geometries, introducing the temperature gradient ∇T, the magnetization vector $\boldsymbol{M}$, the distance between the contacts L_V and the total length of the sample L_T, respectively. (d) Flow chart for the quantitative separation of both ANE contributions from the LSSE voltage. The light green and grey areas correspond to the intermediate steps determining the correction factors A and B respectively, taking into account the reduction of the ANE signal due to the additional Pt layer (spin-polarized and/or non-magnetic).

aforestated contributions. So far, this technique was only used to study the proximity-induced ANE in NM/FMI bilayers. It has not yet been applied to fully conducting NM/FMM bilayers for the separation of the LSSE and ANE contributions in the FMM. In our work, we extended this technique to identify all three contributions quantitatively: LSSE, ANE in the FM, and proximity-induced ANE.

Figures 5.3(a)-(c) illustrate the measurement geometries that we have employed for the separation of the three effects. In the IPM geometries [Figs. 5.3(a) and 5.3(c)] the application of an out-of-plane temperature gradient ∇T in the presence of an in-plane magnetic field along the x axis induces a transverse voltage along the y axis. While measuring in this IPM configuration using the FMs with Pt on top [IPM-Pt, Fig. 5.3(a)], we detect the LSSE

voltage together with both ANE contributions, i.e., FM-induced and proximity-induced. However, in the IPM geometry without Pt [IPM - no Pt, Fig. 5.3(c)] we are only sensitive to the ANE contribution from the FM.

In the OPM geometry utilizing FMs with Pt on top [OPM - Pt, Fig. 5.3(b)], the application of an in-plane temperature gradient $\boldsymbol{\nabla} T$ together with an out-of-plane magnetic field, generates a transverse voltage attributed to the FM-induced and proximity-induced ANE. In this configuration, the LSSE cannot be detected, since no out-of-plane spin current with the proper spin polarization direction is generated [17]. One major issue is to consider the reduction of the ANE signal upon a placement of a Pt layer [30]. All ANE contributions measured with Pt on top have in general reduced contributions and this is indicated by the subscript "red" in Fig. 5.3 and throughout the thesis.

Figure 5.3(d) explains the flow chart for the quantitative disentanglement of the three effects. As a first step, the electric field is calculated from the measured voltages by normalizing to the distance of the electric contacts L_{V}. Then, this electric field is divided by the heat flux ϕ_{q} that runs through the sample. To estimate the ANE reduction due to the additional Pt layer we used the ratio of conductances G of the FM and the Pt in a parallel arrangement [30]

$$r = \frac{G_{\mathrm{FM}}}{G_{\mathrm{Pt}}} = \frac{\rho_{\mathrm{Pt}}}{\rho_{\mathrm{FM}}} \frac{t_{\mathrm{FM}}}{t_{\mathrm{Pt}}}, \tag{5.3}$$

with ρ: RT resistivity and t: thickness of the corresponding layer. The reduced ANE signal from the FM ($\mathrm{ANE}^{\mathrm{FM}}_{\mathrm{red}}$) in the OPM - Pt configuration is then corrected by the factor $A = \frac{r+1}{r}$ [30], resulting in the pure $\mathrm{ANE}^{\mathrm{FM}} = A \cdot \mathrm{ANE}^{\mathrm{FM}}_{\mathrm{red}}$. This correction step in our calculations is highlighted by the light green area in Fig. 5.3(d). Combined with the information on the $\mathrm{ANE}^{\mathrm{FM}}$ from the IPM - no Pt configuration [cf. Fig. 5.3(c)], i.e., by subtracting the $\mathrm{ANE}^{\mathrm{FM}}$ from the corrected term, this method already yields a qualitative criterion for the existence or absence of proximity-induced ANE in the sample.

For a quantitative evaluation, an additional correction has to be applied to the reduced proximity-induced ANE signal ($\mathrm{ANE}^{\mathrm{prox}}_{\mathrm{red}}$) due to the additional non-magnetic Pt layer, while the correction A on the term has to be reversed [see light grey area in Fig. 5.3(d)]. The correction factor for the $\mathrm{ANE}^{\mathrm{prox}}_{\mathrm{red}}$ is given by $B = \frac{d_{\mathrm{I}}+d_{\mathrm{II}}}{d_{\mathrm{I}}}$ [30], where d_{I} and d_{II} are the thicknesses of the spin-

polarized Pt layer and the non-magnetic fraction, respectively, estimated by XRMR. Then, the corrected proximity-induced ANE contribution is denoted as $ANE^{prox} = (B/A) \cdot A \cdot ANE^{prox}_{red}$. For the determination of the correction factor A, the same resistivity ρ_{Pt} was used for the polarized and unpolarized fraction of the Pt layers.

Consequently, the comparison between the voltage signals in the IPM and OPM geometries enables a quantitative separation of the ANE contributions from the LSSE signal. Interestingly, this technique also offers the possibility to systematically investigate the dependence of the individual transport effects on other properties of the materials, e.g., thicknesses and roughnesses.

5.4 LSSE in Pt/$NiFe_2O_x$ bilayers

We employed the aforementioned separation technique for the quantitative disentanglement of the LSSE from the ANE contributions in Pt, on different FM materials such as nearly-insulating $NiFe_2O_4$, semiconducting-like $NiFe_2O_x$ ($4 > x > 0$), and metallic $Ni_{33}Fe_{67}$. According to the previously analyzed flow chart [see Fig. 5.3(d)], this compact procedure necessitates the preparation of twin samples (with and without Pt on top), the implementation of different measurement geometries, the normalization to the heat flux instead of the thermal gradient, and the determination of significant correction factors A and B for the quantitative analysis, to quantitatively separate the effects.

Figure 5.4 illustrates the experimental results for the Pt/$NiFe_2O_{x_2}$ and Pt/$Ni_{33}Fe_{67}$ bilayers. The acquired voltage is normalized to the contact distance and to the heat flux (V_{norm}). The chosen heat flux values for the normalization are comparable in all samples but not identical. However, the magnitude of the normalized signal will not be influenced by the choice of the heat flux value, due to the linear interdependency between both the voltage and the heat flux. By comparing the difference between the ANE^{FM} from the IPM - no Pt configuration (orange line) and the $ANE^{FM} + ANE^{prox}$ signals (corrected $ANE^{FM}_{red} + ANE^{prox}_{red}$ by A and B, as explained above, purple line) we are able to quantitatively determine the contribution from the proximity-induced ANE. For the non-metallic $NiFe_2O_{x_2}$ bilayer [Fig. 5.4(a) and 5.4(b)], no difference can be determined between the saturation values of the ANE^{FM} data from IPM - no Pt configuration [orange line in Fig. 5.4(a)] and the saturation

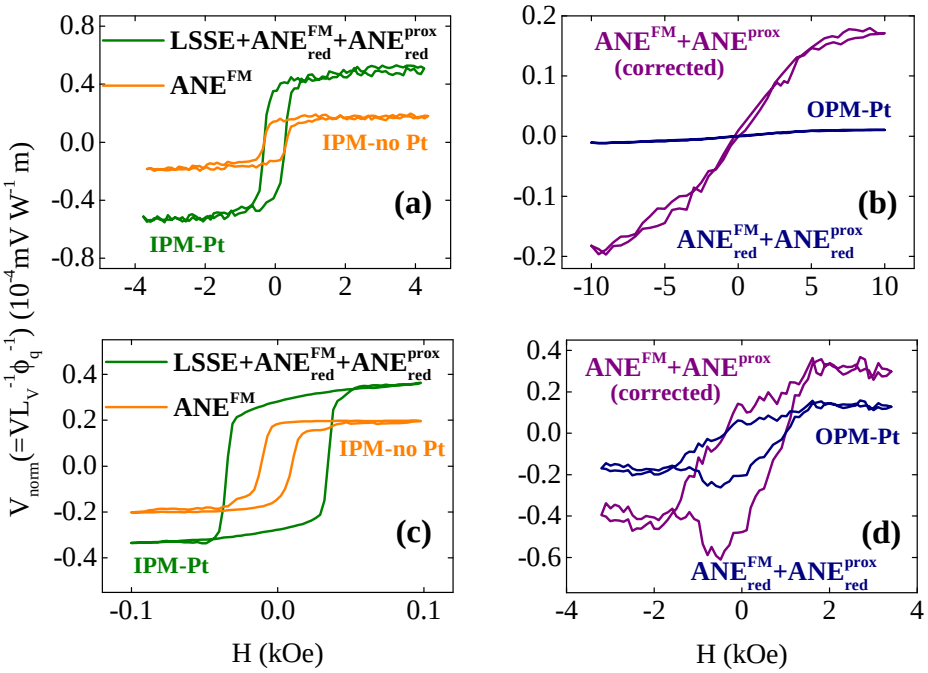

Figure 5.4. Normalized voltage plotted against the magnetic field strength for (a), (b) Pt/$NiFe_2O_{x_2}$ and (c), (d) Pt/$Ni_{33}Fe_{67}$ bilayers, measured in (a), (c) IPM and (b), (d) OPM geometries with the corresponding separation of the ANE contribution (FM-induced and proximity-induced) from the LSSE voltage. ANE^{FM} + ANE^{prox} (purple) regards the calculated ANE signal after the implementation of the correction factors *A* and *B*, which correct the reduction of the measured ANE from the OPM - Pt configuration due to the additional Pt layer (spin-polarized and/or non-magnetic).

values of the ANE^{FM} + ANE^{prox} signal [corrected OPM - Pt data, purple line in Fig. 5.4(b)], which are extracted to be $V^{sat}_{norm} = (0.18 \pm 0.02)\,10^{-4}$mVW^{-1}m in both cases. Thus, the ANE^{prox} is zero and can be neglected for this sample. We conclude that the LSSE appears to be the prominent contribution to the total signal [cf. (Fig. 5.4(a) green line]. On the contrary, for the Pt/$Ni_{33}Fe_{67}$ bilayer [Fig. 5.4(c) and 5.4(d)] the ANE^{FM} + ANE^{prox} is (46 ± 3)% larger than the ANE^{FM} signal unveiling the existence of MPE. Furthermore, for the Pt/NFO bilayer both ANE^{FM} and ANE^{FM} + ANE^{prox} signals are zero confirming the absence of any ANE contribution [37, 132].

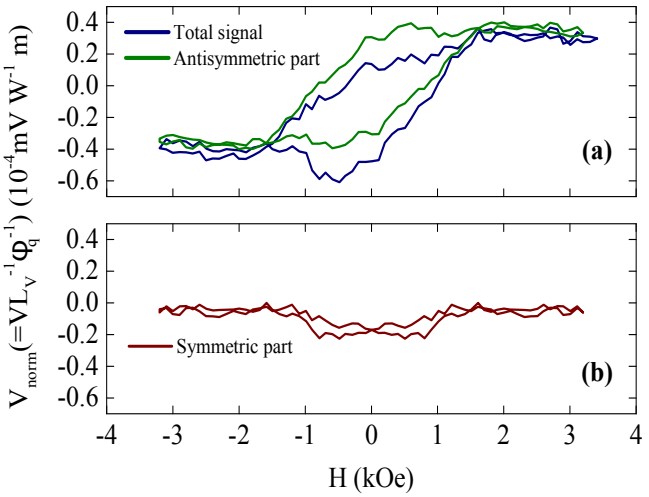

Figure 5.5. (a) Total ANE^{FM} + ANE^{prox} signal and antisymmetric contribution of it for the $Pt/Ni_{33}Fe_{67}$ bilayer. (b) The symmetric contribution to the total signal.

It is worth noting that since in the OPM configuration the application of an in-plane thermal gradient is combined with the application of an out-of-plane magnetic field, an unintended misalignment of the field direction (possible in-plane components) could induce parasitic contributions hampering the measured signal. One possible contribution could be the TSSE which is controversially discussed. So far, in earlier investigations no evidence for the existence of a TSSE could be proven and, therefore, we neglect such a parasitic signal in our measurements [27, 31, 107–109, 113].

Moreover, apart from the TSSE an additional PNE contribution could contaminate the measured voltage prohibiting from the correct interpretation of the desired signal. This contribution is indeed observable while measuring on the $Pt/Ni_{33}Fe_{67}$ sample and appears in the deep of the curve in Fig. 5.4(d). However, the PNE is symmetric with the field and we can easily separate this contribution from the antisymmetric ANE signal. In Fig. 5.5(a) the total signal is presented together with the extracted antisymmetric contribution from the ANE. In Fig. 5.5(b) the symmetric contribution is illustrated which is considerably smaller than the antisymmetric one. In addition, since we are interested in the difference of voltages between plus and minus magnetic field saturation, the symmetric signal does not contribute to the measured voltage and the

values extracted from the antisymmetric signal are the same as if we calculate the magnitude of the effect from the total one. Therefore, we conclude that although a PNE contribution is visible in our measurements, it doesn't affect the magnitude of the effect allowing for the correct interpretation of the measured voltage.

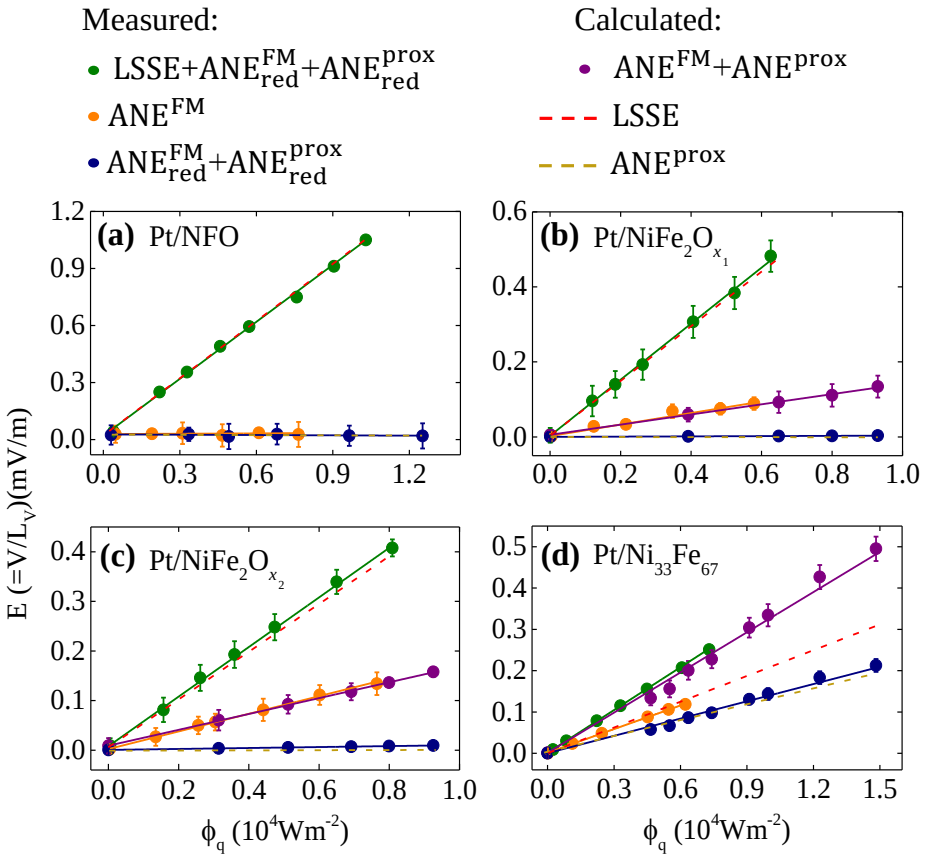

Figure 5.6. Electric field against the heat flux for (a) Pt/NFO, (b) Pt/NiFe$_2$O$_{x_1}$, (c) Pt/NiFe$_2$O$_{x_2}$, and (d) Pt/Ni$_{33}$Fe$_{67}$ samples with the corresponding separation of the ANE contribution (FM-induced and proximity-induced) from the LSSE voltage.

Figure 5.6 illustrates the linear dependence of the electric field (voltage in saturation normalized to the electric contacts distance L_V) on ϕ_q, for all samples. The dashed lines are the calculated contributions of the pure LSSE and ANE^{prox}, extracted as described in the diagram of Fig. 5.3(d) after

correcting the reduced ANE signal arising from both the FM and the spin-polarized Pt layer. In Fig. 5.6(a), the zero line contribution of both types of ANE indicates the absence of MPE in Pt/NFO bilayers [37, 132]. The low amount of mobile charge carriers in the nearly-insulating NFO leads to a vanishing ANE^{FM} contribution [143].

As shown in Figs. 5.6(a)–5.6(c), the LSSE contribution is dominant for all $Pt/NiFe_2O_x$ ($x > 0$) bilayers that consist of oxides. Furthermore, the absence of any proximity-induced ANE is verified, since no difference between the ANE^{FM} and the $ANE^{FM} + ANE^{prox}$ can be identified. Additionally, for the $Pt/NiFe_2O_{x_2}$ bilayer the ANE^{FM} contribution is 14% larger than for the $Pt/NiFe_2O_{x_1}$ bilayer pointing towards its more conducting character. For the $Pt/Ni_{33}Fe_{67}$ bilayer [Fig. 5.6(d)], the enhancement of $ANE^{FM} + ANE^{prox}$ due to the metallic character of $Ni_{33}Fe_{67}$ and the MPE contribution is clearly displayed. Moreover, the ANE^{FM} and the LSSE signals are of comparable magnitude for this sample. The concluded absence of proximity-induced ANE contribution in Pt/NFO, $Pt/NiFe_2O_{x_1/x_2}$ samples and the presence of this contribution in the metallic $Pt/Ni_{33}Fe_{67}$ bilayer, is in line with the XRMR results and are analyzed in Sec. 6.1.

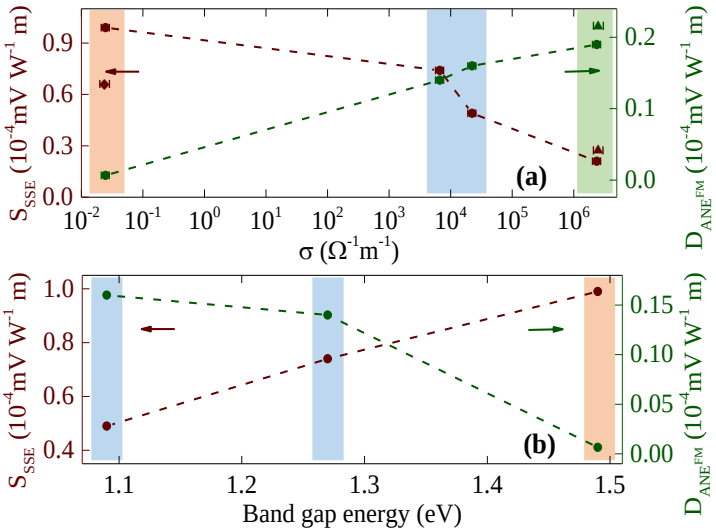

Figure 5.7. SSE and ANE^{FM} coefficients as a function of (a) the electrical conductivity σ for $NiFe_2O_{x_1/x_2}$ (blue area), NFO (orange area), and $Ni_{33}Fe_{67}$ (green area) samples and (b) the optical band gap for $NiFe_2O_{x_1/x_2}$ and NFO samples.

Figure 5.7(a) shows the SSE ($S_{\mathrm{SSE}} = \frac{E_{\mathrm{SSE}}}{\phi_{\mathrm{q}}}$) and ANE$^{\mathrm{FM}}$ ($D_{\mathrm{ANE}}^{\mathrm{FM}} = \frac{E_{\mathrm{ANE}}^{\mathrm{FM}}}{\phi_{\mathrm{q}}}$) coefficients extracted from the corresponding slopes of the curves in Fig. 5.6, plotted against the RT value for the measured electrical conductivity. There is a pronounced increase of the $D_{\mathrm{ANE}}^{\mathrm{FM}}$ when the conductivity increases, whereas the S_{SSE} decreases. A challenging issue is the thickness dependency of the obtained SSE and ANE$^{\mathrm{FM}}$ coefficients. In order to further elucidate this issue we disentangled the effects and extracted the corresponding SSE and ANE$^{\mathrm{FM}}$ coefficients for an additional Pt/NFO and Pt/$Ni_{33}Fe_{67}$ sample, with nominal FM thicknesses equal to t_{NFO}=22 nm and $t_{\mathrm{Ni_{33}Fe_{67}}}$=160 nm, respectively. For both samples t_{Pt}=3 nm. The results are also indicated in Fig. 5.7(a) using a rhombus for the Pt/NFO and a triangle for the Pt/$Ni_{33}Fe_{67}$ bilayers, respectively. The S_{SSE} of the additional Pt/NFO sample is smaller than the initial one illustrating a weak thickness dependency. However, the main trend of decreasing S_{SSE} with increasing conductivity still holds. Moreover, considering the additional the Pt/$Ni_{33}Fe_{67}$ bilayer a weaker thickness dependency of both coefficients can be extracted. Consequently, the $D_{\mathrm{ANE}}^{\mathrm{FM}}$ clearly increases with increasing conductivity whereas the S_{SSE} decreases. These results, are a first step towards the study of the thickness dependency of SSE and ANE$^{\mathrm{FM}}$ coefficients in such systems and further investigation should be conducted to clarify this issue.

Figure 5.7(b) depicts the dependence of the SSE and ANE$^{\mathrm{FM}}$ coefficients on the optical band gap for the NFO and $NiFe_2O_{x_1/x_2}$ bilayers. The description of the band gap determination can be found in Sec. 4.5. It is clearly observed that the more conducting samples are characterized by lower band gap energies, reflecting the existence of additional electronic states in the band gap. Additionally, the $D_{\mathrm{ANE}}^{\mathrm{FM}}$ increases for decreasing band gap energy verifying the previous assumption of more mobile charge carriers at a reduced oxygen concentration. On the contrary, the S_{SSE} increases for larger band gap energies.

In the Table 5.1 the measured physical parameters of all samples are presented, where t_{FM}: thickness of the FM, t_{Pt}: thickness of the Pt layer, $t_{\mathrm{Pt}}^{\mathrm{NM}}$: thickness of the non-magnetic fraction of Pt, $t_{\mathrm{Pt}}^{\mathrm{SP}}$: thickness of the spin-polarized fraction of Pt, ρ_{FM}: electrical resistivity of the FM (measured on the samples without Pt on top), ρ_{Pt}: electrical resistivity of Pt, and R: resistance between the voltage contacts, for each film respectively. The ρ_{Pt} values were calculated

Table 5.1. Resistivity at room temperature, thickness, and resistance between the voltage contacts for Pt/NFO, Pt/$NiFe_2O_{x_1}$, Pt/$NiFe_2O_{x_2}$, and Pt/$Ni_{33}Fe_{67}$ samples.

Film	Pt/NFO	Pt/$NiFe_2O_{x_1}$	Pt/$NiFe_2O_{x_2}$	Pt/$Ni_{33}Fe_{67}$
t_{FM} (nm)	160	60	35	10.4
t_{Pt} (nm)	3.0	2.7	3.1	3.5
t_{Pt}^{NM} (nm)	3.0	2.7	3.1	2.5
t_{Pt}^{SP} (nm)	0.0	0.0	0.0	1.0
ρ_{FM} (Ωm)	40.5	$1.5 \cdot 10^{-4}$	$4.5 \cdot 10^{-5}$	$4.2 \cdot 10^{-7}$
ρ_{Pt} (Ωm)	$1.6 \cdot 10^{-7}$	$1.7 \cdot 10^{-7}$	$1.8 \cdot 10^{-7}$	$1.6 \cdot 10^{-7}$
R_{FM} (Ω)	$3.4 \cdot 10^{9}$	$3.3 \cdot 10^{4}$	$1.7 \cdot 10^{4}$	$0.5 \cdot 10^{3}$

from the measured ρ values of the twin samples with and without the Pt layer on top.

As additional information the Seebeck coefficients for the $NiFe_2O_{x_1}$, $NiFe_2O_{x_2}$, and $Ni_{33}Fe_{67}$ are found to be equal to: 57.2 μV/K, 28.2 μV/K, and 18.2 μV/K, correspondingly. The Seebeck coefficients are estimated after the subtraction of the contribution from the gold wires used for the electrical contacts [193]. Moreover, the D_{ANE}^{FM} for $NiFe_2O_{x_1}$, $NiFe_2O_{x_2}$, and $Ni_{33}Fe_{67}$ is also calculated in units V/K and found to be equal to: 2.8 nV/K, 3.8 nV/K, and 4.7 nV/K, respectively. The D_{ANE}^{FM} for the metallic sample is consistent with values found for permalloy in an earlier publication [40].

5.5 LSSE in Pt/$Co_{1-x}Fe_x$ and Pt/$Ni_{1-x}Fe_x$ bilayers

As a next step, we applied our previously mentioned compact procedure to tackle the issue of the full separation of the effects in FMMs with an adjacent spin-polarized Pt layer. We investigated Pt/$Co_{1-x}Fe_x$ and Pt/$Ni_{1-x}Fe_x$ bilayers focusing on the correlation of the extracted transport coefficients to the compositions and the magnetic moment of both the FMM and the spin-polarized Pt layer. The significant proximity-induced ANE contribution reported here and its dependence on the FMM and spin-polarized Pt layer magnetic moments, unveils that MPE is a key element of spintronics and

could modulate and emerge the functionality of future spintronic and spin caloritronic devices.

Table 5.2 summarizes the measured physical parameters of all samples. For the Pt/$Co_{1-x}Fe_x$ series the FMM and Pt thicknesses are taken from the XRMR analysis as presented in Sec. 6.2 whereas for the Pt/$Ni_{1-x}Fe_x$ the thicknesses are obtained via XRR measurements. As previously, the ρ_{Pt} values were calculated from the measured ρ values of the twin samples with and without the Pt layer on top of the FMM.

Table 5.2. Thickness of the FMM (t_{FMM}), total Pt (t_{Pt}), non-magnetic Pt (t_{Pt}^{NM}), spin-polarized Pt (t_{Pt}^{SP}) layers. RT resistivity of the FMM (ρ_{FMM}), Pt (ρ_{Pt}) layers, and the Pt magnetic moment extracted from the XRMR measurements (see Sec. 6.2), for all samples, respectively. For the Pt/$Ni_{1-x}Fe_x$ bilayers the magnetic moments are taken from Refs. [132, 161].

Film	t_{FMM} (nm)	t_{Pt} (nm)	t_{Pt}^{NM} (nm)	t_{Pt}^{SP} (nm)	ρ_{FMM} (Ωm)	ρ_{Pt} (Ωm)	Pt moment (μ_B/Pt atom)
Pt/Fe	10.0	3.0	2.0	1.0	$3.30\cdot10^{-7}$	$8.10\cdot10^{-8}$	0.60 ± 0.10
Pt/$Co_{33}Fe_{67}$	9.6	3.2	2.0	1.2	$6.11\cdot10^{-7}$	$8.05\cdot10^{-8}$	0.72 ± 0.03
Pt/$Co_{50}Fe_{50}$	8.2	3.1	1.9	1.2	$4.31\cdot10^{-7}$	$8.01\cdot10^{-8}$	0.71 ± 0.03
Pt/$Co_{70}Fe_{30}$	9.9	3.0	1.8	1.2	$4.50\cdot10^{-7}$	$8.11\cdot10^{-8}$	0.66 ± 0.03
Pt/$Co_{85}Fe_{15}$	10.0	3.0	1.8	1.2	$4.73\cdot10^{-7}$	$8.13\cdot10^{-8}$	0.49 ± 0.03
Pt/Co	9.8	2.9	1.6	1.3	$4.93\cdot10^{-7}$	$8.18\cdot10^{-8}$	0.43 ± 0.10
Pt/$Ni_{33}Fe_{67}$	9.8	3.0	2.0	1.0	$5.86\cdot10^{-7}$	$8.08\cdot10^{-8}$	0.44 ± 0.10
Pt/$Ni_{50}Fe_{50}$	10.0	3.0	2.0	1.0	$6.53\cdot10^{-7}$	$8.51\cdot10^{-8}$	0.35 ± 0.10
Pt/$Ni_{81}Fe_{19}$	9.9	3.0	2.0	1.0	$4.42\cdot10^{-7}$	$8.38\cdot10^{-8}$	0.22 ± 0.10
Pt/Ni	9.9	3.0	2.0	1.0	$4.08\cdot10^{-7}$	$8.21\cdot10^{-8}$	0.08 ± 0.08

The magnetic properties of the $Co_{1-x}Fe_x$ were investigated by AGM using a magnetic field up to 1.3 T. The magnetization of the FMM was extracted by hysteresis loops as indicatively presented in Figs. 5.8(a) and 5.8(c) for the $Co_{33}Fe_{67}$ and Co bilayers, respectively. Figures 5.8(b) and 5.8(d) exhibit the corresponding voltage extracted from the measurements in the IPM - no Pt configuration, which is attributed to the ANE^{FM} signal. In both cases, there is

an obvious similarity in shape between the magnetic curve and the voltage curve, reflecting that the observation of the ANE signal is closely related to the magnetic stimuli.

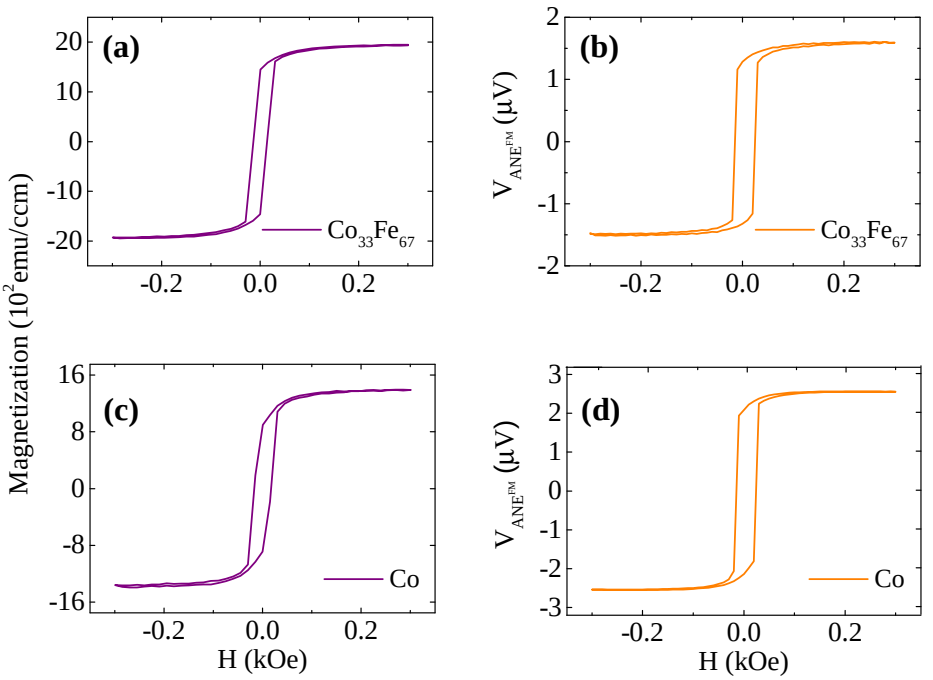

Figure 5.8. FMM magnetization extracted from AGM measurements for (a) $Co_{33}Fe_{67}$ and (c) Co bilayers, respectively. ANE^{FM} collected in the IPM - no Pt configuration for (b) $Co_{33}Fe_{67}$ and (d) Co bilayers, respectively.

Figure 5.9 illustrates the linear dependence of the electric field (voltage in saturation normalized to the electric contacts distance L_V) on the heat flux ϕ_q, for indicatively the Pt/Ni [Fig. 5.9(a)], Pt/Fe [Fig. 5.9(b)], Pt/Co [Fig. 5.9(c)], and Pt/$Co_{33}Fe_{67}$ [Fig. 5.9(d)] bilayers. The linear dependencies have been extracted after evaluating the loop measurements (electric field vs. magnetic field for a series of thermal fluxes) collected in the IPM - Pt, IPM - no Pt, and OPM - Pt configurations, for all sample series. The green points depict the signal collected in the IPM - Pt configuration which includes the LSSE contribution as well as the reduced ANE signals (LSSE+ANE^{FM}_{red}+ANE^{Pt}_{red}). The orange points exhibit the ANE^{FM} contribution measured in the IPM - no Pt configuration. The blue points concern the measured signal from the

OPM - Pt configuration, including both of the reduced ANE contributions (ANE^{FM}_{red}+ANE^{prox}_{red}). The dashed lines represent the calculated contributions of the pure LSSE (red) and ANE^{prox} (yellow) signals, after considering the correction factors *A* and *B* for the reduced ANE signals, due to the spin-polarized and non magnetic Pt layers, as introduced in Sec. 5.3. Again, for the determination of the correction factor *A*, the same resistivity ρ_{Pt} was used for the polarized and unpolarized fraction of the Pt layers. The amplitudes of the error bars are too small to be resolved in this Figure. The quantitative separation of the effects reveals that the ANE^{FM} contribution dominates in all cases. In addition, the non-zero ANE^{prox} signal indicates the existence of MPE for all samples confirmed by the Pt magnetic moments of Table 5.1, determined by XRMR.

Figure 5.10 depicts the dependence of the ANE^{FM} ($D^{FM}_{ANE} = \frac{E^{FM}_{ANE}}{\phi_q}$), SSE ($S_{SSE} = \frac{E_{SSE}}{\phi_q}$), and ANE^{prox} ($D^{prox}_{ANE} = \frac{E^{prox}_{ANE}}{\phi_q}$) coefficients on the Fe content x_{Fe} for both $Pt/Co_{1-x}Fe_x$ and $Pt/Ni_{1-x}Fe_x$ sample series, extracted from the corresponding slopes of the curves in Fig. 5.9. Considering the $Pt/Ni_{1-x}Fe_x$ sample series in Fig. 5.10(a), there is a pronounced increase of all coefficients with increasing Fe content. The ANE^{FM} is the dominant contribution and the ANE^{prox} possesses the lowest values for all compositions. The strength of the SSE contributions can be found in between. This behaviour is consistent with the trend depicted in Figs. 5.9(a) and 5.9(b).

Moreover, by comparing the concluded coefficients for the $Pt/Ni_{33}Fe_{67}$ bilayer with the results from the metallic sample reported in Sec. 5.4, we extract that S_{SSE} is comparable within the same order of magnitude whereas D^{FM}_{ANE} is quite higher in this work. This observation can be attributed to the higher ρ_{FM} of the $Ni_{33}Fe_{67}$ layer fabricated in this work and could be interpreted as follows. Both the ANE and AHE in a FM, involve the spin-dependent separation of charge carriers and, thus, they share the same origin of spin-orbit coupling. It is already established that there are two mechanisms contributing to the AHE, the intrinsic mechanism and the extrinsic one (skew scattering and side jump) [199], as already analyzed in Sec. 2.2. Both the intrinsic and side jump mechanisms obey the square relationship $\rho_{AHE} \propto \rho^2_{FM}$, where ρ_{AHE} and ρ_{FM} correspond to the AHE resistivity and the longitudinal resistivity, respectively [200]. Whereas, considering the skew scattering mechanism there is a linear dependence of ρ_{AHE} on ρ_{FM}. The same analogies hold for

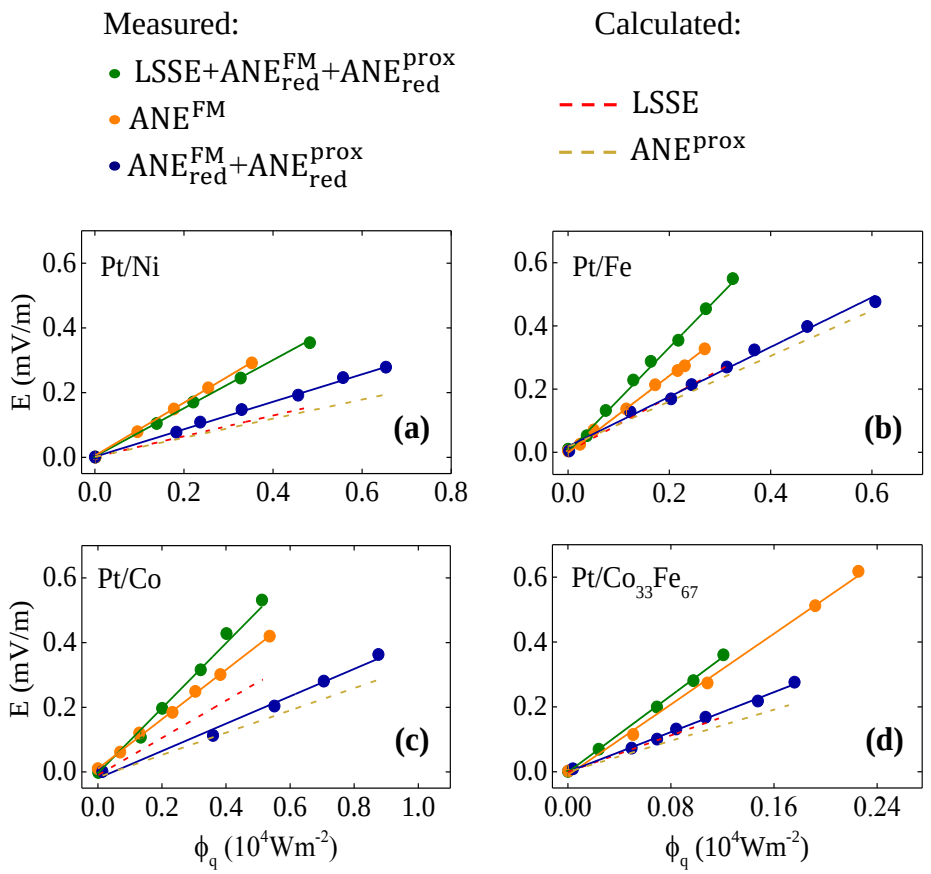

Figure 5.9. Electric field against the heat flux for (a) Pt/Ni, (b) Pt/Fe, (c) Pt/Co, and (d) $Pt/Co_{33}Fe_{67}$ samples with the corresponding separation of the ANE contribution (FM-induced and proximity-induced) from the LSSE signal.

the ρ_{ANE} [201]. Therefore, the D^{FM}_{ANE} is ρ_{FM}-dependent and we expect higher values for samples with higher ρ_{FM} values. In addition, Chuang *et al.* [201] reported an enhancement of ANE in FMMs (Fe, Co, Ni) which is dominated by spin-orbit coupling through the intrinsic and side-jump mechanisms. The ANE is very sensitive to the details of the electronic band structure and an enhancement of the intrinsic or side-jump contribution could increase the ANE signal. However, more systematic research should be conducted examining samples with the same stoichiometry and thickness, while tuning the intrinsic

and extrinsic contributions, by varying the electronic band structure and/or the defects' level.

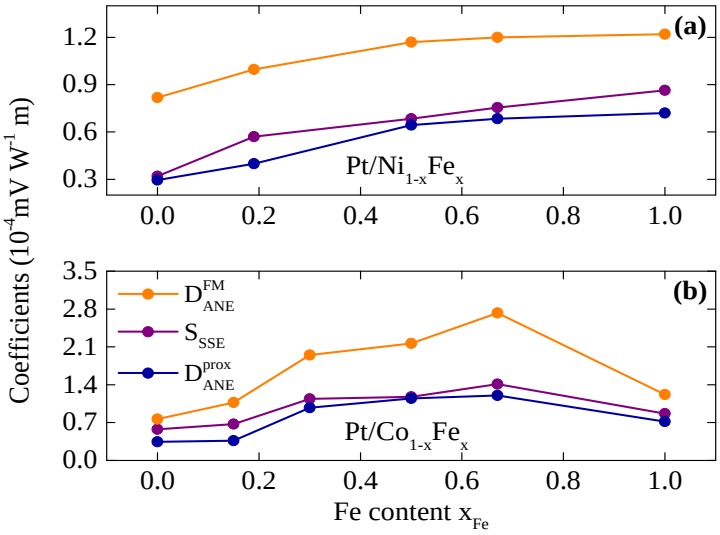

Figure 5.10. ANE^{FM} (D_{ANE}^{FM}), SSE (S_{SSE}), and ANE^{prox} (D_{ANE}^{prox}) coefficients as a function of the Fe content x_{Fe} in the (a) Pt/$Ni_{1-x}Fe_x$ and (b) Pt/$Co_{1-x}Fe_x$ sample series. The error bars are smaller than the size of each dot.

For the Pt/$Co_{1-x}Fe_x$ bilayers in Fig. 5.10(b), all coefficients increase with increasing Fe content peaking at the FMM bilayer Pt/$Co_{33}Fe_{67}$. For Pt on pure Fe, all coefficients decrease. Similarly to the Pt/$Ni_{1-x}Fe_x$ sample series, the ANE^{FM} is the dominant effect whereas the ANE^{prox} has the lowest contribution of the three. Again, the strength of the SSE contributions can be found in between. These observations also verify the tendency sketched in Figs. 5.9(c) and 5.9(d). It is worth noting that the dependence of all coefficients on the Fe content for both sample series, is qualitatively the same as the FMM and Pt moment dependence on the Fe content for the Pt/$Ni_{1-x}Fe_x$ [161] and Pt/$Co_{1-x}Fe_x$ [cf. Fig. 6.5(a)] sample series, respectively.

Figure 5.11 exhibits the dependence of D_{ANE}^{FM}, S_{SSE}, and D_{ANE}^{prox} on the corresponding FMM and Pt magnetic moments. For the Pt/$Ni_{1-x}Fe_x$ series [cf. Fig. 5.11(a)], all coefficients increase with increasing FMM moment, similarly to the behaviour in Fig. 5.10(a). Figure 5.11(b) presents the dependence of D_{ANE}^{prox} on the magnetic moment of the spin-polarized Pt layer extracted from XRMR

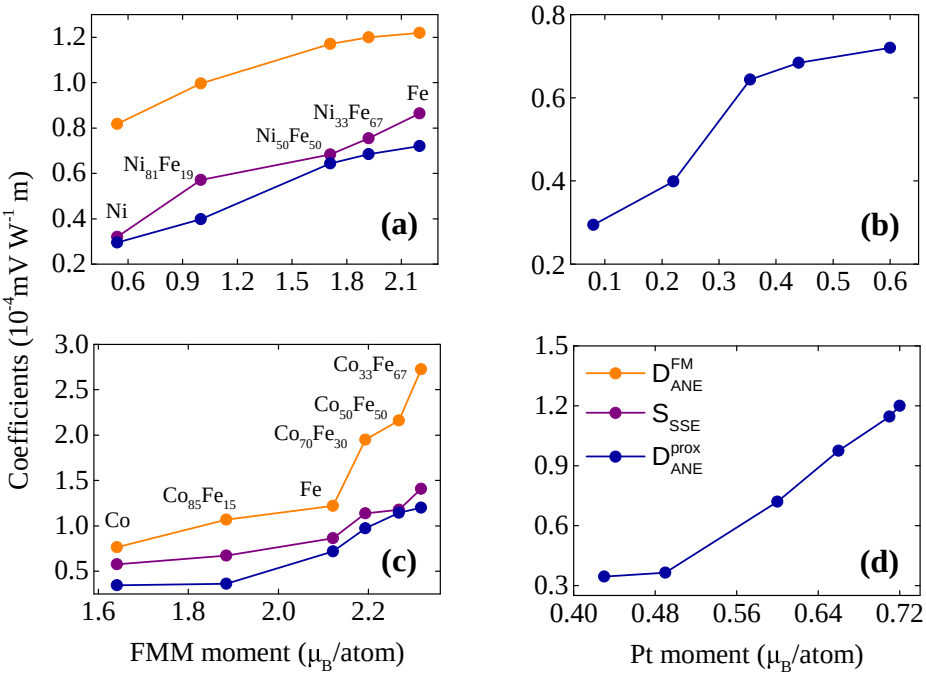

Figure 5.11. (a) Dependence of D^{FM}_{ANE}, S_{SSE}, and D^{prox}_{ANE} on the FMM moment and (b) D^{prox}_{ANE} dependence on the magnetic moment of the spin-polarized Pt layer, for Pt/$Ni_{1-x}Fe_x$ sample series. The FMM and Pt moments are taken from Refs. [132, 161] and the Pt moment for the $Ni_{50}Fe_{50}$ is interpolated data from Fig. 8 of Ref. [161]. (c) Dependence of D^{FM}_{ANE}, S_{SSE}, and D^{prox}_{ANE} on the FMM moment and (d) D^{prox}_{ANE} dependence on the magnetic moment of the spin-polarized Pt layer, for Pt/$Co_{1-x}Fe_x$ sample series. The FMM moments are calculated data from the measured magnetization values on the same samples. The Pt magnetic moments are taken from XRMR measurements (see Sec. 6.2 and Ref. [132]).

measurements, for each alloy in the Pt/$Ni_{1-x}Fe_x$ series [161]. The error bars in the x axis are included in Table 5.2 and left out from the graph for clarity reasons. The FMM and Pt magnetic moments are taken from Refs. [132, 161] and the Pt magnetic moment of the Pt/$Ni_{50}Fe_{50}$ bilayer is interpolated data from the data set in Fig. 8 of Ref. [161]. The strong correlation between the magnetic moment of the Pt and the ANE^{prox} is unveiled by the increase of D^{prox}_{ANE} with increasing Pt moment. For the Pt/$Co_{1-x}Fe_x$ bilayers [cf. Fig. 5.11(c)], all coefficients increase with increasing FMM moment, similarly to the $Ni_{1-x}Fe_x$

series. The FMM moments are calculated data from the measured magnetization values on the same samples, assuming bcc structures for all compositions apart from the $Co_{50}Fe_{50}$ (fcc) and Co (hcp) films. The Pt magnetic moments are extracted via XRMR measurements (see Sec. 6.2), except for the Pt/Fe sample for which the magnetic moment is taken from Ref. [132], measured on a similar Pt/Fe bilayer. Additionally, the increase of the Pt moment in the alloy results in the enhancement of ANE^{prox}, as observed in Fig. 5.11(d). Similarly to Fig. 5.11(b), the error bars in the x axis are left out from the graph, but can be looked up in Table 5.2.

The extracted trends of the coefficients for both sample series can be interpreted by considering in which manner a change in the FMM and Pt magnetic moments of the films could affect the investigating effects. According to Eq. (2.15), an increase of the magnetic moment in the FMM (Pt) layer would imply an enhancement of the measured electric field of the ANE^{FM} (ANE^{prox}). Thereby, the extracted trend of increasing/decreasing the ANE^{FM} (ANE^{prox}) coefficient with increasing/decreasing the FMM (Pt) magnetic moment, is the expected one for both sample series. In addition, the same behaviour has been reported by Srichandan *et al.* [202] when examining the thermoelectric power of $Co_{1-x}Fe_x$ thin films. They found an increase of the thermoelectric power in absolute values with increasing Fe content, in a range of $x_{Fe} = (30-80)\,\%$. Also, Ramos *et al.* reported a sign change in the transverse thermoelectric voltage of a $Co_{40}Fe_{60}$/YIG bilayer, attributed to the presence of an interface-driven ANE due to sd-type exchange at the interface. In our ANE measurements we do not see a sign change in th $Co_{33}Fe_{67}$ film. According to their interpretations, at $x_{Fe} = 70\,\%$ as well as at other contents close to this value, we should be able to detect this sign change. Probably the MgO substrate below the FM layers does not allow for the generation of such an interface-driven ANE in order to cause a sign change in our case.

Considering Eq. (2.6), a potential enhancement of the spin current flowing from the FMM to the Pt layer could induce a higher electric field (via ISHE) attributed to the SSE. Consequently, the observed behaviour of increasing the S_{SSE} with increasing the magnetic moment of both FMM and Pt layers, could be attributed to the existence of a larger number of magnons in the films. Under a thermal bias there is a non-equilibrium accumulation of these magnons at the NM/FMM interface which pump the spin current into the NM. The pumped spin current is then converted into a charge current in

the spin detecting NM. An alternative explanation could be that the higher magnetic moment in the FMM may indicate a higher magnetic density at the NM/FMM interface which would imply a subsequent increase of the spin Seebeck coefficient due to a change in the spin mixing conductance [203]. Furthermore, the extracted S_{SSE} for the $Pt/Ni_{33}Fe_{67}$ bilayer is within the same order of magnitude compared to the $Pt/NiFe_2O_x$ bilayers (see Sec. 5.4) and to the values reported by Rastogi *et al*. [204] on NFO/MgO samples and by Prakash *et al*. [205] on Pt/YIG films.

Chapter 6

MPE in NM/FM bilayers

This chapter demonstrates the results on the static MPE. XRMR is used to detect proximity induced spin polarization in bilayers with a Pt layer adjacent to different FMs. In the first part, we tackle the issue of the MPE existence in Pt adjacent to FM-semiconductor-like layers. The analysis of XRMR measurements on Pt/$NiFe_2O_x$ bilayers proves no magnetic response and provides upper limits for potential induced spin polarization in the Pt layer of these systems.

The second part focuses on the MPE investigations in Pt adjacent to different Co-Fe-based FMMs. Specifically, we systematically examined the dependence of the magnetic moment strength and magnetic anisotropy for the spin-polarized Pt layer on the FMM counterparts and formulated conclusions. All of the results presented here are either published [37, 190] or submitted for publication [206] and the following sections depend on the corresponding articles.

6.1 MPE in Pt/$NiFe_2O_x$ bilayers

The Pt/$NiFe_2O_x$ bilayers were fabricated by dc magnetron sputtering and deposited on top of (001)-oriented MAO substrates, as described in Sec. 3.1. The XRMR measurements were carried out at the XMaS beamline BM28 at ESRF (Grenoble, France) [207, 208], at RT. The XRMR data were collected at

a fixed energy close to the Pt L_3 absorption edge by performing XRR scans with circularly polarized x-rays (off-resonant at 11465 eV, resonant at 11565 eV) [37], while the field was switched between parallel and antiparallel orientation to the in-plane projection of the incident beam at every reflectivity angle. The degree of circular polarization was (88 ±1)% as derived from a model for the performance of the phase-plates [207]. The ratio $\frac{\Delta\beta}{\Delta\delta} = -14.3$ was kept fixed during fitting and was determined by adjusting the magnetooptic data from the *ab initio* calculations to a fixed q-scan [37]. We calculated this ratio at an energy of 11565 eV where we also collected our XRMR measurements.

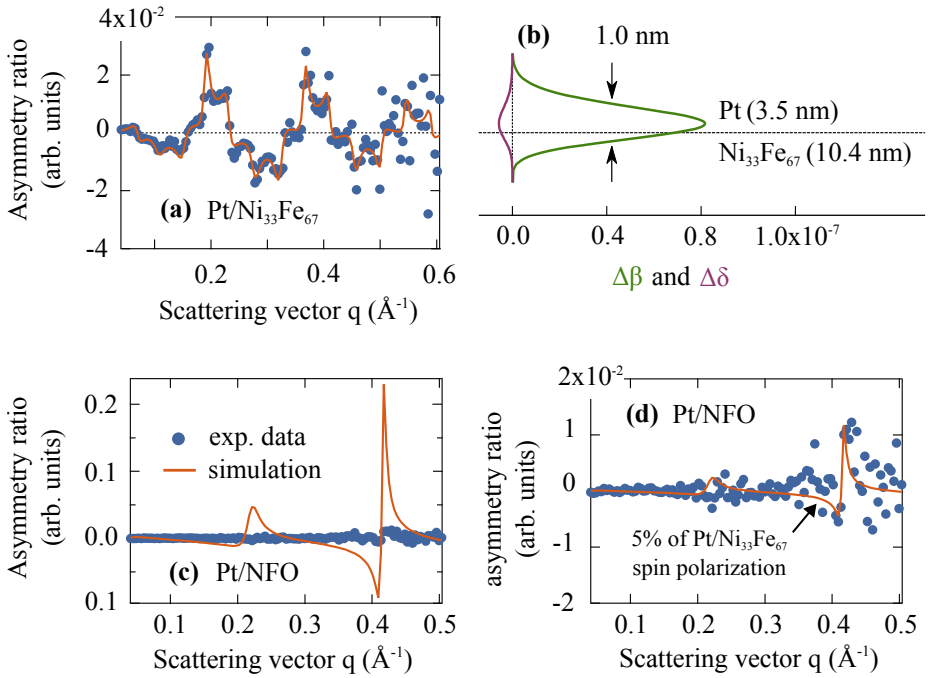

Figure 6.1. (a) XRMR asymmetry ratio for $Pt/Ni_{33}Fe_{67}$ and simulation with the corresponding magnetooptic depth profile (b). (c) XRMR asymmetry ratio for Pt/NFO after using the magnetooptic depth profile of (b), (d) close-up of the experimental data from (c) and simulation assuming 5% of the $Pt/Ni_{33}Fe_{67}$ spin polarization.

In Fig. 6.1 the measured XRMR asymmetry ratios and their simulation are presented for the $Pt/Ni_{33}Fe_{67}$ and Pt/NFO bilayers, using the corresponding magnetooptic depth profile for the metallic sample. In Fig. 6.1(a) the mea-

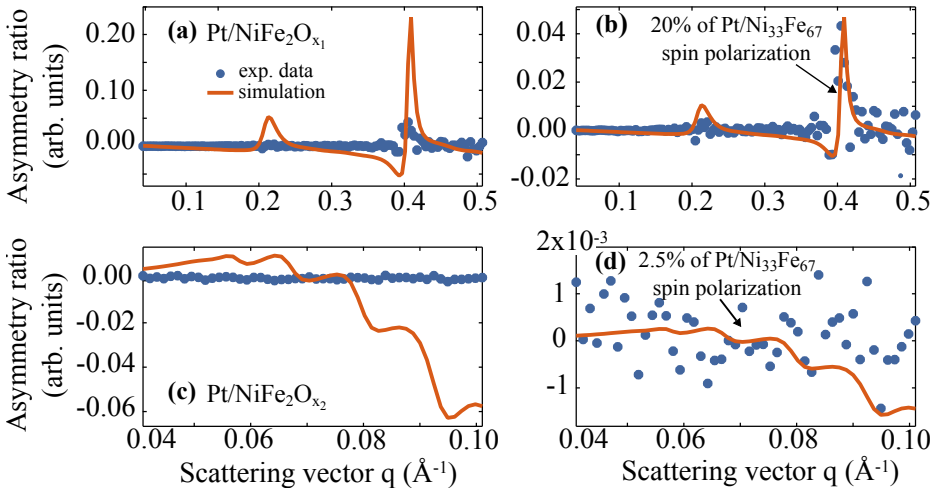

Figure 6.2. (a) XRMR asymmetry ratio for $Pt/NiFe_2O_{x_1}$ and simulation using the magnetooptic depth profile of the $Pt/Ni_{33}Fe_{67}$ bilayer, (b) assuming 20% of the $Pt/Ni_{33}Fe_{67}$ spin polarization. (c) XRMR asymmetry ratio for $Pt/NiFe_2O_{x_2}$ and simulation using the magnetooptic depth profile of the $Pt/Ni_{33}Fe_{67}$ bilayer, (d) assuming 2.5% of the $Pt/Ni_{33}Fe_{67}$ spin polarization.

sured XRMR asymmetry ratio for the $Pt/Ni_{33}Fe_{67}$ bilayer is displayed. From the corresponding fitting and by comparing the experimental fit values of $\Delta\delta$ and $\Delta\beta$ derived from the magnetooptic depth profile in Fig. 6.1(b) to *ab initio* calculations [132], we obtain a maximum Pt magnetic moment of $(0.48 \pm 0.08)\,\mu_B$ per spin-polarized Pt atom. The effective spin-polarized Pt thickness is calculated to be (1.0 ± 0.1) nm, similar to previous investigations [161].

In Fig. 6.1(c) the measured XRMR asymmetry ratio for the Pt/NFO bilayer is presented along with a simulation using a magnetooptic depth profile identical to the one derived for the $Pt/Ni_{33}Fe_{67}$ bilayer. Obviously, the simulated asymmetry ratio of the Pt/NFO sample [Fig. 6.1(c)] deviates strongly from the one of the $Pt/Ni_{33}Fe_{67}$ sample [Fig. 6.1(a)], although the same magnetooptic depth profile [Fig. 6.1(b)] was used. This is due to the different optical constants of $Ni_{33}Fe_{67}$ and NFO. Since no asymmetry was detected for the Pt/NFO sample, a potential MPE present in this film must be significantly smaller than in the all-metallic system. By decreasing the magnitude of the magnetooptic parameters down to 5% of the $Pt/Ni_{33}Fe_{67}$ spin polarization

[Fig. 6.1(d)], we can estimate a detection limit leading to an upper limit for the maximum magnetic moment in Pt of 0.04 μ_B per spin-polarized Pt atom.

In Fig. 6.2 the measured XRMR asymmetry ratio is presented for the Pt/$NiFe_2O_{x_1}$ [Figs. 6.2(a) and 6.2(b)] and Pt/$NiFe_2O_{x_2}$ bilayers [Figs. 6.2(c) and 6.2(d)], respectively, along with a simulation using a magnetooptic depth profile identical to the one derived for the Pt/$Ni_{33}Fe_{67}$ bilayer. Firstly, we compare the experimental data with an asymmetry ratio simulation that describes a Pt/$NiFe_2O_x$ system but with the same magnetooptic depth profile as for Pt/$Ni_{33}Fe_{67}$. As in the case of the Pt/NFO analyzed previously, the simulated asymmetry ratio of the Pt/$NiFe_2O_{x_1}$ [Fig. 6.2(a)] deviates strongly from the one of the Pt/$Ni_{33}Fe_{67}$ sample, although the same magnetooptic depth profile was used [Fig. 6.1(b)], due to the different optical constants of $Ni_{33}Fe_{67}$ and $NiFe_2O_{x_1}$. Therefore, since the simulated asymmetry ratio of the Pt/$NiFe_2O_{x_1}$ sample does not match the experimental data, a potential MPE present in this film must be significantly smaller than in the all-metallic system. In order to extract a limit for a quantitative magnetic moment value, we decreased the magnitude of the magnetooptic parameters down to 20% of the Pt/$Ni_{33}Fe_{67}$ spin polarization [Fig. 6.2(b)] and, thus, we estimated a detection limit leading to an upper limit for the maximum magnetic moment in Pt of 0.1 μ_B per spin-polarized Pt atom. Accordingly, for the Pt/$NiFe_2O_{x_2}$ bilayer we decreased the magnitude of the magnetooptic parameters down to 2.5% of the Pt/$Ni_{33}Fe_{67}$ spin polarization [Fig. 6.2(d)] and we estimated a detection limit leading to an upper limit for the maximum magnetic moment in Pt of 0.01 μ_B per spin-polarized Pt atom. The extracted limits for both samples are different compared to Pt/NFO due to different signal-to-noise ratios in the XRMR data. Finally, possible MPEs can be neglected down to these limits for all samples except for the metallic Pt/$Ni_{33}Fe_{67}$ bilayer, where a distinct spin polarization in the Pt layer can be observed.

6.2 MPE in Pt/$Co_{1-x}Fe_x$ bilayers

The Pt/$Co_{1-x}Fe_x$ bilayers were deposited on top of (001)-oriented MgO substrates by dc magnetron sputtering (see Sec. 3.1) and the synchrotron measurements were carried out at the resonant scattering and diffraction beamline P09 of the third generation synchrotron PETRA III at DESY (Hamburg, Ger-

many) [209]. A six-circle diffractometer was used to perform XRR scans in a $\theta - 2\theta$ scattering geometry, at RT. The external magnetic field of ±80 mT was applied with a four coils electromagnet during the reflectivity scan. The XRR intensity $I_{\pm}$ for left and right circularly polarized light, respectively, was detected off resonance (11465 eV) and at resonance at the L_3 absorption edge of Pt (11565 eV), switching fast the helicity of incident circular polarization [209]. The degree of circular polarization was (99±1)% for left and right circularly polarized light, as determined from a polarization analysis with a Au(111) analyzer crystal. The circular polarization was achieved by one single quarter-wave-plate of 850 μm thickness.

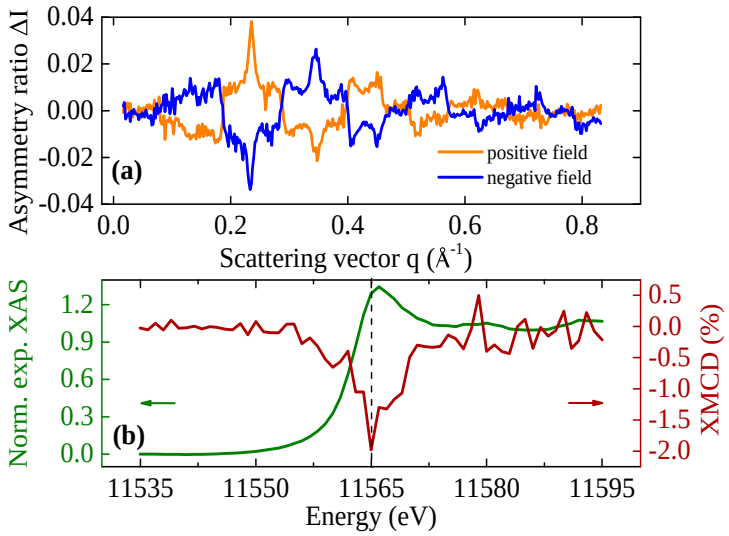

Figure 6.3. (a) Resonant (11565 eV) asymmetry ratio $\Delta I(q)$ for both magnetic field directions. (b) Experimental energy dependant XAS spectrum (green line) and the XMCD signal (red line). All data correspond to the $Pt/Co_{50}Fe_{50}$ bilayer.

Figure 6.3(a) presents the XRMR asymmetry ratio ΔI for the $Pt/Co_{50}Fe_{50}$ bilayer plotted against the scattering vector q. The effect changes sign when the magnetic field direction is reversed which confirms its magnetic origin. Figure 6.3(b) depicts the experimental energy dependant XAS spectrum (green line) at the Pt L_3 edge normalized to the edge jump, after the subtraction of a linear background. The XMCD spectrum was collected using an energy dispersive silicon drift detector synchronized with the piezo-actuators underneath the

phase plates, allowing for the fluorescent photons for left and right circular polarized incident light to be counted separately at every point of the scan. In order to investigate the magnetic anisotropy of the spin-polarized Pt layer, we collected XRMR magnetic field loops for different in-plane sample orientations and a fixed scattering vector q that corresponds to a maximum asymmetry ratio ΔI. The XMCD intensity $(I_+ - I_-)/2$ is also displayed in the figure and was extracted to identify the energy with the largest dichroism. The magnetic dichroism of the spin-polarized Pt has its maximum slightly below the absorption maximum (dashed line) which is in agreement with previous findings [37, 132, 161, 210] and, thus, the chosen energy to collect the XRMR data was at 11565 eV.

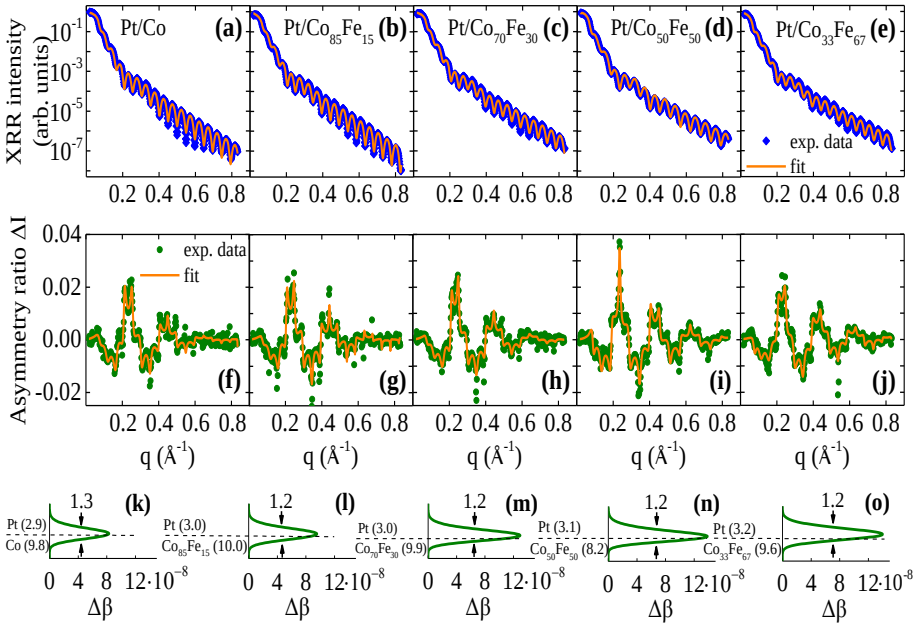

Figure 6.4. (a)-(e) Resonant (11565 eV) XRR scans and fits with (f)-(j) the corresponding determined and fitted XRMR asymmetry ratios $\Delta I(q)$ for all $Pt/Co_{1-x}Fe_x$ bilayers. (k)-(o) Magnetooptic depth profiles which were used to fit the XRMR asymmetry ratios. The thicknesses of the layers are presented in nm. The dashed lines denote the corresponding interface position between Pt and $Co_{1-x}Fe_x$ layers. The arrows indicate the FWHM of the spin-polarized layer obtained from the structural parameters of the XRR fits.

Figure 6.4 presents the XRR and XRMR data as well as the resulting magnetooptic depth profiles for all $Pt/Co_{1-x}Fe_x$ bilayers. Figures 6.4(a)-(e) show the averaged resonant magnetic XRR scans, collected at a photon energy of 11565 eV, plotted against the scattering vector q and accompanied by their fittings. Kiessig fringes appear in all scans due to the interference of the reflected light from the $Pt/Co_{1-x}Fe_x$ and $Co_{1-x}Fe_x/MgO$ interfaces. By fitting the off-resonant (11465 eV) XRR curves we obtain the thickness [indicated in Figs. 6.4(k)-(o)] and roughness (typical values for the NM/FMM interfaces are between 0.20 nm and 0.38 nm), using literature β and δ values for the individual layers. In a second step, we kept the structural parameters fixed for fitting the averaged resonant (11565 eV) XRR curves following the description of Klewe *et al*. [161], thus, obtaining the resonant β and δ values. When fitting the XRMR asymmetry ratios the structural parameters from the off-resonant XRR fit and the optical values from the resonant XRR fit have been kept fixed and just the $\Delta\beta$ depth profile has been varied. The variation of the dispersion $\Delta\delta$ crossed zero around the absorption edge and for that reason we kept $\Delta\delta = 0$ during the XRMR fits.

The derived XRMR asymmetry ratios $\Delta I(q)$ are illustrated in Figs. 6.4(f)-(j), plotted together with the corresponding fittings. In all cases, pronounced oscillations are visible with an amplitude of about 2% comparable to our earlier studies [37, 132, 161] and additional maxima that can reach up to 4%, unveiling an induced spin polarization in Pt.

Figures 6.4(k)-(o) display the magnetooptic depth profiles of $\Delta\beta$, which were used to fit the XRMR asymmetry ratios in Figs. 6.4(f)-(j). The magnetooptic profiles were generated by a Gaussian function at the $Pt/Co_{1-x}Fe_x$ interface, convoluted with the roughness profile of the corresponding layer [161]. For all magnetooptic profiles, we extracted the full width at half maximum (FWHM) which represents the effective thickness of the spin-polarized Pt layer at the $Pt/Co_{1-x}Fe_x$ interface. This effective spin-polarized Pt thickness is between 1.2 nm and 1.3 nm for all samples as indicated in Figs. 6.4(k)-(o) and it is not affected by the FMM magnetic moment. By comparing the experimental fit values of $\Delta\beta$ with the *ab initio* calculations of Ref. [132], we extracted the magnetic moment per spin-polarized Pt atom at the maximum of the magnetooptic profile, as summarized in Table 6.1, for all FMM compositions. For completeness, the magnetic moment of the Pt/Fe sample is taken from Ref. [132], where a similar sample with comparable thicknesses was

used. A pronounced behaviour is clearly displayed with increasing Pt moment for higher Fe content values, peaking at the $Pt/Co_{33}Fe_{67}$ bilayer.

Table 6.1. Induced Pt magnetic moment in $Pt/Co_{1-x}Fe_x$ bilayers extracted from XRMR measurements. [1]Value taken from Ref. [132].

Composition	Pt moment μ_B/Pt atom
Pt/Fe[1]	0.60 ± 0.10
$Pt/Co_{33}Fe_{67}$	0.72 ± 0.03
$Pt/Co_{50}Fe_{50}$	0.71 ± 0.03
$Pt/Co_{70}Fe_{30}$	0.66 ± 0.03
$Pt/Co_{85}Fe_{15}$	0.49 ± 0.03
Pt/Co	0.43 ± 0.03

Figure 6.5(a) presents the Pt magnetic moment for all samples (blue points), plotted against the Fe content x together with the magnetic moment values of the $Co_{1-x}Fe_x$ alloys (orange data), taken from Ref. [211]. The error bars are estimated by changing the β values until the goodness of fit value χ^2 increases up to 20 %. In our prior studies [37, 132, 161] we just roughly estimated the uncertainty, therefore, the previous error values have been slightly larger. The inset depicts a close-up plot of the graph. As visible, the magnetic moments in Pt clearly exhibit a similar progress as the magnetic moments in the $Co_{1-x}Fe_x$ alloys, which follow the Slater-Pauling curve [212]. Both Pt and FMM moments increase with increasing x, peaking at a certain content ratio which is the $Co_{28}Fe_{72}$ alloy for the literature values and the $Pt/Co_{33}Fe_{67}$ bilayer for our experimental data. For further increase of Fe content, both Pt and FMM moments decrease. Consequently, we conclude that the strength of the magnetic coupling between the two layers depends on the magnitude of the magnetic moment in the FMM, as indicated by Klewe *et al.* for $Pt/Ni_{1-x}Fe_x$ bilayers [161] and by Poulopoulos *et al.* [158] for Ni/Pt multilayers. This is valid as long as Pt is deposited on FMMs. If Pt is grown on magnetic semiconductors or insulators, the dependence of Pt moment on FM moment can be different or nonexistent due to a vanishing MPE [37, 131–134, 213].

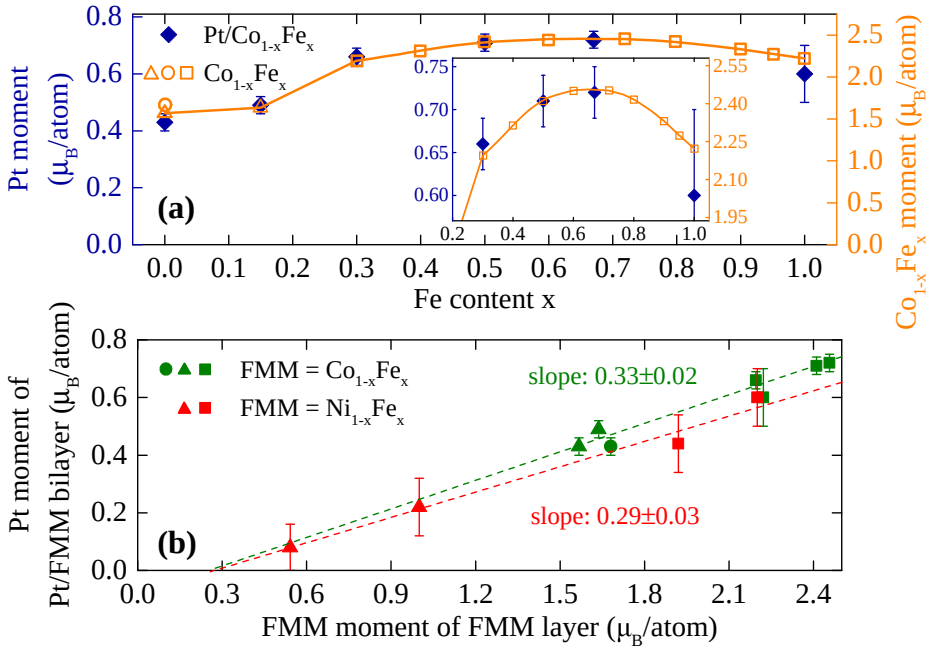

Figure 6.5. (a) Pt magnetic moment plotted against the Fe content x of $Pt/Co_{1-x}Fe_x$ bilayers (blue points). The orange data is taken from Ref. [211] displaying the magnetic moment per atom as derived from magnetization measurements for $Co_{1-x}Fe_x$ alloys. The inset depicts a close-up plot emphasizing the maximum experimental Pt magnetic moment in $Pt/Co_{33}Fe_{67}$. The data of Pt/Fe is taken from Ref. [132]. (b) Pt magnetic moment plotted against the FMM magnetic moment for both $Pt/Co_{1-x}Fe_x$ (green points) and $Pt/Ni_{1-x}Fe_x$ (red points, taken from Refs. [132, 161]) bilayers, respectively. The green (red) dashed line is a linear fit to the data with a slope equal to 0.33 ± 0.02 (0.29 ± 0.03), for the $Pt/Co_{1-x}Fe_x$ ($Pt/Ni_{1-x}Fe_x$) bilayers. In both graphs, the squares, triangles, and circles correspond to FMMs with bcc, fcc, and hcp crystal structure, respectively.

Figure 6.5(b) exhibits the dependence of Pt magnetic moment on the FMM magnetic moment for both $Pt/Co_{1-x}Fe_x$ (green points) and $Pt/Ni_{1-x}Fe_x$ (red points, taken from Refs. [132, 161]) bilayers. The dashed lines are linear fits of the data and indicate the linear dependence between the Pt and FMM magnetic moments in such bilayer systems. In addition, the slopes of both curves, as depicted in the graph, are comparable to each other considering the errors. The slope of the Pt moment linear dependence on the FMM moment

might be interpreted as the distance to the Stoner criterion. The systematic behaviour for Pt on top of other classes of materials (such as semiconductors or slightly oxygen-reduced ferrites) or for other NM materials (such as Pd) on FMMs, should be investigated in order to further clarify the underlying physical mechanism.

Another interesting feature of the graph is the offset of the x axis which indicates a minimum FMM moment that is required to induce magnetism in the adjacent Pt layer. This could be possibly attributed to the formation of a magnetic dead layer at the Pt/FMM interface which prohibits the exchange interactions between the FMM and Pt layers, for weak FMM moments. However, further investigation should be conducted employing samples with varied magnetic dead layer thicknesses, to gain further insight in the underlying mechanism.

As a next step, we investigated the magnetic anisotropy of Fe and $Co_{50}Fe_{50}$ samples by performing MOKE rotational measurements with different in-plane crystal orientation directions ($0° \geq \alpha \geq 360°$ in steps of 5°), in the presence of an in-plane magnetic field. The azimuthal angle α corresponds to the angle between the direction of the applied magnetic field and the [110] direction of the corresponding alloy, as sketched in the inset of Figs. 6.6(c) and 6.6(d). In order to examine the magnetic anisotropy of the spin-polarized Pt layer, we collected XRMR field loop measurements, for different sample orientations ($0° \geq \alpha \geq 45°$ in steps of 15°).

Figures 6.6(a) and 6.6(b) present the squareness, which is the ratio between the magnetic remanence and the saturation magnetization, extracted from the MOKE loops (not shown) for the Fe and $Co_{50}Fe_{50}$ samples and from XRMR field loops for the Pt/Fe and Pt/$Co_{50}Fe_{50}$ samples. For the Fe film [cf. Fig. 6.6(a)], the MOKE measurements reveal magnetic easy axes along the Fe<100> directions, which correspond to the MgO<110> directions ($\alpha = 45°, 135°, 225°, 315°$) with high remanence values and magnetic hard axes along the the Fe<110> directions corresponding to the MgO<100> directions ($\alpha = 0°, 90°, 180°, 270°$) with low remanence values [214, 215]. On the other hand, for the $Co_{50}Fe_{50}$ sample [cf. Fig. 6.6(b)] the four-fold magnetic anisotropy is 45° rotated compared to Fe. Therefore, the magnetic easy axes for the $Co_{50}Fe_{50}$ sample are aligned along the CoFe<110> directions which are the MgO<100> directions with high remanence values, whereas the magnetic

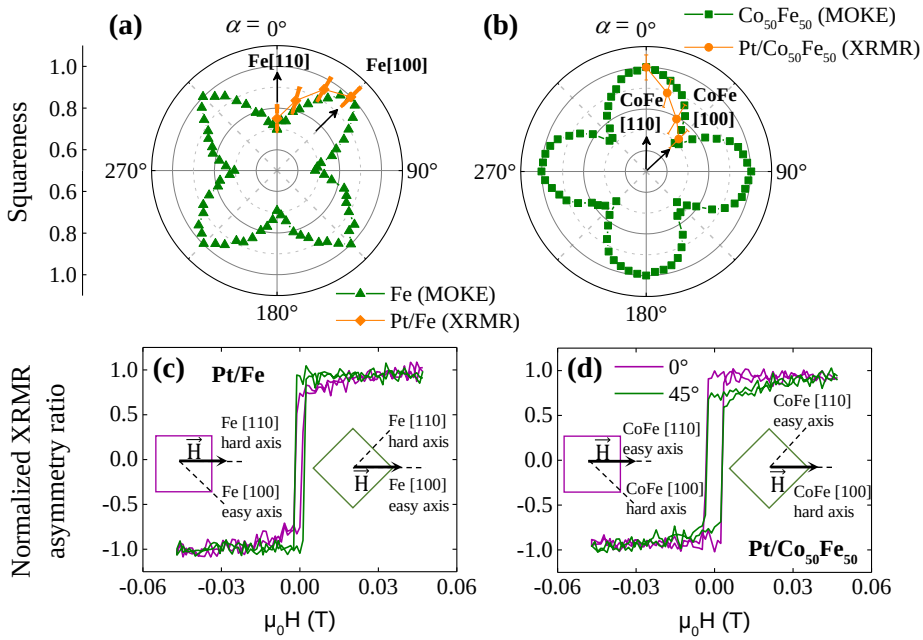

Figure 6.6. Squareness plotted against the value of the azimuthal angle α for (a) Fe (MOKE), Pt/Fe (Pt element-selective XRMR) and (b) $Co_{50}Fe_{50}$ (MOKE), Pt/$Co_{50}Fe_{50}$ (Pt element-selective XRMR) samples, collected at RT. The angle α corresponds to the angle between the direction of the applied magnetic field and the [110] direction of the corresponding alloy, as sketched in the inset of Figs. (c) and (d). The purple (green) square corresponds to the orientation of the MgO substrate with respect to the direction of the applied magnetic field leading to $\alpha = 0°$ ($\alpha = 45°$). Detected XRMR asymmetry ratio field loops with $\alpha = 0°, 45°$ for (c) Pt/Fe and (d) Pt/$Co_{50}Fe_{50}$ bilayers, collected in resonance (11565 eV) and with a q value of 0.24 $Å^{-1}$.

hard axes are aligned along the CoFe<100> directions corresponding to the MgO<110> directions with low remanence values [216, 217].

In Figs. 6.6(c) and 6.6(d) two normalized XRMR field loops for Pt/Fe and Pt/$Co_{50}Fe_{50}$ samples are illustrated for $\alpha = 0°$ and 45°, respectively. For the Pt/Fe bilayer [Fig. 6.6(c)], the spin-polarized Pt layer showed the magnetic easy axis for $\alpha = 45°$ (green curve) and the magnetic hard axis for $\alpha = 0°$ (purple curve), which is consistent with the results extracted from the previously analyzed MOKE measurements of the pure Fe layer. In addition, for the Pt/$Co_{50}Fe_{50}$ sample [Fig. 6.6(d)] the magnetic easy axis appeared for

$\alpha = 0°$ (purple curve) and the magnetic hard axis was found at $\alpha = 45°$ (green curve), which also coincides with the MOKE results of the pure $Co_{50}Fe_{50}$ film. Moreover, the extracted squareness values from the XRMR field loops for the Pt/Fe and Pt/$Co_{50}Fe_{50}$ samples are included in Figs. 6.6(a) and 6.6(b), respectively. The spins in the spin-polarized Pt layer are strongly coupled to the FMM spins through Heisenberg exchange interactions and, thus, the magnetic anisotropy of the spin-polarized Pt layer on top of the FMM (where FMM is Fe or $Co_{50}Fe_{50}$) reflects the magnetic anisotropy of the underlying FMM.

Chapter 7

Summary & Outlook

In summary, the main focus of this thesis lies on the investigation and quantitative disentanglement of thermal spin transport phenomena in NM/FM bilayer systems, tackling the challenging issue of the proximity-induced effect contributions. We examined different bilayer combinations from variable material classes ranging from FMIs and FM-semiconductor-like layers to FMMs. As thoroughly discussed in the thesis, MPE is a key element of spintronics which could modulate and emerge the functionality of future spintronic and spin caloritronic devices, based on the investigated heterostructures. Therefore, the fabricated structures were systematically investigated for a static MPE in terms of an induced interface spin polarization in the NM layer (Pt) and, furthermore, the correlations of the MPE with the electrical and magnetic parameters of the samples were pointed out.

As a first step, we fabricated the thin inverse spinel ferrite $NiFe_2O_x$ with reactive dc magnetron co-sputtering. By reducing the oxygen content below its stoichiometric value ($x = 4$), we tuned the conductivity, the band gap, and the electrical transport mechanisms. Beside structural and magnetic characterization, we investigated the localization of electronic states and the disorder of these systems by temperature dependent electrical resistivity measurements as well as the optical band gap and semiconducting properties, by absorption experiments and Hall effect studies. We extracted optical band gap energies in a range of (1.09-1.49) eV. We further concluded that different conduction mechanisms govern our systems in the examined low and high

temperature regimes. Resistivity measurements in the high temperature regime unveiled the Arrhenius type of conduction for the delocalization of the carriers. We obtained low thermal activation energies for all samples in a range of (0.05-0.19) eV, indicating a semiconducting behaviour. Furthermore, in the low temperature regime, Mott-VRH was the dominant conduction mechanism underpinning the impurity-based type of conduction. Moreover, using Hall effect measurements, a semiconducting n-type character was identified in the films along with the corresponding densities and mobilities of the charge carriers.

Since our aim was to quantitatively disentangle the thermal spin transport phenomena in NM/FM bilayers, we first studied the LSSE on NM/FMI bilayer system (Pt/YIG). In such system, we expect the absence of the parasitic FM-induced ANE due to the lack of free carriers. The proximity-induced ANE contribution could rather exist, when the Pt becomes spin-polarized. However, the general question of MPE in Pt/FMIs is still open since it cannot be excluded due to its strong dependence on the interface configuration of each bilayer. The controversial results reported within the research community, dictate the necessity for further investigations to be implemented in order for reliable conclusions to be drawn. In collaboration with INRIM, we performed the LSSE experiments on the Pt/YIG film by using different setups and employing both the temperature difference and the heat flux method. We concluded that the LSSE coefficient can be measured reproducibly and with a low uncertainty ($\approx 3\,\%$) only by using the approach based on the heat flux method.

Apart from FMIs, when utilizing FM-semiconductors and FMMs in LSSE experiments, an additional ANE from the conducting FM as well as a proximity-induced ANE from the spin-polarized NM layer may contribute to the measured LSSE signal. To handle this issue, we proposed a compact procedure which was based on different measurement geometries, the normalization to the heat flux instead of the thermal gradient, and the determination of important correction factors to obtain quantitative LSSE and ANE values. In turn, we utilized the proposed technique to disentangle the LSSE from the ANE contributions in Pt on $NiFe_2O_x$ samples, studying the transition from FMI (NFO) to FMM ($Ni_{33}Fe_{67}$). We obtained the dominant LSSE contribution for all Pt/$NiFe_2O_x$ bilayers that consist of oxides with the spin Seebeck effect coefficient to range from $S_{\mathrm{SSE}} = 0.49 \cdot 10^{-4}\,\mathrm{mVW^{-1}m}$ to $S_{\mathrm{SSE}} = 0.99 \cdot 10^{-4}\,\mathrm{mVW^{-1}m}$, for the most conducting to the most insulating sample, respectively. Moreover, we found

no proximity-induced ANE, except for the metallic case. The FM-induced ANE was enhanced in the FMM compared to the $NiFe_2O_x$ samples owing to its conducting character. We also were able to extract the dependence of the effects' coefficients on the band gap energy and on the electrical conductivity of the samples. We pointed out that the LSSE increases monotonically with the band gap energy whereas the FM-induced ANE decreases. Furthermore, we identified the increase of ANE with increasing conductivity while the LSSE decreases.

As a next step, we employed our technique to disentangle the aforementioned effects on metallic systems using $Co_{1-x}Fe_x$ and $Ni_{1-x}Fe_x$ films, with a spin-polarized Pt layer on top. We reported a strong dependence of all effects on the FMM composition showing a qualitative analogy of increasing/decreasing the effects' coefficients with increasing/decreasing the magnetic moments of both the FMM and the spin-polarized Pt layer. Specifically, the extracted trend of increasing the S_{SSE} with increasing the magnetic moment of both FM and Pt layers could be attributed to a potential enhancement of the spin current flowing from the FM to the Pt layer, inducing a higher electric field (via ISHE). Alternatively, a higher magnetic moment in the FMM may indicate a higher magnetic density at the NM/FMM interface which would imply a subsequent increase of the S_{SSE} due to a change in the spin mixing conductance. Additionally, an increase of the magnetic moment in the FMM (Pt) layer would imply an enhancement of the measured electric field of the ANE_{FM} (ANE_{prox}), thus explaining the observed behaviour of increasing/decreasing the ANE_{FM} (ANE_{prox}) coefficient with increasing/decreasing the FMM (Pt) magnetic moment. The results were discussed in the context of the current literature.

In order to evaluate and verify the results obtained by the transport measurements, we systematically studied the interface properties of the NM/FM bilayer systems, in terms of possible static MPEs in Pt. We used the element-selective XRMR to quantify the Pt magnetic moment on top of NFO and $NiFe_2O_x$ films. We found no magnetic response down to our detection limits for Pt/NFO and Pt/$NiFe_2O_x$ whereas for the Pt/$Ni_{33}Fe_{67}$ bilayer we identified a clear induced spin polarization in Pt of $(0.48 \pm 0.08)\,\mu_B$/Pt atom. The XRMR results are in line with the absence/presence of the proximity-induced ANE contributions in the transport measurements.

Since we proved that the MPE varies for different material combinations (e.g. insulators vs. metals), in the last experimental section we set the focus on the dependence of MPE on material parameters within one class of material, such as FMMs. We again employed XRMR measurements on $Pt/Co_{1-x}Fe_x$ bilayers, to quantify the induced Pt spin polarization as well as to probe the magnetic anisotropy of the spin-polarized Pt layer. We extracted the maximum induced magnetic moment of $(0.72 \pm 0.03)\,\mu_B$/Pt atom of Pt on $Co_{33}Fe_{67}$, while the minimum Pt magnetic moment of $(0.43 \pm 0.03)\,\mu_B$/Pt atom was identified for the Pt/Co bilayer. We further confirmed that the magnetic moment in Pt follows the Slater-Pauling curve of magnetic moments in $Co_{1-x}Fe_x$ alloys and the magnetic anisotropy of the spin-polarized Pt layer reflects the magnetic anisotropy of the FMM in the corresponding alloy. In a next step, we investigated the efficiency of the MPE in $Pt/Co_{1-x}Fe_x$ and $Pt/Ni_{1-x}Fe_x$ systems extracting a linear dependence between the Pt and FMM magnetic moments. We evaluated the results stating that the slope of this linear dependence could give an experimental access to the Stoner criterion. As a progression of this work, additional research will be conducted exploring a series of different material system combinations utilizing different Stoner-instable materials (e.g. Pd) on different FMM films, to create a full FMM moment and conductivity mapping of the MPE in various NMs. Via this process we will gain a deeper insight into the MPE mechanism, supporting the implementation of such systems into spintronic and spin caloritronic devices.

As a continuation of this thesis, the separation of the aforementioned effects will be investigated in sputter-deposited Pt/Fe_3O_4 bilayers, where proximity-induced phenomena are also possible to emerge. A further quite promising topic will be to compare the sensitivities between the XRMR and our effect separation technique, to identify proximity induced magnetization in the examined systems. This idea could be studied via the fabrication of oxygen-reduced latticed matched $NiFe_2O_x$ samples which present an MPE, either verified by XRMR investigations or via the quantitative identification of the ANE_{prox}. An equally challenging issue would be to apply this separation technique on multilayer systems as well as in low temperature regimes since the FM magnetization and, thus, the induced spin polarization to the NM could be temperature dependent. A matter of significant importance regards the knowledge of the thermal conductivity (at the corresponding temperature) of the individual layer in the system and the evaluation of any possible interfacial

contributions of the effects. For example, thickness dependent measurements for each single layer could unveil both the bulk and the interface effect's contributions.

Considering that both magnons and conduction electrons could contribute in the measured LSSE signal when FMMs and FM-semiconductors are employed, a future separation between both contributions could be of major importance since it would further elucidate the underlying physics of the SSE. This concept could be examining by performing LSSE experiments in a series of NM/FMM bilayers while varying the FMM thickness. We expect two saturation effects in the thickness dependent measurements of the SSE coefficient. The first one originates from the spin diffusion length of the spin carrying electrons governing the thickness dependence graph for law thicknesses and the second one is attributed to the magnon propagation length which is found to be some hundreds of nm [87]. Promising FMM candidates are materials with low damping, since, thus, the electron spin propagation and the magnon transport are independent (weak interaction). Consequently, the two characteristic thicknesses could be identified.

Furthermore, in close collaboration with the group of Prof. Dr. A. Gupta in Alabama University, the LSSE coefficient will be examined in Pt/NFO bilayers deposited on top of better latticed matched substrates (e.g. $MgGa_2O_4$ and $CoGa_2O_4$), expressing higher values compared to the Pt/NFO/MAO films due to the improved structural, interfacial, and dynamical properties. The films are grown via pulsed laser deposition. A further idea within this project is the investigation of the SSE in sputtered deposited NFO samples, using the aforementioned improved lattice matched $MgGa_2O_4$ and $CoGa_2O_4$ substrates, for the detection of the *magnon-polaron*. In particular, under the application of high magnetic fields (around 4 T) in the SSE measurements, magnons and phonons are allowed to hybridize leading to the *magnon-polaron* formation which can be detected as spike structures in the recorded signal. The magnon-polaron formation has been reported on both local magnon spin injection/detection geometries in Pt/YIG films [218] and nonlocal geometries (a certain distance separates the spin injection and detection contacts) in Pt/YIG [94] and Pt/NFO [97] films.

Last but not least, Lin *et al*. [219] recently reported a large enhancement of the LSSE signal on NM/AFM/YIG structures, where the thin AFM layer can enhance the spin current from YIG to NM by a factor of ten. They at-

tributed this observation to the enhancement of the spin mixing conductance in NM/AFM/YIG due to the magnons and the spin fluctuation in the AFM layer. However, this behaviour could be an effect of the normalization of the S_{SSE} to the temperature gradient instead of the heat flux since the interfacial thermal resistances in the systems could affect the measured signal, as thoroughly discussed in this thesis. Consequently, LSSE experiments with material combinations that show the enhancement of the signal regarding the temperature difference normalization and a subsequent comparison of the results when considering the heat flux normalization, would be a promissing idea to elucidate this issue.

Bibliography

[1] S. Mueller, *Upgrading and Repairing PCs* (Que Publishing, 800 East 96th Street, Indianapolis, Indiana 46240 USA, 2010).

[2] S. Waner and S. R. Costenoble, *Finite Mathematics* (Cengage Learning, Boston, USA, 2017).

[3] E. Pop, S. Sinha, and K. E. Goodson, "Heat Generation and Transport in Nanometer-Scale Transistors", Proc. IEEE **94**, 1587 (2006).

[4] A. Hoffmann and S. D. Bader, "Opportunities at the Frontiers of Spintronics", Phys. Rev. Applied **4**, 047001 (2015).

[5] M. N. Baibich, J. M. Broto, A. Fert, F. N. Van Dau, F. Petroff, P. Etienne, G. Creuzet, A. Friederich, and J. Chazelas, "Giant Magnetoresistance of (001)Fe/(001)Cr Magnetic Superlattices", Phys. Rev. Lett. **61**, 2472 (1988).

[6] G. Binasch, P. Grünberg, F. Saurenbach, and W. Zinn, "Enhanced magnetoresistance in layered magnetic structures with antiferromagnetic interlayer exchange", Phys. Rev. B **39**, 4828 (1989).

[7] M. Julliere, "Tunneling between ferromagnetic films", Phys. Lett. A **54**, 225 (1975).

[8] T. Miyazaki and N. Tezuka, "Giant magnetic tunneling effect in Fe/Al_2O_3 /Fe junction", J. Magn. Magn. Mater. **139**, L231 (1995).

[9] J. S. Moodera, L. R. Kinder, T. M. Wong, and R. Meservey, "Large Magnetoresistance at Room Temperature in Ferromagnetic Thin Film Tunnel Junctions", Phys. Rev. Lett. **74**, 3273 (1995).

[10] G. E. W. Bauer, E. Saitoh, and B. J. van Wees, “Spin caloritronics”, Nat. Mater. **11**, 391 (2012).

[11] S. T. B. Goennenwein and G. E. W. Bauer, “Spin caloritronics: Electron spins blow hot and cold”, Nat. Nanotechn. **7**, 145 (2012).

[12] S. R. Boona, R. C. Myers, and J. P. Heremans, “Spin caloritronics”, Energy Environ. Sci. **7**, 885 (2014).

[13] H. Yu, S. D. Brechet, and J.-P. Ansermet, “Spin caloritronics, origin and outlook”, Phys. Lett. A **381**, 825 (2017).

[14] J. Holanda, D. S. Maior, A. Azevedo, and S. M. Rezende, “Detecting the phonon spin in magnon-phonon conversion experiments”, Nat. Phys. **14**, 500 (2018).

[15] E. C. Stoner, “Collective Electron Ferromagnetism”, Proc. R. Soc. **165**, 372 (1938).

[16] S. Y. Huang, X. Fan, D. Qu, Y. P. Chen, W. G. Wang, J. Wu, T. Y. Chen, J. Q. Xiao, and C. L. Chien, “Transport Magnetic Proximity Effects in Platinum”, Phys. Rev. Lett. **109**, 107204 (2012).

[17] T. Kikkawa, K. Uchida, Y. Shiomi, Z. Qiu, D. Hou, D. Tian, H. Nakayama, X.-F. Jin, and E. Saitoh, “Longitudinal Spin Seebeck Effect Free from the Proximity Nernst Effect”, Phys. Rev. Lett. **110**, 067207 (2013).

[18] T. Kikkawa, K. Uchida, S. Daimon, Y. Shiomi, H. Adachi, Z. Qiu, D. Hou, X.-F. Jin, S. Maekawa, and E. Saitoh, “Separation of longitudinal spin Seebeck effect from anomalous Nernst effect: Determination of origin of transverse thermoelectric voltage in metal/insulator junctions”, Phys. Rev. B **88**, 214403 (2013).

[19] J. X. Li, M. W. Jia, Z. Ding, J. H. Liang, Y. M. Luo, and Y. Z. Wu, “Pt-enhanced anisotropic magnetoresistance in Pt/Fe bilayers”, Phys. Rev. B **90**, 214415 (2014).

[20] Y. Xu, B. Yang, C. Tang, Z. Jiang, M. Schneider, R. Whig, and J. Shi, “Heat-driven spin transport in a ferromagnetic metal”, Appl. Phys. Lett. **105**, 242404 (2014).

[21] B. F. Miao, S. Y. Huang, D. Qu, and C. L. Chien, “Absence of anomalous Nernst effect in spin Seebeck effect of Pt/YIG”, AIP Adv. **6**, 015018 (2016).

[22] D. Qu, S. Y. Huang, J. Hu, R. Wu, and C. L. Chien, "Intrinsic Spin Seebeck Effect in Au/YIG", Phys. Rev. Lett. **110**, 067206 (2013).

[23] M. Agrawal, V. I. Vasyuchka, A. A. Serga, A. Kirihara, P. Pirro, T. Langner, M. B. Jungfleisch, A. V. Chumak, E. T. Papaioannou, and B. Hillebrands, "Role of bulk-magnon transport in the temporal evolution of the longitudinal spin-Seebeck effect", Phys. Rev. B **89**, 224414 (2014).

[24] A. Kehlberger, G. Jakob, M. C. Onbasli, D. H. Kim, C. A. Ross, and M. Kläui, "Investigation of the magnetic properties of insulating thin films using the longitudinal spin Seebeck effect", J. Appl. Phys. **115**, 17C731 (2014).

[25] M. Schreier, G. E. W. Bauer, V. I. Vasyuchka, J. Flipse, K.-i. Uchida, J. Lotze, V. Lauer, A. V. Chumak, A. A. Serga, S. Daimon, T. Kikkawa, E. Saitoh, B. J. van Wees, B. Hillebrands, R. Gross, and S. T. B. Goennenwein, "Sign of inverse spin Hall voltages generated by ferromagnetic resonance and temperature gradients in yttrium iron garnet platinum bilayers", J. Phys. D **48**, 025001 (2015).

[26] K. Uchida, M. Ishida, T. Kikkawa, A. Kirihara, T. Murakami, and E. Saitoh, "Longitudinal spin Seebeck effect: from fundamentals to applications", J. Phys. Condens. Matter **26**, 343202 (2014).

[27] D. Meier, D. Reinhardt, M. van Straaten, C. Klewe, M. Althammer, M. Schreier, S. T. B. Goennenwein, A. Gupta, M. Schmid, C. H. Back, J.-M. Schmalhorst, T. Kuschel, and G. Reiss, "Longitudinal spin Seebeck effect contribution in transverse spin Seebeck effect experiments in Pt/YIG and Pt/NFO", Nat. Commun. **6**, 8211 (2015).

[28] D. Meier, T. Kuschel, S. Meyer, S. T. B. Goennenwein, L. Shen, A. Gupta, J.-M. Schmalhorst, and G. Reiss, "Detection of DC currents and resistance measurements in longitudinal spin Seebeck effect experiments on Pt/YIG and Pt/NFO", AIP Adv. **6**, 056302 (2016).

[29] A. Sola, P. Bougiatioti, M. Kuepferling, D. Meier, G. Reiss, M. Pasquale, T. Kuschel, and V. Basso, "Longitudinal spin Seebeck coefficient: heat flux vs. temperature difference method", Sci. Rep. **7**, 46752 (2017).

[30] R. Ramos, T. Kikkawa, K. Uchida, H. Adachi, I. Lucas, M. H. Aguirre, P. Algarabel, L. Morellón, S. Maekawa, E. Saitoh, and M. R. Ibarra, "Observation of the spin Seebeck effect in epitaxial Fe_3O_4 thin films", Appl. Phys. Lett. **102**, 072413 (2013).

[31] D. Meier, D. Reinhardt, M. Schmid, C. H. Back, J.-M. Schmalhorst, T. Kuschel, and G. Reiss, "Influence of heat flow directions on Nernst effects in Py/Pt bilayers", Phys. Rev. B **88**, 184425 (2013).

[32] R. Ramos, M. H. Aguirre, A. Anadón, J. Blasco, I. Lucas, K. Uchida, P. A. Algarabel, L. Morellón, E. Saitoh, and M. R. Ibarra, "Anomalous Nernst effect of Fe_3O_4 single crystal", Phys. Rev. B **90**, 054422 (2014).

[33] S. M. Wu, J. Hoffman, J. E. Pearson, and A. Bhattacharya, "Unambiguous separation of the inverse spin Hall and anomalous Nernst Effects within a ferromagnetic metal using the spin Seebeck effect", Appl. Phys. Lett. **105**, 092409 (2014).

[34] R. Ramos, T. Kikkawa, M. H. Aguirre, I. Lucas, A. Anadón, T. Oyake, K. Uchida, H. Adachi, J. Shiomi, P. A. Algarabel, L. Morellón, S. Maekawa, E. Saitoh, and M. R. Ibarra, "Unconventional scaling and significant enhancement of the spin Seebeck effect in multilayers", Phys. Rev. B **92**, 220407 (2015).

[35] K. I. Uchida, T. Kikkawa, T. Seki, T. Oyake, J. Shiomi, Z. Qiu, K. Takanashi, and E. Saitoh, "Enhancement of anomalous Nernst effects in metallic multilayers free from proximity-induced magnetism", Phys. Rev. B **92**, 094414 (2015).

[36] K.-D. Lee, D.-J. Kim, H. Y. Lee, S.-H. Kim, J.-H. Lee, K.-M. Lee, J.-R. Jeong, K.-S. Lee, H.-S. Song, J.-W. Sohn, S.-C. Shin, and B.-G. Park, "Thermoelectric Signal Enhancement by Reconciling the Spin Seebeck and Anomalous Nernst Effects in Ferromagnet/Non-magnet Multilayers", Sci. Rep. **5**, 10249 (2015).

[37] T. Kuschel, C. Klewe, P. Bougiatioti, O. Kuschel, J. Wollschläger, L. Bouchenoire, S. D. Brown, J. M. Schmalhorst, D. Meier, and G. Reiss, "Static Magnetic Proximity Effect in Pt Layers on Sputter-Deposited $NiFe_2O_4$ and on Fe of Various Thicknesses Investigated by XRMR", IEEE Trans. Magn. **52**, 4500104 (2016).

[38] K. Uchida, H. Adachi, T. Kikkawa, A. Kirihara, M. Ishida, S. Yorozu, S. Maekawa, and E. Saitoh, "Thermoelectric generation based on spin Seebeck effects", Proc. IEEE **104**, 1946 (2016).

[39] R. Ramos, A. Anadón, I. Lucas, K. Uchida, P. A. Algarabel, L. Morellón, M. H. Aguirre, E. Saitoh, and M. R. Ibarra, "Thermoelectric performance of spin Seebeck effect in Fe_3O_4/Pt-based thin film heterostructures", APL Mater. **4**, 104802 (2016).

[40] J. Holanda, O. Alves Santos, R. O. Cunha, J. B. S. Mendes, R. L. Rodrıguez-Suárez, A. Azevedo, and S. M. Rezende, "Longitudinal spin Seebeck effect in permalloy separated from the anomalous Nernst effect: Theory and experiment", Phys. Rev. B **95**, 214421 (2017).

[41] L. Onsager, "Reciprocal Relations in Irreversible Processes. I.", Phys. Rev. **37**, 405 (1931).

[42] Y. Onose, T. Ideue, H. Katsura, Y. Shiomi, N. Nagaosa, and Y. Tokura, "Observation of the Magnon Hall Effect", Science **329**, 297 (2010).

[43] Y. Tserkovnyak, A. Brataas, and G. E. W. Bauer, "Enhanced Gilbert Damping in Thin Ferromagnetic Films", Phys. Rev. Lett. **88**, 117601 (2002).

[44] B. Heinrich, Y. Tserkovnyak, G. Woltersdorf, A. Brataas, R. Urban, and G. E. W. Bauer, "Dynamic Exchange Coupling in Magnetic Bilayers", Phys. Rev. Lett. **90**, 187601 (2003).

[45] M. I. Dyakonov and V. I. Perel, "Possibility of orienting electron spins with current.", JETP Lett. **13**, 467 (1971).

[46] M. I. Dyakonov and V. I. Perel, "Current-induced spin orientation of electrons in semiconductors.", Phys. Lett. A. **35**, 459 (1971).

[47] J. N. Chazalviel and I. Solomon, "Experimental Evidence of the Anomalous Hall Effect in a Nonmagnetic Semiconductor", Phys. Rev. Lett. **29**, 1676 (1972).

[48] J. N. Chazalviel, "Spin-dependent Hall effect in semiconductors", Phys. Rev. B **11**, 3918 (1975).

[49] J. E. Hirsch, "Spin Hall Effect", Phys. Rev. Lett. **83**, 1834 (1999).

[50] Y. K. Kato, R. C. Myers, A. C. Gossard, and D. D. Awschalom, "Observation of the Spin Hall Effect in Semiconductors", Science **306**, 1910 (2004).

[51] J. Wunderlich, B. Kaestner, J. Sinova, and T. Jungwirth, "Experimental Observation of the Spin-Hall Effect in a Two-Dimensional Spin-Orbit Coupled Semiconductor System", Phys. Rev. Lett. **94**, 047204 (2005).

[52] M. Gradhand, D. V. Fedorov, P. Zahn, and I. Mertig, "Extrinsic Spin Hall Effect from First Principles", Phys. Rev. Lett. **104**, 186403 (2010).

[53] G. Vignale, "Ten Years of Spin Hall Effect", J. Supercond. Nov. Magn. **23**, 3 (2009).

[54] J. Sinova, D. Culcer, Q. Niu, N. A. Sinitsyn, T. Jungwirth, and A. H. MacDonald, "Universal Intrinsic Spin Hall Effect", Phys. Rev. Lett. **92**, 126603 (2004).

[55] K. Sato and E. Saitoh, *Spintronics for Next Generation Innovative Devices* (John Wiley and Sons, Ltd, United Kingdom, 2015).

[56] L. Liu, T. Moriyama, D. C. Ralph, and R. A. Buhrman, "Spin-Torque Ferromagnetic Resonance Induced by the Spin Hall Effect", Phys. Rev. Lett. **106**, 036601 (2011).

[57] Z. Tang, Y. Kitamura, E. Shikoh, Y. Ando, T. Shinjo, and M. Shiraishi, "Temperature Dependence of Spin Hall Angle of Palladium", Appl. Phys. Express **6**, 083001 (2013).

[58] L. Liu, C.-F. Pai, Y. Li, H. Tseng, D. Ralph, and R. Buhrman, "Spin-torque switching with the giant spin hall effect of tantalum", Science **336**, 555 (2012).

[59] C.-F. Pai, L. Liu, Y. Li, H. W. Tseng, D. C. Ralph, and R. A. Buhrman, "Spin transfer torque devices utilizing the giant spin Hall effect of tungsten", Appl. Phys. Lett. **101**, 122404 (2012).

[60] M. Althammer, S. Meyer, H. Nakayama, M. Schreier, S. Altmannshofer, M. Weiler, H. Huebl, S. Geprägs, M. Opel, R. Gross, D. Meier, C. Klewe, T. Kuschel, J.-M. Schmalhorst, G. Reiss, L. Shen, A. Gupta, Y.-T. Chen, G. E. W. Bauer, E. Saitoh, and S. T. B. Goennenwein, "Quantitative study of the spin Hall magnetoresistance in ferromagnetic insulator/normal metal hybrids", Phys. Rev. B **87**, 224401 (2013).

[61] E. Saitoh, M. Ueda, H. Miyajima, and G. Tatara, "Conversion of spin current into charge current at room temperature: Inverse spin-Hall effect", Appl. Phys. Lett. **88**, 182509 (2006).

[62] K. Ando and E. Saitoh, "Observation of the inverse spin Hall effect in silicon", Nat. Commun. **3**, 629 (2012).

[63] J. Bass and W. P. P. Jr, "Spin-diffusion lengths in metals and alloys, and spin-flipping at metal/metal interfaces: an experimentalist's critical review", J. Phys. Condens. Matter. **19**, 183201 (2007).

[64] O. Mosendz, J. E. Pearson, F. Y. Fradin, G. E. W. Bauer, S. D. Bader, and A. Hoffmann, "Quantifying Spin Hall Angles from Spin Pumping: Experiments and Theory", Phys. Rev. Lett. **104**, 046601 (2010).

[65] E. H. Hall, "On a New Action of the Magnet on Electric Currents", Amer. J. Math. **2**, 287 (1879).

[66] E. H. Hall, "XXXVIII. On the new action of magnetism on a permanent electric current", Philos. Mag. **12**, 301 (1880).

[67] E. Hall, "XVIII. On the "Rotational Coefficient" in nickel and cobalt", Philos. Mag. **12**, 157 (1881).

[68] M. V. Berry, Proceedings of the Royal Society of London A: Mathematical, Physical and Engineering Sciences **392**, 45 (1984).

[69] S. Lowitzer, M. Gradhand, D. Ködderitzsch, D. V. Fedorov, I. Mertig, and H. Ebert, "Extrinsic and Intrinsic Contributions to the Spin Hall Effect of Alloys", Phys. Rev. Lett. **106**, 056601 (2011).

[70] N. Vlietstra, J. Shan, V. Castel, B. J. van Wees, and J. Ben Youssef, "Spin-Hall magnetoresistance in platinum on yttrium iron garnet: Dependence on platinum thickness and in-plane/out-of-plane magnetization", Phys. Rev. B **87**, 184421 (2013).

[71] Y.-T. Chen, S. Takahashi, H. Nakayama, M. Althammer, S. T. B. Goennenwein, E. Saitoh, and G. E. W. Bauer, "Theory of spin Hall magnetoresistance", Phys. Rev. B **87**, 144411 (2013).

[72] H. Nakayama, M. Althammer, Y.-T. Chen, K. Uchida, Y. Kajiwara, D. Kikuchi, T. Ohtani, S. Geprägs, M. Opel, S. Takahashi, R. Gross, G. E. W. Bauer, S. T. B. Goennenwein, and E. Saitoh, "Spin Hall Magnetoresistance Induced by a Nonequilibrium Proximity Effect", Phys. Rev. Lett. **110**, 206601 (2013).

[73] Y.-T. Chen, S. Takahashi, H. Nakayama, M. Althammer, S. T. B. Goennenwein, E. Saitoh, and G. E. W. Bauer, "Theory of spin Hall magnetoresistance (SMR) and related phenomena", J. Phys. Condens. Matter **28**, 103004 (2016).

[74] W. Thomson, "On the Electro-Dynamic Qualities of Metals:–Effects of Magnetization on the Electric Conductivity of Nickel and of Iron", Proc. R. Soc. Lond. **8**, 546 (1856).

[75] T. Tritt, *Recent Trends in Thermoelectric Materials Research II* (Academic Press, New York, 2000).

[76] G. Nolas, J. Sharp, and J. Goldsmid, *Thermoelectrics* (Springer-Verlag Berlin Heidelberg, 2001).

[77] T. Seebeck, "Magnetische polarisation der metalle und erze durch temperatur-differenz", Abh. Akad. Wiss. Berlin **1820–21**, 189 (1822).

[78] A. v. Ettingshausen and W. Nernst, "Ueber das Auftreten electromotorischer Kräfte in Metallplatten, welche von einem Wärmestrome durchflossen werden und sich im magnetischen Felde befinden.", Ann. Phys. Chem. **343–347**, 265 (1886).

[79] K. Seeger, *Semiconductor Physics: An Introduction* (9th ed. Springer-Verlag Berlin Heidelberg, 2004).

[80] M. Johnson and R. H. Silsbee, "Thermodynamic analysis of interfacial transport and of the thermomagnetoelectric system", Phys. Rev. B **35**, 4959 (1987).

[81] S. O. Valenzuela and M. Tinkham, "Direct electronic measurement of the spin Hall effect", Nature **442**, 176 (2006).

[82] T. Kimura, Y. Otani, T. Sato, S. Takahashi, and S. Maekawa, "Room-Temperature Reversible Spin Hall Effect", Phys. Rev. Lett. **98**, 156601 (2007).

[83] K. Ando, S. Takahashi, J. Ieda, Y. Kajiwara, H. Nakayama, T. Yoshino, K. Harii, Y. Fujikawa, M. Matsuo, S. Maekawa, and E. Saitoh, "Inverse spin-Hall effect induced by spin pumping in metallic system", J. Appl. Phys. **109**, 103913 (2011).

[84] J. Xiao, G. E. W. Bauer, K.-c. Uchida, E. Saitoh, and S. Maekawa, "Theory of magnon-driven spin Seebeck effect", Phys. Rev. B **81**, 214418 (2010).

[85] S. Hoffman, K. Sato, and Y. Tserkovnyak, "Landau-Lifshitz theory of the longitudinal spin Seebeck effect", Phys. Rev. B **88**, 064408 (2013).

[86] H. Adachi, K.-i. Uchida, E. Saitoh, and S. Maekawa, "Theory of the spin Seebeck effect", Rep. Prog. Phys. **76**, 036501 (2013).

[87] A. Kehlberger, U. Ritzmann, D. Hinzke, E.-J. Guo, J. Cramer, G. Jakob, M. C. Onbasli, D. H. Kim, C. A. Ross, M. B. Jungfleisch, B. Hillebrands, U. Nowak, and M. Kläui, "Length Scale of the Spin Seebeck Effect", Phys. Rev. Lett. **115**, 096602 (2015).

[88] S. M. Rezende, R. L. Rodrıguez-Suárez, R. O. Cunha, A. R. Rodrigues, F. L. A. Machado, G. A. Fonseca Guerra, J. C. Lopez Ortiz, and A. Azevedo, "Magnon spin-current theory for the longitudinal spin-Seebeck effect", Phys. Rev. B **89**, 014416 (2014).

[89] S. Rezende, R. Rodríguez-Suárez, R. Cunha, J. L. Ortiz, and A. Azevedo, "Bulk magnon spin current theory for the longitudinal spin Seebeck effect", J. Magn. Magn. Mater. **400**, 171 (2016).

[90] L. J. Cornelissen, K. J. H. Peters, G. E. W. Bauer, R. A. Duine, and B. J. van Wees, "Magnon spin transport driven by the magnon chemical potential in a magnetic insulator", Phys. Rev. B **94**, 014412 (2016).

[91] J. Shan, L. J. Cornelissen, J. Liu, J. B. Youssef, L. Liang, and B. J. van Wees, "Criteria for accurate determination of the magnon relaxation length from the nonlocal spin Seebeck effect", Phys. Rev. B **96**, 184427 (2017).

[92] L. J. Cornelissen, J. Liu, R. A. Duine, J. B. Youssef, and B. J. van Wees, "Long-distance transport of magnon spin information in a magnetic insulator at room temperature", Nat. Phys. **11**, 1022 (2015).

[93] L. J. Cornelissen, J. Shan, and B. J. van Wees, "Temperature dependence of the magnon spin diffusion length and magnon spin conductivity in the magnetic insulator yttrium iron garnet", Phys. Rev. B **94**, 180402 (2016).

[94] L. J. Cornelissen, K. Oyanagi, T. Kikkawa, Z. Qiu, T. Kuschel, G. E. W. Bauer, B. J. van Wees, and E. Saitoh, "Nonlocal magnon-polaron transport in yttrium iron garnet", Phys. Rev. B **96**, 104441 (2017).

[95] J. Liu, L. J. Cornelissen, J. Shan, B. J. van Wees, and T. Kuschel, "Nonlocal magnon spin transport in yttrium iron garnet with tantalum and platinum spin injection/detection electrodes", J. Phys. D: Appl. Phys. **51**, 224005 (2018).

[96] J. Shan, P. Bougiatioti, L. Liang, G. Reiss, T. Kuschel, and B. J. van Wees, "Magnon spin transport in $NiFe_2O_4$ thin films", Appl. Phys. Lett. **110**, 132406 (2017).

[97] J. Shan, A. V. Singh, L. Liang, L. J. Cornelissen, Z. Galazka, A. Gupta, B. J. van Wees, and T. Kuschel, "Enhanced magnon spin transport in $NiFe_2O_4$ thin films on a lattice-matched substrate", Appl. Phys. Lett. **113**, 162403 (2018).

[98] K. Uchida, S. Takahashi, K. Harii, J. Ieda, W. Koshibae, K. Ando, S. Maekawa, and E. Saitoh, "Observation of the spin Seebeck effect", Nature **455**, 778 (2008).

[99] K. Uchida, J. Xiao, H. Adachi, J. Ohe, S. Takahashi, J. Ieda, T. Ota, Y. Kajiwara, H. Umezawa, H. Kawai, G. E. W. Bauer, S. Maekawa, and E. Saitoh, "Spin Seebeck insulator", Nat. Mater. **9**, 894 (2010).

[100] C. M. Jaworski, J. Yang, S. Mack, D. D. Awschalom, J. P. Heremans, and R. C. Myers, "Observation of the spin-Seebeck effect in a ferromagnetic semiconductor", Nat. Mater. **9**, 898 (2010).

[101] H. B. Callen and T. A. Welton, "Irreversibility and Generalized Noise", Phys. Rev. **83**, 34 (1951).

[102] J. Slonczewski, "Current-driven excitation of magnetic multilayers", J. Magn. Magn. Mater. **159**, L1 (1996).

[103] T. Gerrits, M. L. Schneider, and T. J. Silva, "Enhanced ferromagnetic damping in Permalloy/Cu bilayers", J. Appl. Phys. **99**, 023901 (2006).

[104] M. Schreier, A. Kamra, M. Weiler, J. Xiao, G. E. W. Bauer, R. Gross, and S. T. B. Goennenwein, "Magnon, phonon, and electron temperature profiles and the spin Seebeck effect in magnetic insulator/normal metal hybrid structures", Phys. Rev. B **88**, 094410 (2013).

[105] S. S.-L. Zhang and S. Zhang, "Magnon Mediated Electric Current Drag Across a Ferromagnetic Insulator Layer", Phys. Rev. Lett. **109**, 096603 (2012).

[106] F. Reif, *Fundamentals of Statistical and Thermal Physics* (Waveland Press, Inc., USA, 2009).

[107] S. Y. Huang, W. G. Wang, S. F. Lee, J. Kwo, and C. L. Chien, "Intrinsic Spin-Dependent Thermal Transport", Phys. Rev. Lett. **107**, 216604 (2011).

[108] A. D. Avery, M. R. Pufall, and B. L. Zink, "Observation of the Planar Nernst Effect in Permalloy and Nickel Thin Films with In-Plane Thermal Gradients", Phys. Rev. Lett. **109**, 196602 (2012).

[109] M. Schmid, S. Srichandan, D. Meier, T. Kuschel, J.-M. Schmalhorst, M. Vogel, G. Reiss, C. Strunk, and C. H. Back, "Transverse Spin Seebeck Effect versus Anomalous and Planar Nernst Effects in Permalloy Thin Films", Phys. Rev. Lett. **111**, 187201 (2013).

[110] C. T. Bui and F. Rivadulla, "Anomalous and planar Nernst effects in thin films of the half-metallic ferromagnet $La_{2/3}Sr_{1/3}MnO_3$", Phys. Rev. B **90**, 100403 (2014).

[111] I. V. Soldatov, N. Panarina, C. Hess, L. Schultz, and R. Schäfer, "Thermoelectric effects and magnetic anisotropy of $Ga_{1-x}Mn_xAs$ thin films", Phys. Rev. B **90**, 104423 (2014).

[112] D. Meier, "PhD thesis", Bielefeld University (2015).

[113] A. S. Shestakov, M. Schmid, D. Meier, T. Kuschel, and C. H. Back, "Dependence of transverse magnetothermoelectric effects on inhomogeneous magnetic fields", Phys. Rev. B **92**, 224425 (2015).

[114] K. Uchida, H. Adachi, T. Ota, H. Nakayama, S. Maekawa, and E. Saitoh, "Observation of longitudinal spin-Seebeck effect in magnetic insulators", Appl. Phys. Lett. **97**, 172505 (2010).

[115] A. Slachter, F. L. Bakker, J.-P. Adam, and B. J. van Wees, “Thermally driven spin injection from a ferromagnet into a non-magnetic metal”, Nat. Phys. **6**, 879 (2010).

[116] S.-g. Cheng, Y. Xing, Q.-f. Sun, and X. C. Xie, “Spin Nernst effect and Nernst effect in two-dimensional electron systems”, Phys. Rev. B **78**, 045302 (2008).

[117] X. Liu and X. Xie, “Spin Nernst effect in the absence of a magnetic field”, Solid State Commun. **150**, Spin Caloritronics, 471 (2010).

[118] P. Sheng, Y. Sakuraba, Y.-C. Lau, S. Takahashi, S. Mitani, and M. Hayashi, “The spin Nernst effect in tungsten”, Sci. Adv. **3** (2017).

[119] S. Meyer, Y.-T. Chen, S. Wimmer, M. Althammer, T. Wimmer, R. Schlitz, S. Geprägs, H. Huebl, D. Ködderitzsch, H. Ebert, G. E. W. Bauer, R. Gross, and S. T. B. Goennenwein, “Observation of the spin Nernst effect”, Nat. Mater. **16**, 977 (2017).

[120] M. Zuckermann, “The proximity effect for weak itinerant ferromagnets”, Solid State Commun. **12**, 745 (1973).

[121] T. Lin, M. A. Tomaz, M. M. Schwickert, and G. R. Harp, “Structure and magnetic properties of Ru/Fe(001) multilayers”, Phys. Rev. B **58**, 862 (1998).

[122] E. Wohlfarth, “The electronic properties of nickel-palladium alloys”, J. Phys. Chem. Solids **1**, 35 (1956).

[123] S. Rüegg and G. Schütz and P. Fischer and R. Wienke and W. B. Zeper and H. Ebert, “Spin-dependent x-ray absorption in Co/Pt multilayers”, J. Appl. Phys. **69**, 5655 (1991).

[124] H. Wende, A. Scherz, F. Wilhelm, and K. Baberschke, “Induced magnetism at thin-film interfaces probed by means of x-ray magnetic circular dichroism”, J. Phys. Condens. Matter **15**, S547 (2003).

[125] F. Wilhelm, M. Angelakeris, N. Jaouen, P. Poulopoulos, E. T. Papaioannou, C. Mueller, P. Fumagalli, A. Rogalev, and N. K. Flevaris, “Magnetic moment of Au at Au/Co interfaces: A direct experimental determination”, Phys. Rev. B **69**, 220404 (2004).

[126] P. Poulopoulos, A. Scherz, F. Wilhelm, H. Wende, and K. Baberschke, "Direct Probe of Induced Magnetic Moments at Interfaces via X-Ray Magnetic Circular Dichroism", Phys. stat. sol. (a) **189**, 293 (2002).

[127] M. A. Tomaz, W. J. A. Jr, W. L. O'Brien, and G. R. Harp, "Induced V moments in Fe/V(100), (211), and (110) superlattices studied using x-ray magnetic circular dichroism", J. Phys. Condens. Matter **9**, L179 (1997).

[128] M. M. Schwickert, G. Y. Guo, M. A. Tomaz, W. L. O'Brien, and G. R. Harp, "X-ray magnetic linear dichroism in absorption at the *L* edge of metallic Co, Fe, Cr, and V", Phys. Rev. B **58**, R4289 (1998).

[129] M. M. Sigalas and D. A. Papaconstantopoulos, "Calculations of the total energy, electron-phonon interaction, and Stoner parameter for metals", Phys. Rev. B **50**, 7255 (1994).

[130] Y. M. Lu, Y. Choi, C. M. Ortega, X. M. Cheng, J. W. Cai, S. Y. Huang, L. Sun, and C. L. Chien, "Pt Magnetic Polarization on $Y_3O_5Fe_{12}$ and Magnetotransport Characteristics", Phys. Rev. Lett. **110**, 147207 (2013).

[131] S. Geprägs, S. Meyer, S. Altmannshofer, M. Opel, F. Wilhelm, A. Rogalev, R. Gross, and S. T. B. Goennenwein, "Investigation of induced Pt magnetic polarization in $Pt/Y_3Fe_5O_{12}$ bilayers", Appl. Phys. Lett. **101**, 262407 (2012).

[132] T. Kuschel, C. Klewe, J.-M. Schmalhorst, F. Bertram, O. Kuschel, T. Schemme, J. Wollschläger, S. Francoual, J. Strempfer, A. Gupta, M. Meinert, G. Götz, D. Meier, and G. Reiss, "Static Magnetic Proximity Effect in $Pt/NiFe_2O_4$ and Pt/Fe Bilayers Investigated by X-Ray Resonant Magnetic Reflectivity", Phys. Rev. Lett. **115**, 097401 (2015).

[133] M. Valvidares, N. Dix, M. Isasa, K. Ollefs, F. Wilhelm, A. Rogalev, F. Sánchez, E. Pellegrin, A. Bedoya-Pinto, P. Gargiani, L. E. Hueso, F. Casanova, and J. Fontcuberta, "Absence of magnetic proximity effects in magnetoresistive $Pt/CoFe_2O_4$ hybrid interfaces", Phys. Rev. B **93**, 214415 (2016).

[134] M. Collet, R. Mattana, J.-B. Moussy, K. Ollefs, S. Collin, C. Deranlot, A. Anane, V. Cros, F. Petroff, F. Wilhelm and A. Rogalev, "Investigating magnetic proximity effects at ferrite/Pt interfaces", Appl. Phys. Lett. **111**, 202401 (2017).

[135] T. Kikkawa, M. Suzuki, J. Okabayashi, K.-i. Uchida, D. Kikuchi, Z. Qiu, and E. Saitoh, "Detection of induced paramagnetic moments in Pt on $Y_3Fe_5O_{12}$ via x-ray magnetic circular dichroism", Phys. Rev. B **95**, 214416 (2017).

[136] P. Manna and S. Yusuf, "Two interface effects: Exchange bias and magnetic proximity", Phys. Rep. **535**, 61 (2014).

[137] T. Manago, T. Ono, H. Miyajima, K. Kawaguchi, and M. Sohma, "Appearance of Ferromagnetism Induced by Proximity Effect and Exchange Enhancement in Multilayer Consisting of Antiferromagnetic NiO and Paramagnetic Pd", J. Phys. Soc. Japan **68**, 334 (1999).

[138] A. Hoffmann, M. R. Fitzsimmons, J. A. Dura, and C. F. Majkrzak, "Investigating magnetic proximity effects in NiO/Pd with polarized neutron reflectometry", Phys. Rev. B **65**, 024428 (2001).

[139] P. J. van der Zaag, Y. Ijiri, J. A. Borchers, L. F. Feiner, R. M. Wolf, J. M. Gaines, R. W. Erwin, and M. A. Verheijen, "Difference between Blocking and Néel Temperatures in the Exchange Biased Fe_3O_4/CoO System", Phys. Rev. Lett. **84**, 6102 (2000).

[140] J. A. Borchers, M. J. Carey, R. W. Erwin, C. F. Majkrzak, and A. E. Berkowitz, "Spatially modulated antiferromagnetic order in CoO/NiO superlattices", Phys. Rev. Lett. **70**, 1878 (1993).

[141] R. Pauthenet, "Aimantation spontanée des ferrites", Ann. Phys. **7**, 710 (1952).

[142] G. F. Dionne, "Molecular-field coefficients of $MnFe_2O_4$ and $NiFe_2O_4$ spinel ferrite systems", J. Appl. Phys. **63**, 3777 (1988).

[143] D. Meier, T. Kuschel, L. Shen, A. Gupta, T. Kikkawa, K. Uchida, E. Saitoh, J.-M. Schmalhorst, and G. Reiss, "Thermally driven spin and charge currents in thin $NiFe_2O_4$/Pt films", Phys. Rev. B **87**, 054421 (2013).

[144] C. Klewe, "PhD thesis", Bielefeld University (2016).

[145] W. C. Röntgen, *Ueber eine neue Art von Strahlen*, Sonderabbdruck aus den Sitzungsberichten der Würzburger Physik.-medic. Gesellschaft 1895, Vorläufige Mittheilung (1896).

[146] P. A. Varotsos and K. D. Alexopoulos, *Solid State Physics* (Savvala, Athens, Greece, 1995).

[147] T. N. Blanton and C. R. Hoople, "X-ray diffraction analysis of ultrathin platinum silicide films deposited on (100) silicon", Powder Diffr. **17**, 7 (2002).

[148] S. Macke and E. Goering, "Magnetic reflectometry of heterostructures", J. Phys. Condens. Matter **26**, 363201 (2014).

[149] M. Tolan, *X-Ray Scattering from Soft-Matter Thin Films* (Springer-Verlag Berlin Heidelberg, 1999).

[150] L. G. Parratt, "Surface Studies of Solids by Total Reflection of X-Rays", Phys. Rev. **95**, 359 (1954).

[151] L. Mino, G. Agostini, E. Borfecchia, D. Gianolio, A. Piovano, E. Gallo, and C. Lamberti, "Low-dimensional systems investigated by x-ray absorption spectroscopy: a selection of 2D, 1D and 0D cases", J. Phys. D **46**, 423001 (2013).

[152] M. Meinert and G. Reiss, "Electronic structure and optical band gap determination of $NiFe_2O_4$", J. Phys. Condens. Matter **26**, 115503 (2014).

[153] G. Schütz, R. Wienke, W. Wilhelm, W. Wagner, R. Frahm, and P. Kienle, "Spin-dependent absorption at the K- and $L_{2,3}$-edges in ferromagnetic $Fe_{80}Pt_{20}$ alloy", Physica B **158**, 284 (1989).

[154] G. Schütz, R. Wienke, W. Wilhelm, W. B. Zeper, H. Ebert, and K. Spörl, "Spin-dependent x-ray absorption in Co/Pt multilayers and $Co_{50}Pt_{50}$ alloy", J. Appl. Phys. **67**, 4456 (1990).

[155] H. Maruyama, A. Koizumi, K. Kobayashi, and H. Yamazaki, "X-Ray Magnetic Circular Dichroism and XANES Spectra at Pt $L_{2,3}$-edges in Fe–Pt Alloys", Jpn. J. Appl. Phys. **32**, 290 (1993).

[156] W. J. Antel, M. M. Schwickert, T. Lin, W. L. O'Brien, and G. R. Harp, "Induced ferromagnetism and anisotropy of Pt layers in Fe/Pt(001) multilayers", Phys. Rev. B **60**, 12933 (1999).

[157] F. Wilhelm, P. Poulopoulos, G. Ceballos, H. Wende, K. Baberschke, P. Srivastava, D. Benea, H. Ebert, M. Angelakeris, N. K. Flevaris, D. Niarchos, A. Rogalev, and N. B. Brookes, "Layer-Resolved Magnetic Moments in Ni/Pt Multilayers", Phys. Rev. Lett. **85**, 413 (2000).

[158] P. Poulopoulos, F. Wilhelm, H. Wende, G. Ceballos, K. Baberschke, D. Benea, H. Ebert, M. Angelakeris, N. K. Flevaris, A. Rogalev, and N. B. Brookes, "X-ray magnetic circular dichroic magnetometry on Ni/Pt multilayers", J. Appl. Phys. **89**, 3874 (2001).

[159] F. Wilhelm, P. Poulopoulos, A. Scherz, H. Wende, K. Baberschke, M. Angelakeris, N. K. Flevaris, J. Goulon, and A. Rogalev, "Interface magnetism in 3d/5d multilayers probed by X-ray magnetic circular dichroism", Phys. Status Solidi A **196**, 33 (2003).

[160] M. Suzuki, H. Muraoka, Y. Inaba, H. Miyagawa, N. Kawamura, T. Shimatsu, H. Maruyama, N. Ishimatsu, Y. Isohama, and Y. Sonobe, "Depth profile of spin and orbital magnetic moments in a subnanometer Pt film on Co", Phys. Rev. B **72**, 054430 (2005).

[161] C. Klewe, T. Kuschel, J.-M. Schmalhorst, F. Bertram, O. Kuschel, J. Wollschläger, J. Strempfer, M. Meinert, and G. Reiss, "Static magnetic proximity effect in $Pt/Ni_{1-x}Fe_x$ bilayers investigated by x-ray resonant magnetic reflectivity", Phys. Rev. B **93**, 214440 (2016).

[162] B. Henke, E. Gullikson, and J. Davis, "X-Ray Interactions: Photoabsorption, Scattering, Transmission, and Reflection at E = 50-30,000 eV, Z = 1-92", Atomic Data and Nuclear Data Tables **54**, 181 (1993).

[163] P. J. Flanders, "An alternating-gradient magnetometer (invited)", J. Appl. Phys. **63**, 3940 (1988).

[164] K. J. LL.D., "XLIII. On rotation of the plane of polarization by reflection from the pole of a magnet", Philos. Mag. **3**, 321 (1877).

[165] C. Klewe, M. Meinert, A. Boehnke, K. Kuepper, E. Arenholz, A. Gupta, J.-M. Schmalhorst, T. Kuschel, and G. Reiss, "Physical characteristics and cation distribution of $NiFe_2O_4$ thin films with high resistivity prepared by reactive co-sputtering", J. Appl. Phys. **115**, 123903 (2014).

[166] A. Sola, M. Kuepferling, V. Basso, M. Pasquale, T. Kikkawa, K. Uchida, and E. Saitoh, "Evaluation of thermal gradients in longitudinal spin Seebeck effect measurements", J. Appl. Phys. **117**, 17C510 (2015).

[167] B. Schulz and M. Hoffmann, "Thermophysical properties of the system Al_2O_3-MgO", High Temp. - High Pressures **34**, 203 (2002).

[168] *CrysTec GmbH, MgO for Research and Development*, `https://www.msesupplies.com/products/mgo-magnesium-oxide-crystal`, Accessed: 2018-02-02.

[169] A. T. Nelson, J. T. White, D. A. Andersson, J. A. Aguiar, K. J. McClellan, D. D. Byler, M. P. Short, and C. R. Stanek, "Thermal Expansion, Heat Capacity, and Thermal Conductivity of Nickel Ferrite ($NiFe_2O_4$)", J. Am. Ceram. Soc. **97**, 1559 (2014).

[170] W. Fulkerson, J. P. Moore, and D. L. McElroy, "Comparison of the Thermal Conductivity, Electrical Resistivity, and Seebeck Coefficient of a High-Purity Iron and an Armco Iron to 1000 °C", J. Appl. Phys. **37**, 2639 (1966).

[171] X. Zheng, D. Cahill, P. Krasnochtchekov, R. Averback, and J.-C. Zhao, "High-throughput thermal conductivity measurements of nickel solid solutions and the applicability of the Wiedemann–Franz law", Acta Mater. **55**, 5177 (2007).

[172] D. M. Rowe, *Modules, Systems, and Applications in Thermoelectrics* (Boca Raton: CRC Press., 2012).

[173] X. Wu, Z. Liu, and T. Luo, "Magnon and phonon dispersion, lifetime, and thermal conductivity of iron from spin-lattice dynamics simulations", J. Appl. Phys. **123**, 085109 (2018).

[174] P. Bougiatioti, O. Manos, C. Klewe, D. Meier, N. Teichert, J.-M. Schmalhorst, T. Kuschel, and G. Reiss, "Electrical transport and optical band gap of $NiFe_2O_x$ thin films", J. Appl. Phys. **122**, 225101 (2017).

[175] Z. Li, E. S. Fisher, J. Z. Liu, and M. V. Nevitt, "Single-crystal elastic constants of Co-Al and Co-Fe spinels", J. Mater. Sci. **26**, 2621 (1991).

[176] G. Nolas, J. Sharp, and J. Goldsmid, *Quantum Wells, Wires and Dots: Theoretical and Computational Physics of Semiconductor Nanostructures* (2nd ed. Wiley-Interscience, Chichester, 2005).

[177] D. Fritsch and C. Ederer, “Epitaxial strain effects in the spinel ferrites $CoFe_2O_4$ and $NiFe_2O_4$ from first principles”, Phys. Rev. B **82**, 104117 (2010).

[178] J. X. Ma, D. Mazumdar, G. Kim, H. Sato, N. Z. Bao, and A. Gupta, “A robust approach for the growth of epitaxial spinel ferrite films”, J. Appl. Phys. **108**, 063917 (2010).

[179] V. F. Gantmakher and I. M. Lucia, *Electrons and disorder in solids* (Oxford University Press, Oxford, 2005).

[180] B. I. Shklovskii and A. L. Efros, *Electronic Properties of Doped Semiconductors* (Springer, Berlin, 1984).

[181] N. F. Mott, “Conduction and switching in non-crystalline materials”, Contemp. Phys. **10**, 125 (1969).

[182] H. Lord and R. Parker, “Electrical Resistivity of Nickel Ferrite”, Nature (London) **188**, 929 (1960).

[183] I. G. Austin and D. Elwell, “Magnetic semiconductors”, Contemp. Phys. **11**, 455 (1970).

[184] N. Ponpandian, P. Balaya, and A. Narayanasamy, “Electrical conductivity and dielectric behaviour of nanocrystalline $NiFe_2O_4$ spinel”, J. Phys. Condens. Matter **14**, 3221 (2002).

[185] B. Baruwati, K. M. Reddy, S. V. Manorama, R. K. Singh, and O. Parkash, “Tailored conductivity behavior in nanocrystalline nickel ferrite”, Appl. Phys. Lett. **85**, 2833 (2004).

[186] D. Mergel and Z. Qiao, “Dielectric modelling of optical spectra of thin In_2O_3: Sn films”, J. Phys. D: Appl. Phys. **35**, 794 (2002).

[187] C. E. Turner, “Hall mobility measurements on iron rich nickel ferrites from room temperature to 600 degrees C”, J. Phys. C: Solid State Phys. **5**, 2859 (1972).

[188] B. S. Holinsworth, D. Mazumdar, H. Sims, Q.-C. Sun, M. K. Yurtisigi, S. K. Sarker, A. Gupta, W. H. Butler, and J. L. Musfeldt, “Chemical tuning of the optical band gap in spinel ferrites: $CoFe_2O_4$ vs $NiFe_2O_4$”, Appl. Phys. Lett. **103**, 082406 (2013).

[189] Q.-C. Sun, H. Sims, D. Mazumdar, J. X. Ma, B. S. Holinsworth, K. R. O'Neal, G. Kim, W. H. Butler, A. Gupta, and J. L. Musfeldt, "Optical band gap hierarchy in a magnetic oxide: Electronic structure of $NiFe_2O_4$", Phys. Rev. B **86**, 205106 (2012).

[190] P. Bougiatioti, C. Klewe, D. Meier, O. Manos, O. Kuschel, J. Wollschläger, L. Bouchenoire, S. D. Brown, J.-M. Schmalhorst, G. Reiss, and T. Kuschel, "Quantitative Disentanglement of the Spin Seebeck, Proximity-Induced, and Ferromagnetic-Induced Anomalous Nernst Effect in Normal-Metal–Ferromagnet Bilayers", Phys. Rev. Lett. **119**, 227205 (2017).

[191] P. Bougiatioti, O. Manos, G. Reiss, and T. Kuschel, "Quantitative separation of thermal spin transport phenomena and their correlation to the magnetic properties in metallic normal metal/ferromagnet bilayer systems", under preparation (2018).

[192] M. Schreier, N. Roschewsky, E. Dobler, S. Meyer, H. Huebl, R. Gross, and S. T. B. Goennenwein, "Current heating induced spin Seebeck effect", Appl. Phys. Lett. **103**, 242404 (2013).

[193] O. Reimer, D. Meier, M. Bovender, L. Helmich, J.-O. Dreessen, J. Krieft, A. S. Shestakov, C. H. Back, J.-M. Schmalhorst, A. Hütten, G. Reiss, and T. Kuschel, "Quantitative separation of the anisotropic magnetothermopower and planar Nernst effect by the rotation of an in-plane thermal gradient", Sci. Rep. **7**, 40586 (2017).

[194] O. Reimer, "PhD thesis", Bielefeld University (2018).

[195] N. Vlietstra, J. Shan, B. J. van Wees, M. Isasa, F. Casanova, and J. Ben Youssef, "Simultaneous detection of the spin-Hall magnetoresistance and the spin-Seebeck effect in platinum and tantalum on yttrium iron garnet", Phys. Rev. B **90**, 174436 (2014).

[196] S. M. Wu, F. Y. Fradin, J. Hoffman, A. Hoffmann, and A. Bhattacharya, "Spin Seebeck devices using local on-chip heating", J. Appl. Phys. **117**, 17C509 (2015).

[197] M. Weiler, M. Althammer, F. D. Czeschka, H. Huebl, M. S. Wagner, M. Opel, I.-M. Imort, G. Reiss, A. Thomas, R. Gross, and S. T. B. Goennenwein, "Local Charge and Spin Currents in Magnetothermal Landscapes", Phys. Rev. Lett. **108**, 106602 (2012).

[198] A. M. Hofmeister, “Thermal diffusivity of garnets at high temperature”, Phys. Chem. Miner. **33**, 45 (2006).

[199] N. Nagaosa, J. Sinova, S. Onoda, A. H. MacDonald, and N. P. Ong, “Anomalous Hall effect”, Rev. Mod. Phys. **82**, 1539 (2010).

[200] Y.-q. Zhang, N.-y. Sun, W.-r. Che, R. Shan, and Z.-g. Zhu, “A novel method to evaluate spin diffusion length of Pt”, Physica B **488**, 67 (2016).

[201] T. C. Chuang, P. L. Su, P. H. Wu, and S. Y. Huang, “Enhancement of the anomalous Nernst effect in ferromagnetic thin films”, Phys. Rev. B **96**, 174406 (2017).

[202] S. Srichandan, S. Wimmer, S. Pöllath, M. Kronseder, H. Ebert, C. H. Back, and C. Strunk, “Magnon scattering in the transport coefficients of CoFe thin films”, Phys. Rev. B **98**, 020406 (2018).

[203] H. Yuasa, K. Tamae, and N. Onizuka, “Spin mixing conductance enhancement by increasing magnetic density”, AIP Adv. **7**, 055928 (2017).

[204] A. Rastogi, A. V. Singh, Z. Li, T. Peters, P. Bougiatioti, D. Meier, J. B. Mohammadi, B. Khodadadi, T. Mewes, R. Mishra, J. Gazquez, Borisevich, Z. Galazka, R. Uecker, G. Reiss, T. Kuschel, and A. Gupta, “Enhancement in Thermally Generated Spin Voltage at Nickel Ferrite/Pt Interface”, under review (2018).

[205] A. Prakash, B. Flebus, J. Brangham, F. Yang, Y. Tserkovnyak, and J. P. Heremans, “Evidence for the role of the magnon energy relaxation length in the spin Seebeck effect”, Phys. Rev. B **97**, 020408 (2018).

[206] P. Bougiatioti, O. Manos, O. Kuschel, J. Wollschläger, M. Tolkiehn, S. Francoual, and T. Kuschel, “Impact of magnetic moment and anisotropy of $Co_{1-x}Fe_x$ thin films on the magnetic proximity effect of Pt”, under review, 1807.09032 (2018).

[207] L. Bouchenoire, S. D. Brown, P. Thompson, J. A. Duffy, J. W. Taylor, and M. J. Cooper, “Performance of phase plates on the XMaS beamline at the ESRF”, J. Synchrotron Radiat. **10**, 172 (2003).

[208] S. D. Brown, L. Bouchenoire, D. Bowyer, J. Kervin, D. Laundy, M. J. Longfield, D. Mannix, D. F. Paul, A. Stunault, P. Thompson, M. J. Cooper, C. A. Lucas, and W. G. Stirling, "The XMaS beamline at ESRF: instrumental developments and high-resolution diffraction studies", J. Synchrotron Radiat. **8**, 1172 (2001).

[209] J. Strempfer, S. Francoual, D. Reuther, D. K. Shukla, A. Skaugen, H. Schulte-Schrepping, K. T., and H. Franz, "Resonant scattering and diffraction beamline P09 at PETRA III", J. Synchrotron Radiat. **20**, 541 (2013).

[210] J. Geissler, E. Goering, M. Justen, F. Weigand, G. Schütz, J. Langer, D. Schmitz, H. Maletta, and R. Mattheis, "Pt magnetization profile in a Pt/Co bilayer studied by resonant magnetic x-ray reflectometry", Phys. Rev. B **65**, 020405 (2001).

[211] D. Bonnenberg, K. A. Hempel, and H. Wijn, *Atomic magnetic moment, magnetic moment density, g and g' factor* (Springer-Verlag Berlin Heidelberg, 1986).

[212] D. M. Bozorth, *Ferromagnetism* (Van Nostrand, New York, 1951).

[213] S. Geprägs, S. T. B. Goennenwein, M. Schneider, F. Wilhelm, K. Ollefs, A. Rogalev, M. Opel, and R. Gross, "Comment on: Pt magnetic polarization on $Y_3Fe_5O_{12}$ and magnetotransport characteristics", arXiv:1307.4869 (2013).

[214] J.L Costa-Krämer, J.L Menéndez, A Cebollada, F Briones, D Garciá and A Hernando, "Magnetization reversal asymmetry in Fe/MgO(001) thin films", J. Magn. Magn. Mater. **210**, 341 (2000).

[215] T. Kuschel, H. Bardenhagen, H. Wilkens, R. Schubert, J. Hamrle, J. Pištora and J. Wollschläger, "Vectorial magnetometry using magnetooptic Kerr effect including first- and second-order contributions for thin ferromagnetic films", J. Phys. D: Appl. Phys. **44**, 265003 (2011).

[216] K. Shikada, M. Ohtake, F. Kirino, and M. Futamoto, "Microstructure and magnetic properties of FeCo epitaxial thin films grown on MgO single-crystal substrates", J. Appl. Phys. **105**, 07C303 (2009).

[217] T. Kuschel, J. Hamrle, J. Pištora, K. Saito, S. Bosu, Y. Sakuraba, K. Takanashi and J. Wollschläger, "Magnetic characterization of thin $Co_{50}Fe_{50}$ films by magnetooptic Kerr effect", J. Phys. D: Appl. Phys. **45**, 495002 (2012).

[218] T. Kikkawa, K. Shen, B. Flebus, R. A. Duine, K.-i. Uchida, Z. Qiu, G. E. W. Bauer, and E. Saitoh, "Magnon Polarons in the Spin Seebeck Effect", Phys. Rev. Lett. **117**, 207203 (2016).

[219] W. Lin, K. Chen, S. Zhang, and C. L. Chien, "Enhancement of Thermally Injected Spin Current through an Antiferromagnetic Insulator", Phys. Rev. Lett. **116**, 186601 (2016).

Chapter 8

Publications

1. Orestis Manos, **Panagiota Bougiatioti**, Denis Dyck, Torsten Hübner, Jan-Michael Schmalhorst and Günter Reiss, "Correlation of tunnel magnetoresistance with the magnetic properties in perpendicular CoFeB-based junctions with exchange bias", J. Appl. Phys., **125**, 023905 (2019)

2. **Panagiota Bougiatioti**, Orestis Manos, Olga Kuschel, Joachim Wollschläger, Martin Tolkiehn, Sonia Francoual and Timo Kuschel, "Impact of magnetic moment and anisotropy of $Co_{1-x}Fe_x$ thin films on the magnetic proximity effect of Pt", Phys. Rev. Lett., under review, arXiv:1807.09032, (2018)

3. A. Rastogi, A. V. Singh, Z. Li, T. Peters, **P. Bougiatioti**, D. Meier, J. B. Mohammadi, B. Khodadadi, T. Mewes, R. Mishra, J. Gazquez, A. Y. Borisevich, Z. Galazka, R. Uecker, G. Reiss, T. Kuschel and A. Gupta, "Enhancement in Thermally Generated Spin Voltage at Nickel Ferrite/Pt Interface", Phys. Rev. Lett., under review, (2018)

4. **Panagiota Bougiatioti**, Christoph Klewe, Daniel Meier, Orestis Manos, Olga Kuschel, Joachim Wollschläger, Laurence Bouchenoire, Simon D. Brown, Jan-Michael Schmalhorst, Günter Reiss and Timo Kuschel, "Quantitative Disentanglement of the Spin Seebeck, Proximity-Induced,

and Ferromagnetic-Induced Anomalous Nernst Effect in Normal-Metal–Ferromagnet Bilayers", Phys. Rev. Lett., **119**, 227205, (2017)

5. **Panagiota Bougiatioti**, Orestis Manos, Christoph Klewe, Daniel Meier, Niclas Teichert Jan-Michael Schmalhorst, Timo Kuschel and Günter Reiss, "Electrical transport and optical band gap of $NiFe_2O_x$ thin films", J. Appl. Phys., **122**, 225101, (2017)

6. Orestis Manos, Alexander Böhnke, **Panagiota Bougiatioti**, Robin Klett, Karsten Rott, Alessia Niesen, Jan-Michael Schmalhorst and Günter Reiss, "Tunneling magnetoresistance of perpendicular CoFeB-based junctions with exchange bias", J. Appl. Phys., **122**, 103904, (2017)

7. A. Sola, **P. Bougiatioti**, M. Kuepferling, D. Meier, G. Reiss, M. Pasquale, T. Kuschel and V. Basso, "Longitudinal spin Seebeck coefficient: heat flux vs. temperature difference method", Sci. Rep., **7**, 46752, (2017)

8. J. Shan, **P. Bougiatioti**, L. Liang, G. Reiss, T. Kuschel, and B. J. van Wees, "Nonlocal magnon spin transport in $NiFe_2O_4$ thin films", Appl. Phys. Lett., **110**, 132406, (2017)

9. Timo Kuschel, Christoph Klewe, **Panagiota Bougiatioti**, Olga Kuschel, Joachim Wollschläger, Laurence Bouchenoire, Simon D. Brown, Jan-Michael Schmalhorst, Daniel Meier, and Günter Reiss, "Static Magnetic Proximity Effect in Pt Layers on Sputter-Deposited $NiFe_2O_4$ and on Fe of Various Thicknesses Investigated by XRMR", IEEE Trans. Magn., **52**, 4500104, (2016)

Conferences

03/2017 Talk at the **81st Deutsche Physikalische Gesellschaft Frühjahrstagung**, Dresden, Germany

02/2017 Poster at the **Spinmechanics 4**, Lake Louise, Canada

07/2016 Poster at the **Spin Caloritronics 7**, Utrecht, The Netherlands

03/2016 Talk at the **80th Deutsche Physikalische Gesellschaft Frühjahrstagung**, Regensburg, Germany

06/2015 Poster at the **Spinmechanics 3**, Munich, Germany

06/2015 Poster at the **SpinCat PhD workshop**, Garching, Germany

03/2015 Poster at the **79th Deutsche Physikalische Gesellschaft Frühjahrstagung**, Berlin, Germany

02/2015 Poster at the **Colloquium of the SPP 1538 (SpinCat)**, Bad Honnef, Germany

Acknowledgements

Finally, I am taking this opportunity to express my gratitude to everyone who contributed to the successful completion of this work.

First and foremost I wish to thank my doctoral supervisor, Prof. Dr. Günter Reiss, for providing me with the opportunity to become a member of his working group, pursuing my Ph.D. in a high-tech environment and driving exploratory research under his constant support and advice, in all stages of my doctoral studies.

I would also like to extend my deepest gratitude to my direct supervisor, Dr. Timo Kuschel, who contributed significantly to the success of this work via his aspiring guidance, encouragement, invaluably constructive criticism, direct response to my questions and queries, and friendly advice during my studies.

For the scientific discussions and the excellent collaboration I would like to thank my former colleagues Dr. Christoph Klewe and Dr. Daniel Meier who also worked in the fields of spintronics and spin caloritronics and with their team spirit provided great help regarding my first steps as a PhD student.

I am also grateful to Dr. Karsten Rott for his invaluable assistance to any technical problem regarding the lab equipment and his great helpfulness for the execution of the experiments.

I would like to thank Aggi Windmann for her contribution to resolve administrative issues fast and effectively.

I am very much thankful to all the members of D2 for the very pleasant working atmosphere and especially I would like to name some of them for their direct or indirect involvement in the completion of this work. Thank you, Dr. Jan-Michael Schmalhorst, Prof. Dr. Andreas Hütten, Orestis Manos, Alessia Niesen, Dr. Niclas Teichert, Robin Silber, Dr. Alexander Böhnke, Anastasiia

Moskaltsova, Dr. Oliver Reimer, Jan Krieft, Niklas Dohmeier, Dr. Robin Klett, Dr. Torsten Hübner, and Dr. Manuel Glas.

I also had great pleasure of collaborating with Prof. Dr. habil. Joachim Wollschläger and Olga Kuschel from Osnabrück University as well as Dr. Alessandro Sola from Istituto Nazionale di Ricerca Metrologica in Turin. Thank you for the scientific discussions and contributions.

I gratefully acknowledge the Deutsche Forschungsgemeinschaft (DFG) for the financial support under the priority program Spin Caloric Transport (SPP 1538). In addition, many thanks go to the reviewers of my dissertation and the rest members of my dissertation committee for rating my work and attending my defence.

I would be remiss not to acknowledge Prof. Dr. George Triberis from National and Kapodistrian University of Athens who was my mentor during the first steps of my scientific career, encouraging me to pursue my Ph.D dream. It was a great honor for me to share of his exceptional scientific knowledge.

Special thanks go to my close circle of friends who provided me with support and friendship throughout this experience.

I would like to dedicate the last lines where the most basic source of my life energy resides: my parents and my brother. Thank you for encouraging me in all of my pursuits and inspiring me to follow my dreams, no matter how difficult and long the ride was. This journey would not have been possible without such a powerful team behind me.